3

The Sun as the prime source of space weather

Volker Bothmer and Andrei Zhukov

The Sun is the prime source of energy in our solar system and it is the prime source of space weather. This chapter provides an overview on the main forms of solar energy output – fast and slow solar wind streams, co-rotating interaction regions, flares, coronal mass ejections and their interplanetary counterparts, solar energetic particle events – that determine space weather conditions in the interplanetary medium and in geospace and their variation with the solar activity cycle. The chapter also addresses the processes through which the energy transfer is modulated by solar, interplanetary and terrestrial conditions. The outlook of the chapter aims at defining the required observations that are crucial to help establishing real-time space weather forecasts.

3.1 INTRODUCTION – THE SUN'S ENERGY OUTPUT AND VARIABILITY

The Sun is the most powerful source of energy in our solar system and sustains life on Earth. It primarily emits energy in the form of electromagnetic (EM) radiation. The solar irradiance spectrum is shown in Figure 3.1. Since the full spectrum is made up of several components, it varies from an idealized black-body spectrum. The Sun's atmospheric layers overlying the visible disk – the photosphere, the chromosphere and corona (see Figure 3.4 in color section and Figure 3.7) – contribute to the spectr5m at EUV and X-ray wavelengths. These layers consist of a tenuous fully ionized plasma and hence cannot be treated as a black-body. Since the magnetic structure of the Sun's photosphere varies continuously (see Section 3.3.1) transient processes – such as micro- and nano-flares, shock waves, erupting prominences, flares and coronal mass ejections (CMEs) – cause short-time increases of EUV-, X-ray, gamma-ray and radio-wave emissions superimposed on the Sun's continuous spectrum (Figure 3.2). For a more detailed introduction to the physics of the solar spectrum the reader is referred to the introductions in the books by Aschwanden (2004) and Stix (2004).

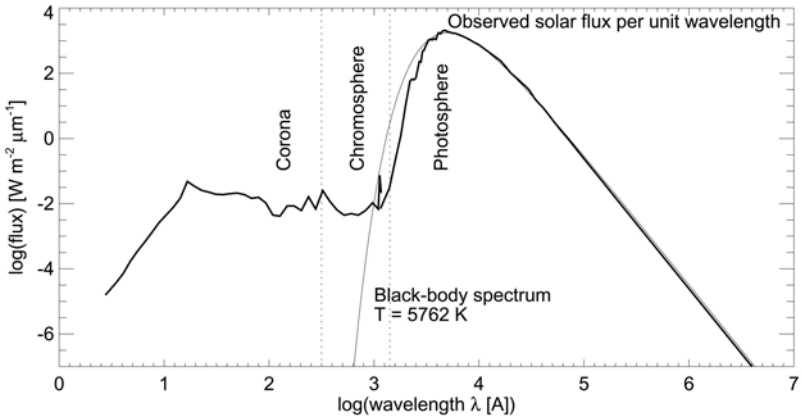

Figure 3.1. Measured spectrum of the solar flux and that of a black-body with $T = 5762\,\mathrm{K}$. From Aschwanden (2004).

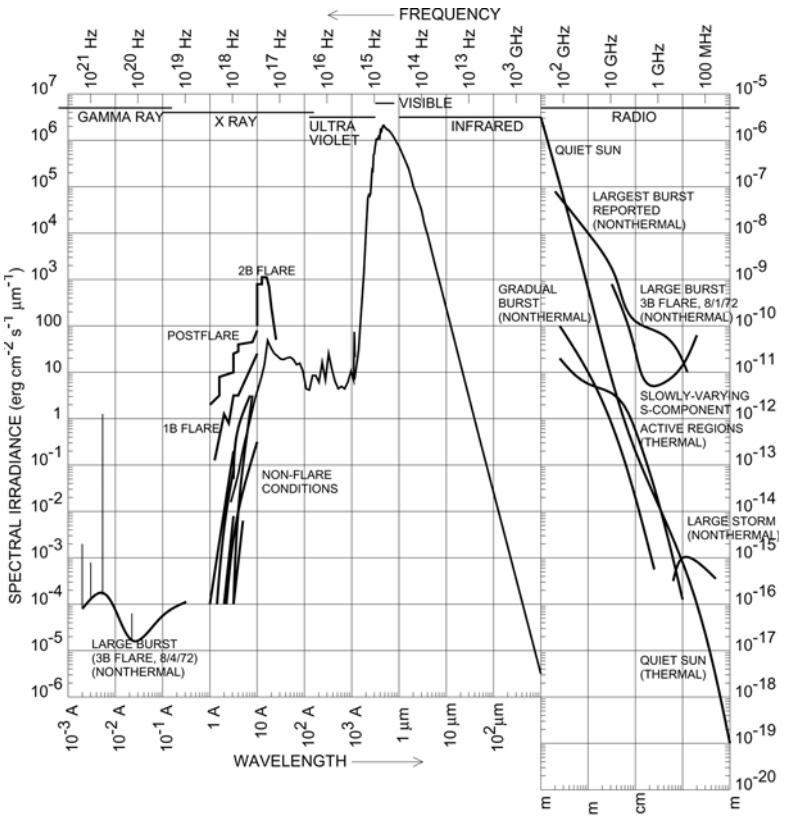

Figure 3.2. Full solar irradiance spectrum. Note the shift in the y-axis scaling by 12 orders of magnitude at a wavelength of 1 mm. From Aschwanden (2004).

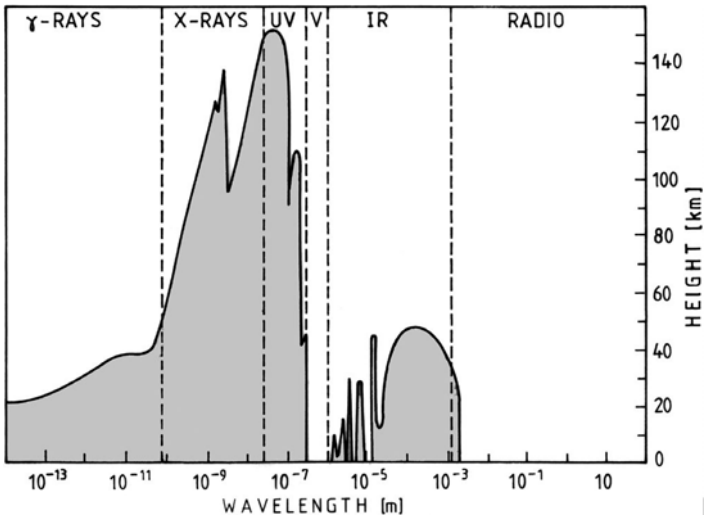

Figure 3.3. Absorption of solar radiation by the Earth's atmosphere. The shaded areas provide the height above ground where the incoming intensity is reduced to 50% of its original strength. After Nicolson (1982), adapted by Stix (2004).

On Earth – only at the visible wavelengths and part of the radio wavelength regime – the atmosphere is fully transparent to the Sun's radiation (see Figure 3.3) so that solar observations at X-ray and EUV wavelengths have to be achieved through space missions. The Yohkoh mission, launched on August 31, 1991 can be regarded as a milestone in terms of continuous high spatial resolution, full disk solar remote-sensing observations at X-ray wavelengths. Until the end of its mission life-time – on December 14, 2001 – it provided stunning new views of the Sun's X-ray corona (Figure 3.4, color section).

Although the Sun's total irradiance – the 'Solar Constant', being roughly $1367\,W/m^2$ as measured at the distance of the Earth – varies only at the order of 0.1% in the course of the solar cycle (e.g., Froehlich, 2003), the variation at specific wavelength intervals can be much larger (see Chapter 8). Since intensity variations at UV- and EUV-wavelengths may have important effects on the Earth's atmosphere, this subject is one of the hot current research topics. Figure 3.5 (color section) shows the variation of the longitudinal component of the photospheric magnetic field from solar activity maximum around 1992 until the next one around 2000, as measured by the US Kitt Peak National Solar Observatory (KPNSO), Tucson, Arizona, together with the measurements of the Sun's coronal soft X-ray emission, as measured by the Soft X-ray Telescope (SXT) onboard the Japanese/US Yohkoh satellite. The total variation of irradiance – in the range 2–30 Å – was roughly at the order of 10^2 between 1992 and 1996, but can in principle be much larger in case the solar photospheric magnetic fields are more frequent and intense, as can be expected, for example, from the highly varying number of sunspots in the different c. 11-yr long solar activity cycles (Figure 3.6). Benevolenskaya *et al.* (2002) found that the soft X-ray intensity shows

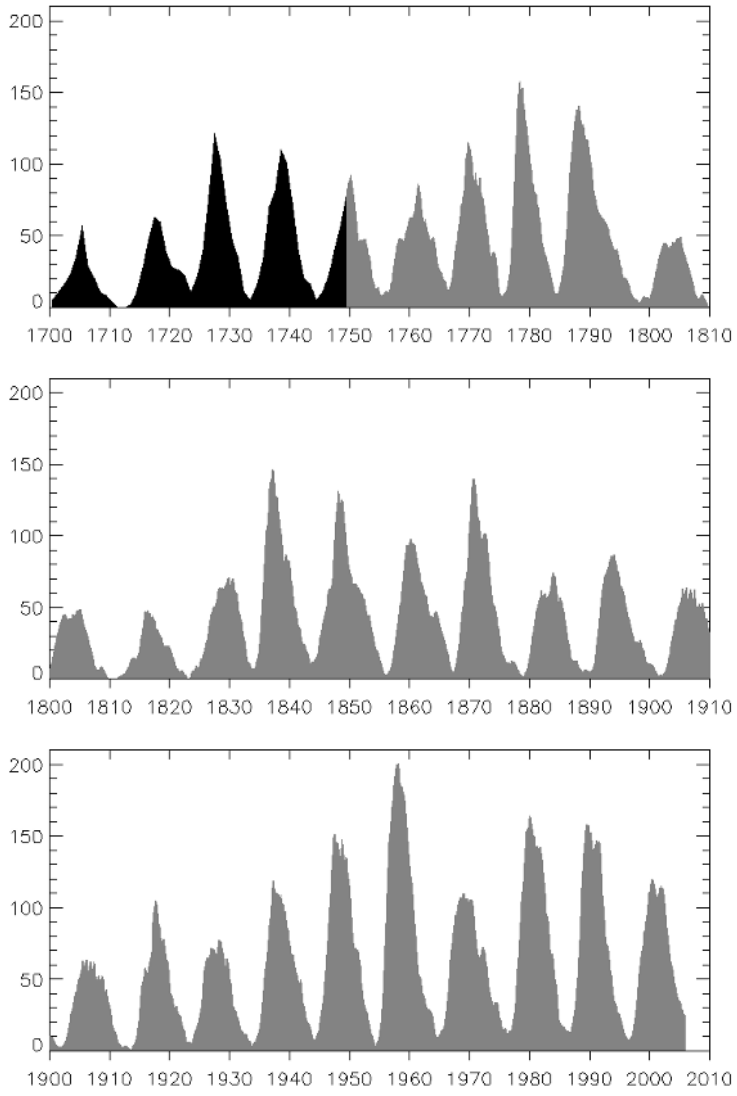

Figure 3.6. The yearly (black, up to 1750) and monthly (gray, from 1750 on) smoothed sunspot numbers. Courtesy: Solar Influences Data Analysis Center (SIDC), Brussels (*http://www.sidc.be*, July 1, 2006).

the following dependence on the longitudinal component of the photospheric field:

$$I_{SXR} \propto \langle |B_{\|}| \rangle^{n} \begin{Bmatrix} n = 1.6\text{–}1.8, \text{ solar maximum} \\ n = 2.0\text{–}2.2, \text{ solar minimum} \end{Bmatrix}$$

Solar cycles are counted from one solar minimum to the next – for example, the current cycle has the number 23 and runs from 1996 until the next minimum expected

after 2006. At low solar activity the Sun's internal magnetic field may be treated to first order as a magnetic dipole. From about 1991 until 2000 the polarity of the Sun's magnetic field was positive – that is, the direction of the magnetic field lines was predominantly directed away from the Sun's photosphere – at its northern heliographic pole and negative – that is, the direction of the magnetic field lines was predominantly directed towards the photosphere – at the Sun's southern heliographic pole (compare with Figure 3.14, color section). A complete magnetic polarity reversal of the Sun's magnetic field hence takes about 22 years, commonly referred to as the 'Hale Cycle'.

The long-term behavior of the 11-yr solar cycle variations and that of even higher periodicities (e.g., the Gleissberg cycle of ~90 years) is highly important in terms of space climate (e.g., Eddy, 1977), whereas for space weather, similarly to terrestrial weather, the momentary conditions at the Sun, in the interplanetary medium and at geospace are of prime importance – that is, forecasts require day by day services. Information derived from the long-term characteristics of individual cycles – like the obviously rapid rise and slow decay phases typically seen in individual cycles, as well as prediction of the strength of the next cycle – appear additionally as helpful means. Recently, Dikpati *et al*. (2006) have developed a flux transport model for the variation /f the Sun's magnetic flux in different cycles based on data from the Michelson Doppler Imager (MDI) onboard the ESA/NASA SoHO spacecraft, being in a halo orbit around the L1 point, 1.5 million km ahead of Earth in the sunward direction. According to the results of this model, solar cycle 24 will be 30–50% stronger in terms of activity, being somehow proportional to the evolution of the magnetic flux in the Sun's photosphere, compared with the current cycle and that activity will start rising at the end of 2007 or early 2008. So far, the prediction of solar cycle strength has unfortunately been relatively uncertain and the estimated peak sunspot number, R, for the coming cycle ranges from less than 50 to over 180 in the various model calculations (Badalyan *et al*., 2001; Dikpati *et al*., 2006).

The solar magnetic field structures the overlying solar corona and hence the global shape of the Sun's corona varies with respect to the phase of the solar activity cycle (Figure 3.7). The faint white light of the solar corona, being 10^6 times less in intensity compared with normal sunlight, is due to scattering of originally photospheric radiation by free electrons in the fully ionized hot outer atmosphere. The existence of the Sun's hot corona with temperatures of some million K above the cooler photosphere, $T = 5762\,\mathrm{K}$, is one of the unsolved astrophysical problems to date. During solar minimum the corona is roughly symmetric with respect to the solar equator and often reveals the presence of large coronal streamers that can be identified from their helmet-like appearances.

Besides EM radiation, the Sun continuously emits a flow of charged particles (plasma) from the corona, the solar wind. With speeds of several hundred km/s, it fills a region in interstellar space, the heliosphere, that occupies distances greatly exceeding 100 AU – that is, it extends out far beyond the distances of the furthest planets of our solar system. The properties of the solar wind and its evolution in the heliosphere control, together with flows of energetic particles in the eV (suprathermal) to MeV energy range, interplanetary space weather conditions. The supersonic solar wind flow

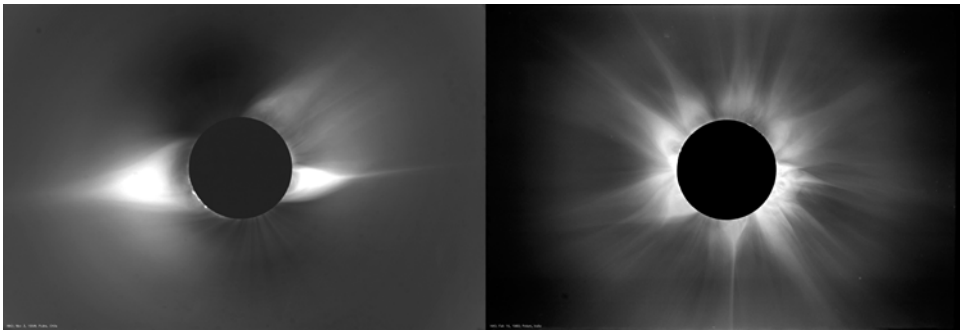

Figure 3.7. Left: the solar corona near solar minimum, as seen during the total solar eclipse on November 3, 1994. Right: the solar corona near solar maximum, observed during the total eclipse on February 16, 1980. Courtesy: High Altitude Observatory, Boulder, CO.

continuously impinges on the Earth's magnetic field. Superimposed on this quasi-steady flow of the solar wind and energetic particles are transient solar wind and particle flows in which the solar wind can blow against the Earth's magnetosphere with speeds of more than 2000 km/s and particle energies up to the GeV range as well as large solar flares, sporadic emissions of EM radiation, that can lead to short-term disturbances of the Earth's atmospheric conditions (see also Chapters 7 and 13). The different forms of energy released by the Sun are summarized in Tables 3.1 and 3.2. The following sections will provide a detailed overview of the solar/interplanetary origins of space weather, including slow and fast solar wind streams, stream interactions, coronal mass ejection events, flares and solar energetic particles.

Table 3.1. Power figures for different forms of solar %nergy output and mass flux estimates.

Total power input	
Solar radiation	$\sim 4 \times 10^{26}$ W
Solar wind from coronal hole	$\sim 4 \times 10^{20}$ W
Large coronal mass ejection	$\sim 1 \times 10^{23}$ W
Large solar flare	$\sim 1 \times 10^{23}$ W
Power at Earth	
Solar radiation	0.137 W/cm^2
Total on Earth	1.73×10^{17} W
Solar wind on disk with 1 R_E	$\sim 1.0 \times 10^{13}$ W
Solar mass loss	
Radiation	4.24×10^{12} g/s
Solar wind	$\sim 1.4 \times 10^{12}$ g/s
Coronal mass ejection	$\sim 1.0 \times 10^{12}$ g/s

Adapted from Schwenn (1988).

Table 3.2. The different forms of solar energy output.

1. Radiation

Spectral range	Source(s)	Characteristics
Radio mm IR	Quiet and disturbed corona, chromosphere	Electromagnetic radiation from moving charged particles (thermal radiation), transient radio emission caused by coronal shocks
White light	Photosphere Chromosphere K-Corona F-Corona	Continuum, thermal radiation Line emission and absorption Spectral lines from 6arious ions Continuum, photospheric light reflected from dust particles
UV	Chromosphere Transition region Corona	Spectral lines from various ions at various ionization stages
EUV	Corona Flares	See UV See X-rays
X-Rays	Upper corona 'Hot' corona, flares, etc.	Spectral lines as for UV, Bremsstrahlung Bremsstrahlung
γ-Rays	Strong flares	Bremsstrahlung and line emission from nuclear processes

2. Particles

Type	Source(s)	Characteristics
Solar wind (magnetized plasma)	Corona	H^+ up to 2 keV, electrons up to 1 keV
'Low energy' particles	Magnetic reconnection, flares, shocks	H, He, C, N, O, up to $\sim$100 keV
Energetic particles	Flares, shocks	Energies up to $\sim$100 MeV, sometimes up to $\sim$GeV

Adapted from Schwenn (1988).

3.2 SPACE WEATHER EFFECTS OF THE QUASI STEADY-STATE CORONA

3.2.1 Slow and fast solar wind streams and their source regions

Soon after the launch of the first satellites in the years around 1960, the existence of a continuous stream of charged particles, termed solar wind – as had been postulated by Biermann (1951) and Parker (1959) – could be verified through *in situ* measurements based on the invention of spaceflight techniques and instrumentation (Neugebauer and Snyder, 1966; Sonett and Abrahams, 1963). The observed solar wind

characteristics showed a systematic two-stream pattern of slow and fast streams, with a 27-day recurrency interval suggestive that their solar source regions rotated with the Sun. For a detailed historical introduction of the early concepts of solar–terrestrial relationships and the discovery of the solar wind, the reader is referred to the article 'The solar atmosphere and space weather' (Bothmer, 2006).

Figure 3.8 (color section) shows observations of the Sun's corona taken at 195 Å, corresponding to temperatures of about 1.5 million K emitted mainly from Fe XII ions, as imaged by the imaging telescope (EIT, see Delaboudinière *et al.*, 1995) onboard SoHO, together with measurements of the geomagnetic activity index Ap (measured by 13 stations world-wide, see Section 3.2.2 and Chapter 7) and the solar wind speed as measured by the WIND satellite for the time period August 27 until September 10, 1996. The two time intervals with a fast and a slow solar wind stream, with speeds at around 400 and 600 km/s, are labeled.

Simultaneous measurements of the solar wind together with X-ray imaging of the solar corona have revealed – since the Skylab era in 1973 – that the sources of fast solar wind streams are 'coronal holes' (CHs) at the Sun. CHs appear as dark regions at the Sun in X-ray and EUV images because the magnetic field lines originating from these areas are rooted with only one end in the solar photosphere, contrar9 to active regions where heated plasma, radiating bright at X-ray and EUV wavelengths, is confined by closed magnetic loops rooted with both ends in underlying bipolar photospheric regions of opposite magnetic polarity. The passage of the fast solar wind stream encountered by the Earth is consistent with the appearance of the coronal hole extension at the central meridian. With a speed of about 600 km/s, it takes roughly 3 days for the solar wind stream to reach the Earth – that is, at times the solar wind has reached Earth's orbit, the solar wind source region, rotating with the Sun, is typically located to the west of the central meridian. In case the low-latitudinal extension of the coronal hole increases in heliolongitude, the time interval of the high-speed flow at 1 AU increases correspondingly. Such low-latitudinal extensions of coronal holes are a prominent feature during the declining phase of the solar activity cycle (e.g., Tsurutani *et al.*, 2006). They can last as quasi-stable co-rotating structures for many months as has been observed – for example, during the Skylab mission in 1974 (Bohlin and Sheeley, 1978).

Due to the Sun's rotation period of 25.4 days, being 27.23 days with respect to Earth, the outward-convected solar magnetic field imbedded in the solar wind gets structured into the pattern of an Archimedian spiral, also termed a Parker spiral, as shown schematically in Figure 3.9. The angle of the magnetic field direction in the ecliptic plane with respect to the Sun–Earth line depends on the solar wind speed, being roughly 45° for a flow speed of 400 km/s, with its polarity being directed outward (+ polarity) or inward (− polarity) depending on the magnetic polarity of the solar source region from which the solar wind stream originates. The angle of the magnetic field direction, φ, is calculated from the solar wind speed V_R at a given distance R with the rotation speed of the Sun Ω_S, as:

$$\varphi = \left(\left| \frac{\Omega_S R}{V_R} \right| \right)$$

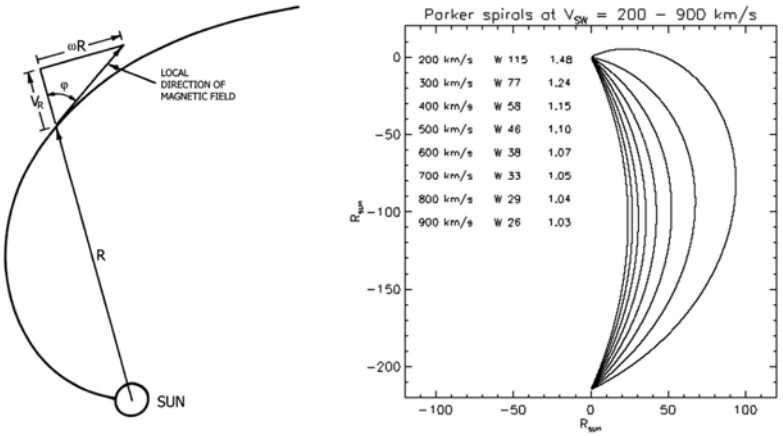

Figure 3.9. Left: schematic geometry of the interplanetary magnetic field (IMF) in the ecliptic plane for a solar wind with speed V_R at a distance R. The situation sketches the observed structure for a solar wind speed of ~400 km/s near 1 AU. The magnetic polarity of the IMF is assumed to be in the anti-sunward direction (i.e., positive). Right: curvature of the Parker spiral at the orbit of Earth for solar wind speeds between 200 and 900 km/s.

The magnetic field swept out by the expanding solar wind is termed the interplanetary magnetic field (IMF). Typical field strengths of the IMF at Earth's orbit are at the order of a few nT and are provided in Table 3.3, together with the average properties of the fast and slow solar wind near Earth's orbit.

As the right EUV image in Figure 3.8 shows, on September 6, 1996 the low-latitude extension of the coronal hole had disappeared behind the limb and the active region, seen to the southeast of the central meridian on August 27, had reached the Sun's west limb. At that time only slow solar wind was encountered at Earth's orbit and the geomagnetic activity index Ap was at low levels. It should be noted here that

Table 3.3. Basic solar wind characteristics near Earth's orbit.

Fast wind	Slow wind
450–800 km/s	<~450 km/s
$n_P \sim 3\,cm^{-3}$	$n_P \sim 7$–$10\,cm^{-3}$
~95% H, 5% He, minor ions and same number of electrons	~94% H, ~4% He, minor ions and same number of electrons – great variability
$T_P \sim 2 \times 10^5$ K	$T_P \sim 4 \times 10^4$ K
$B \sim 5$ nT	$B \sim 4$ nT
Alfvénic fluctuations	Density fluctuations
Origin in coronal holes	Origin 'above' coronal streamers and through small-scale transients

Adapted from Schwenn (1990).

the origin of the slow solar wind remains still a puzzle, but it is commonly believed to originate from the top of coronal streamers in a 'drop-like' manner (Wang and Sheeley, 1998). However, it may often well be that what is believed to be actually slow wind, such as that shown in Figure 3.8, had rather originated from near the edge of a polar coronal hole and expanded non-radially from the higher latitudes down into the ecliptic plane (Bothmer, 1998).

Around times of solar activity minimum, the structure of the heliosphere near the ecliptic plane is dominated by slow solar wind flows and the structure at higher latitudes by fast solar wind flows, as shown in the left part of Figure 3.10 (color section) based on results from the ESA Ulysses mission. Ulysses, launched in 1990, was the first spacecraft to explore the uncharted third dimension of the heliosphere. It orbits the Sun nearly normal to the ecliptic plane at distances between 1 AU and 5 AU (Balogh *et al.*, 2001; Marsden, 2001). The high-inclination orbit was achieved through a gravity assist maneuver at Jupiter. The measurements of the solar wind speed and IMF direction, taken during Ulysses' first and second orbit around the Sun, are displayed in Figure 3.10. During the first orbit, at higher latitudes outside the ecliptic plane, only fast solar wind with speeds of about 750 km/s was encountered by Ulysses. Slow solar wind with speeds less than 450 km/s was confined to heliospheric regions in a narrow belt from about 20°N to 20°S with respect to the heliographic equator. The dominant magnetic polarity observed by Ulysses in both heliospheric hemispheres is consistent with the expected global magnetic polarity of the Sun during the rising phase of odd cycles: positive in the N, whilst negative in the S. Short-term intervals with faster streams seen at lower latitudes can be attributed to either transient streams (which will be described in detail in Sections 3.3.2 and 3.3.4), to streams from equatorward extensions of polar coronal holes (as shown in Figure 3.8) or to low-latitude short-lived coronal holes that occur near times of solar maximum (i.e., around times of magnetic polarity reversal of the Sun – see Figure 3.23 in color section). The relatively simple structure of the corona completely changes at times of solar maximum, as can be seen in the right top part of the solar image in Figure 3.10. The changing coronal structure is directly connected to variability of the solar magnetic field and the processes of its reversal.

3.2.2 Solar wind impact on the Earth's magnetosphere

The physical origins of geomagnetic activity are induction currents caused by the solar wind's electric field impacting the Earth's magnetosphere (see Chapter 4). The solar wind plasma and IMF impose the electric field $\mathbf{E} = -\mathbf{v} \times \mathbf{B}$ on the Earth's magnetosphere, causing a complex system of magnetospheric and ionospheric current systems (e.g., Burton, 1975; McPherron, 1979). Its prime components in both hemispheres are the ionospheric polar auroral electrojets and the near equatorial magnetospheric ring current measured through the AE (Auroral Electrojet) and Dst (disturbed storminess) indices (e.g., Bartels and Veldkamp, 1949; Mayaud, 1980; Rostoker, 1972; Siebert, 1971). The current systems are schematically shown in Figure 3.11 (color section).

The electrojet currents are primarily driven by electrons which spiral along magnetic field lines into the ionosphere where the current density $\mathbf{j}$ is given by $\mathbf{j} = \boldsymbol{\sigma}\mathbf{E}$, with $\boldsymbol{\sigma}$ being the conduction strength and $\mathbf{E}$ being the electric field that drives the current. The electric field $\mathbf{E}$ is of the order of several 10^{-3} V/m at times of weak energy input by the solar wind and reaches magnitudes of several 0.1 V/m during large storms (e.g., Schlegel, 2000).

The electrojets and the ring current are the major drivers of the fluctuations of the Earth's magnetic field. Comparable with the 'Richter–Skala' characterizing earthquake magnitudes, the overall geomagnetic activity index Kp ('Kennziffer Planetarisch') is a quasi-logarithmic parameter, given as daily 3-hr values (from 0 to 9), derived from magnetograms recorded by 13 stations primarily located in the northern hemisphere (Bartels and Veldkamp, 1949; Siebert, 1971). It is important to note that Kp is not only made up of the intensity of the electrojet current systems, but that it also depends on their spatial position – that is, large pressure pulses driven by solar wind flows, causing stronger compressions of the Earth's magnetosphere and subsequent movement of the electrojets to lower latitudes, lead to strongly enhanced Kp values, but will appear less pronounced in the ring current index Dst. Hence, a difficulty in an exact global determination of the absolute magnitude of a given magnetic storm is the superposition of compressional effects and current strengths. The Kp index and the magnetospheric ring current index Dst are both measured in units of nano Tesla (nT). The 3-hr ap-values and the daily Ap index represent the linear counterparts of Kp (a description of the conversion method between Kp and ap can be found at *http://www.gfz-potsdam.de*).

The subsolar point up to which the magnetosphere stretches out in space in the sunward direction can be calculated to first order from the pressure balance between the solar wind's dynamic pressure and the pressure provided by the Earth's magnetic field (e.g., Kivelson and Russell, 1995; Parks, 2003) as $2nmV^2 = B^2(r_{MP})/2\mu_0$, with n, V being the density and velocity of the solar wind, m being the proton mass and B being the strength of the Earth's magnetic field. Any pressure variation of the solar wind causes the magnetosphere to flutter in space like a flag – as shown, for example, by the simulations of Goodrich *et al.* (1998). Any variation of the solar wind electric field $\mathbf{E} = -\mathbf{v} \times \mathbf{B}$ leads in turn to fluctuations of the geomagnetic field, either caused through variation of the solar wind speed or its magnetic field magnitude. Note that, for simplicity, dynamic pressure variations due to solar wind density variations are neglected in this chapter in the subsequent considerations of the causes of geomagnetic activity. A detailed overview of solar wind–magnetosphere coupling functions can be found, for example, in Gonzalez (1990).

Solar wind speed is one of the drivers of geomagnetic activity, but it is well known that the energy transfer into the Earth's magnetosphere also depends crucially upon whether the IMF has a southward-directed (antiparallel) component with respect to the ecliptic plane (direction of the magnetospheric field). For an exact treatment, the IMF components must be considered in the GSM (Geocentric Solar Magnetospheric Coordinates) system (Russell and McPherron, 1973a). A systematic introduction to common coordinate systems was provided by Russell (1971). The main driver of geomagnetic activity is referred to, for short, simply as the southward $-B_z$ component

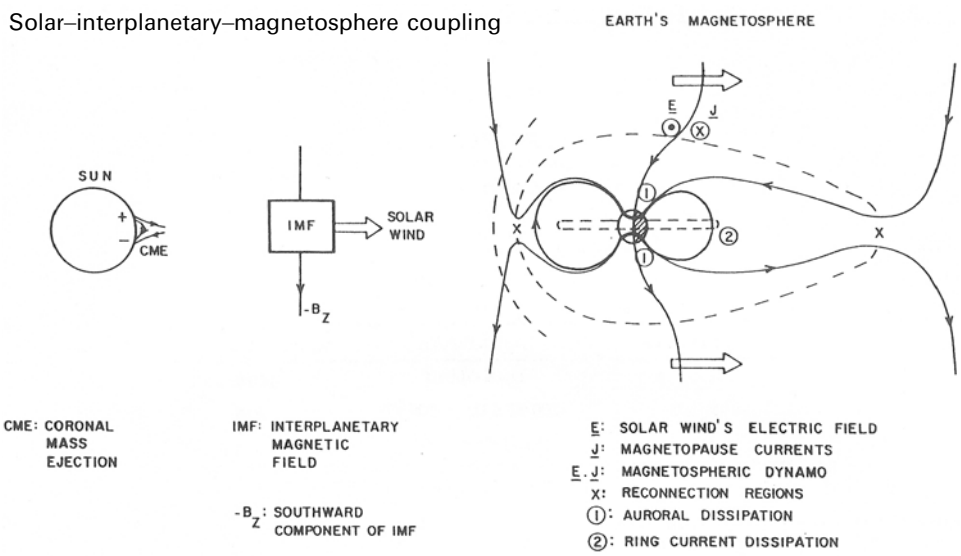

Figure 3.12. Schematic sketch of the magnetic reconnection process of the IMF with the Earth's magnetosphere and the energy injection process into the night-side magnetosphere. Note that the solar wind *per se* does not carry a substantial southward ($-B_z$) component, requiring specific processes – Alfvén waves, stream interactions, coronal mass ejections (CMEs). From Tsurutani and Gonzalez (1997).

of the IMF, leading to magnetic reconnection between interplanetary magnetic fields and magnetospheric fields, as depicted in Figure 3.12 (Tsurutani and Gonzalez, 1997). The reconnection process subsequently leads to plasma injection into the nightside magnetosphere. It should be noted that, should the Earth's magnetic field reverse, a northward component of the IMF would be favorable to reconnection processes.

Figure 3.13 shows the relationship between the interplanetary dawn–dusk electric fields for specific solar wind events (magnetic clouds, see Section 3.3.4) and the peak Dst values in individual geomagnetic storms (Tsurutani *et al.*, 2004). These cases, in which the solar wind speed was low (<400 km/s) – that is, pressure effects on the magnetosphere excited by the solar wind flow can be neglected – show a nearly linear relationship between the electric fields and the Dst values.

3.2.3 Space storms due to co-rotating interaction regions and high-speed flows

The structure of the inner heliosphere near solar minimum resembles the skirt of a 'ballerina', as proposed by Alfvén (1977) and sketched in Figure 3.14 (color section). At some solar radii distance from the Sun, the solar wind in both hemispheres is comprised of the two flows from the large polar coronal holes with opposite magnetic field polarity, yielding the so-called two-sector structure of the IMF. An observer (e.g., located at Earth) would pass through the upper and lower parts of the ballerina skirt during one solar rotation – that is, would record phases of opposite polarity of the IMF.

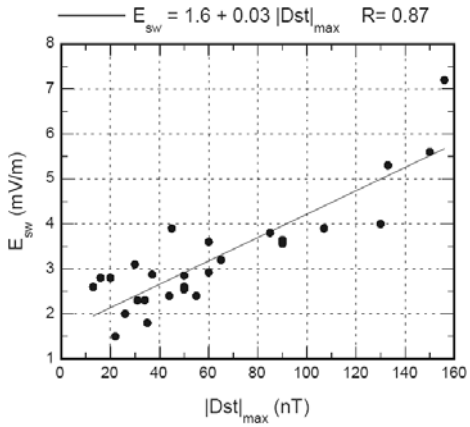

Figure 3.13. Relationship between the interplanetary electric field caused by the solar wind, E_{SW}, and the maximum Dst values of different geomagnetic storms. The individual storms were caused by slow transient solar wind streams with internal southward-directed magnetic fields (slow magnetic clouds). From Tsurutani *et al.* (2004).

A dominant feature of the heliosphere near solar minimum, especially in the declining phase of a solar cycle associated with the fast/slow stream solar wind pattern, is the long-lasting formation of co-rotating interaction regions (CIRs) followed by high speed (>600 km/s) solar wind streams. CIRs are caused by fast solar wind streams catching up slower solar wind streams ahead that had originated in solar longitude westward of the fast streams as viewed from Earth. In the stream interaction process, low-speed wind is compressed in its trailing edge and deflected in the sense of solar rotation, whilst high-speed wind is compressed in its leading portion and slightly deflected towards the opposite direction. Within CIRs the magnetic field magnitude is increased and the field vector may be deflected out of the ecliptic plane (e.g., Tsurutani *et al.*, 2006).

Observations of the corona taken simultaneously with solar wind data obtained by near-Earth satellites have revealed that recurrent – the period of solar rotation is 25.4 days and hence 27.3 days as seen from Earth – geomagnetic storms are caused by fast solar wind streams with speeds typically in the range of 500–800 km/s (Burlaga and Lepping, 1977; Crooker and Siscoe, 1986; Tsurutani, 2001). Contrary to Bartels' earlier belief that recurrent storms are due to magnetic active regions at the Sun, we now know that they stem from coronal holes – that is, rather magnetic 'quiescent' solar regions. Recurrent geomagn%tic storms are dominant especially in the declining phase of sunspot cycles (e.g., Richardson *et al.*, 2001) because at these times large polar coronal holes exhibit persistent low-latitude extensions over time periods of several months (e.g., Tsurutani *et al.*, 2006). Figure 3.15 shows the variation of the Kp index during 1974 organized in the classical 'Kp Musical Diagram' together with a yearly summary plot of the IMF B_z-component, Dst index, solar wind speed and IMF magnitude B. In the declining phase of cycle 21, high-speed solar wind streams from low-latitudinal extensions of the polar coronal holes persisted for months and led to recurrent patterns of enhanced geomagnetic activity.

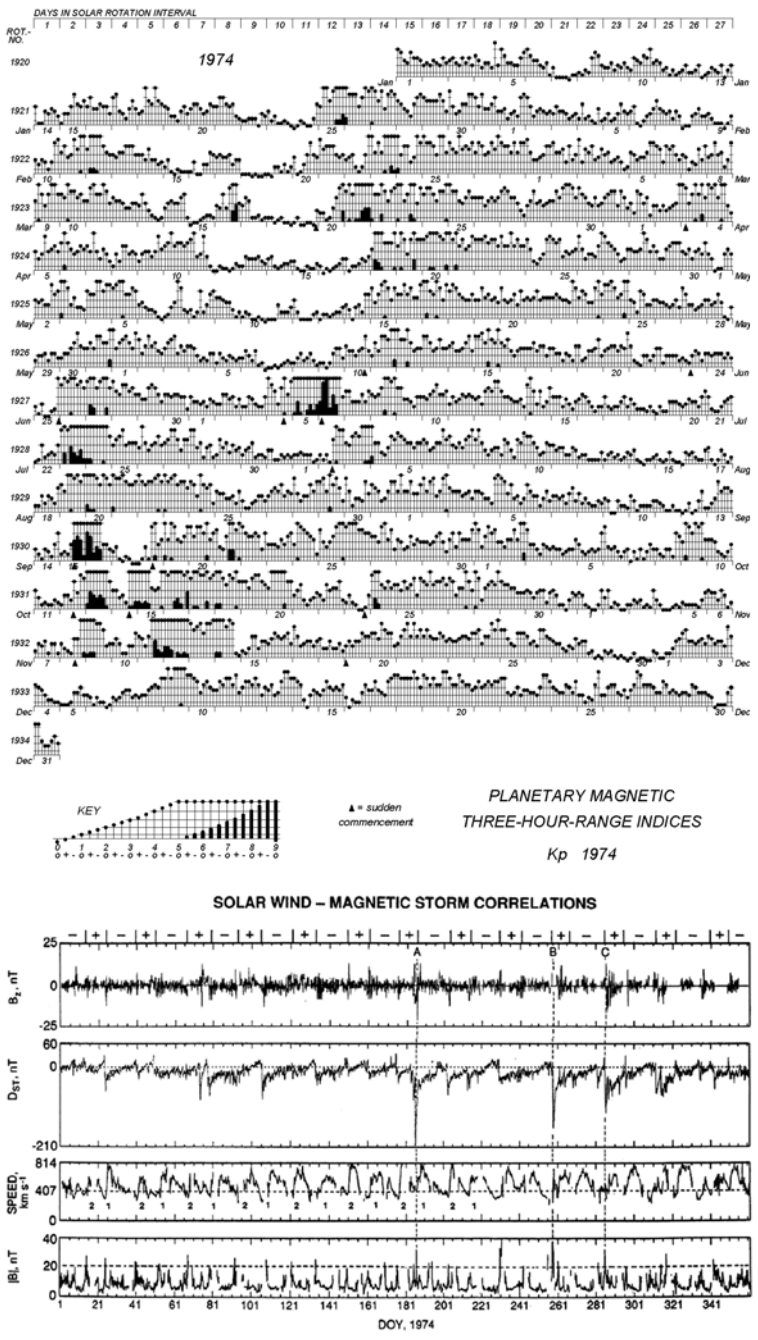

Figure 3.15. Top: the Kp 'musical diagram' for 1974. Bottom: southward component B_z of the IMF, Dst index, solar wind speed and IMF magnitude B in 1974. Labeled on top is the magnetic polarity of the IMF. Bottom diagram courtesy: Tsurutani (2006).

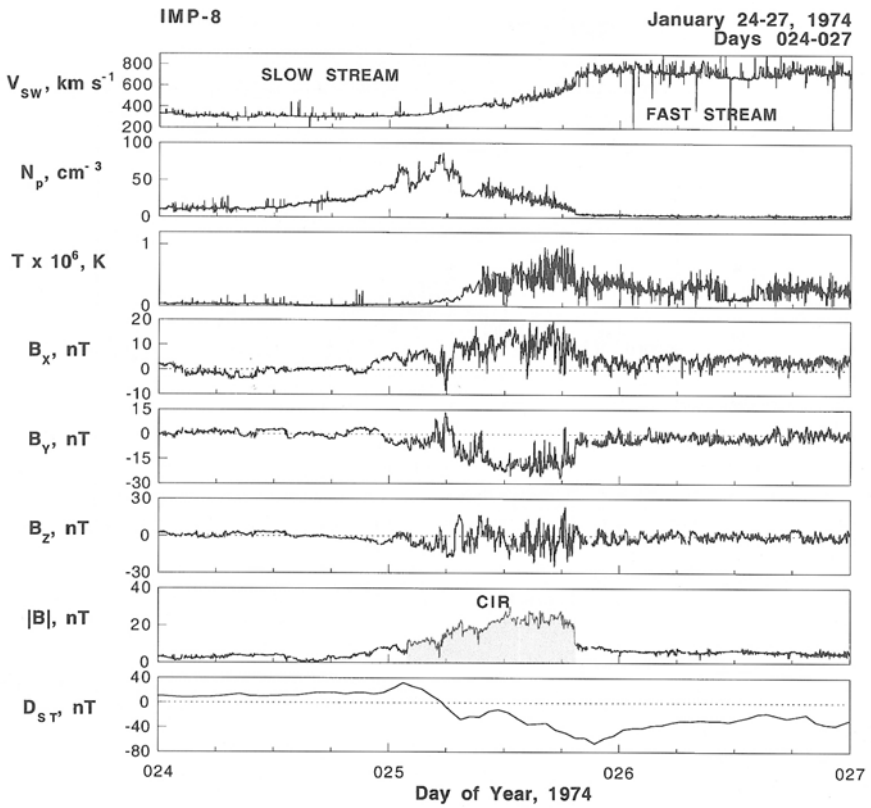

Figure 3.16. Solar wind measurements from IMP (Interplanetary Monitoring Platform) 8 of a co-rotating interaction region (CIR) formed between a slow and fast solar wind stream in January 1974 and the geomagnetic response as provided by the Dst index. Plotted from top to bottom are: solar wind speed, proton density and temperature, Cartesian components and magnitude of the IMF and Dst. From Tsurutani (2000).

Figure 3.16 shows an archetypal example of a geomagnetic storm that was triggered by a CIR and a subsequent high-speed solar wind stream observed in January 1974. Geomagnetic activity peaks within the CIR because of the compression and fluctuations of the IMF and Alfvénic waves (Tsurutani and Gonzalez, 1997). Following the CIR-related storm period, typically lasting for time intervals of less than a day, within the high-speed stream itself geomagnetic activity is triggered at lower levels by large amplitude IMF $-B_z$ fluctuations caused by Alfvénic waves (Tsurutani and Gonzalez, 1997). These fluctuations, as shown in Figure 3.17, stimulate prolonged substorm activities which lead to high-intensity long-duration continuous AE activity (HILDCAA) (Tsurutani and Gonzalez, 1987) in which energetic proton injections into the nightside magnetosphere up to about $L = 4$ (shell parameter of the McIlwain coordinate system, see Chapter 4) occur (Tsurutani *et al.*, 2006). Additionally to the protons, relativistic electrons at MeV energies, sometimes called 'killer electrons' because they can lead to surface charging and subsequent discharging

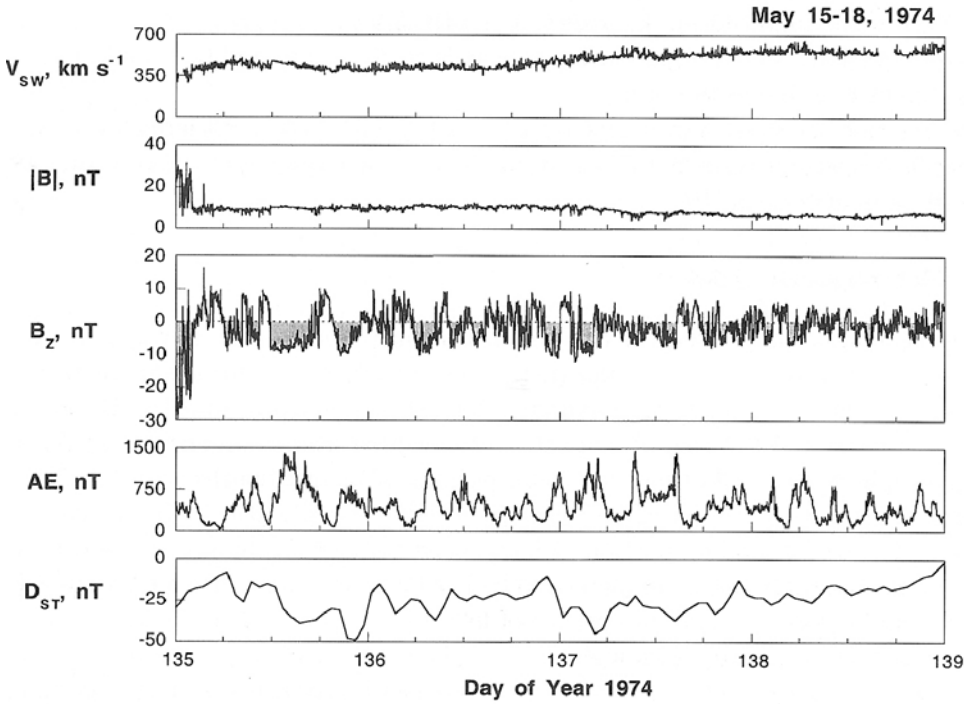

Figure 3.17. Example of a high-intensity long-duration continous AE activity (HILDCAA). From Tsurutani and Gonzalez (1997).

processes that may damage or disable satellite components, have been detected during intervals of high-speed streams (see also Chapter 6 and Baker, 2004).

CIR-related activity and subsequent wave activity are the reasons for the typically observed two-step behavior in recurrent storms (e.g.. Borello Filisetti *et al.*, 1988; Burlaga and Lepping, 1977). CIR-related shocks commonly form at distances around 2 AU from the Sun, though some have been observed by the Helios spacecraft at distances as close as 0.3 AU (Schwenn and Marsch, 1990), depending on whether the plasma gradients of the interacting streams exceed critical thresholds in terms of Alfvén and sound speeds. Charged particles are accelerated by CIR shocks and can stream along the magnetic field lines to heliospheric distances far away from the local acceleration sites, as has been frequently observed during the Ulysses mission (Lanzerotti and Sanderson, 2001). The physics of CIRs in the 3-D heliosphere has been explicitely summarized in reviews on these topics by Balogh and Bothmer *et al.* (1999), Crooker *et al.* (1999), and Gosling and Pizzo (1999). Depending on the spatial structure of the coronal holes, the tilt of the Sun's rotation axis and the structure of the global corona, systematic spatial patterns of compression regions or forward and reverse shock pairs may form (Gosling and Pizzo, 1999) and might have been the cause of systematic out-of-the-ecliptic deflection of the IMF in CIRs – like those reported by Rosenberg and Coleman (1980).

The strength and duration of an individual geomagnetic storm caused by a CIR and related high-speed solar wind stream can be quite variable, depending on the amount of compression of the IMF and the direction of the B_z component as well as its duration in case of a southward direction and, finally, the spatial size of the following high-speed flow (e.g., Richardson *et al.*, 2006). However, field intensities of the IMF at 1 AU within CIRs at 1 AU commonly do not exceed values of about 20 nT, and the variation of the solar wind speed compared with that of the slow solar wind is about a factor of 2. This is the prime reason geomagnetic storms caused by CIRs usually do not exceed Kp values of 7+, as has been inferred by Bothmer and Schwenn (1995) from detailed analysis of satellite data for 43 geomagnetic storms during the years 1960–1990 with peak Kp values of 8− and larger, in agreement with the results of Gosling (1993) and Richardson *et al.* (2001). As will be shown in Sections 3.3.4 and 3.4, all major space storms are caused by solar eruptions. The typical profiles of a CIR-related storm compared with that caused by a transient solar wind stream from a coronal mass ejection (CME, see Section 3.3.3) is shown in Figure 3.18.

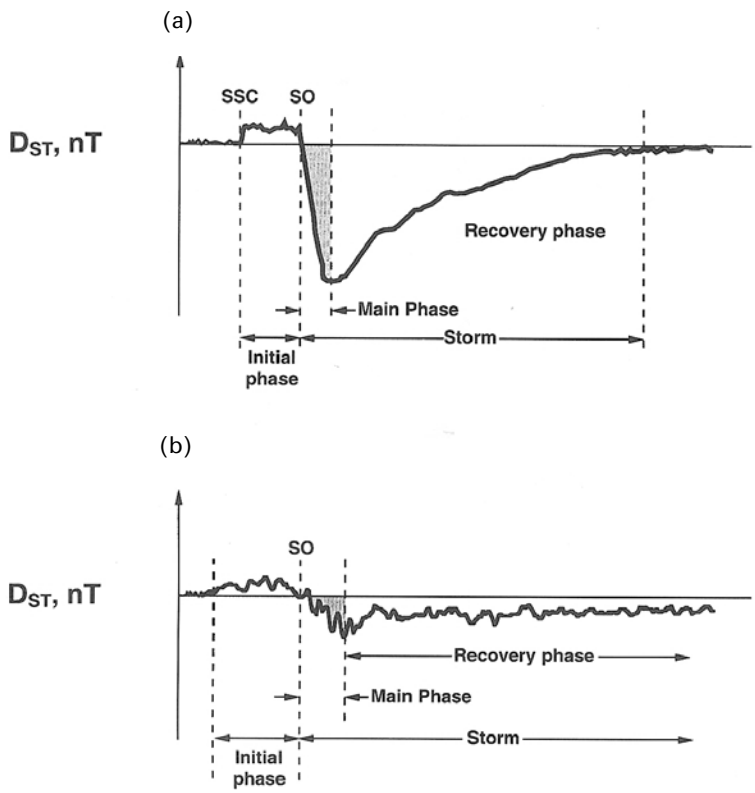

Figure 3.18. Typical Dst profiles for geomagnetic storms generated by an interplanetary coronal mass ejection (a) and a CIR/high-speed stream (b). SSC stands for sudden storm commencement, caused by a short-term compression of the magnetosphere through the transient flow. SO denotes the storm onset. From Tsurutani (2000).

3.3 SPACE WEATHER EFFECTS OF THE DYNAMIC CORONA

3.3.1 The ever changing photospheric magnetic field

Independently of the sunspot phenomenon, the photosphere of the Sun is always occupied by a magnetic field, as can be seen from comparison of SoHO/MDI/EIT (for an overview on the EIT and MDI instruments see Delaboudinière *et al*., 1995, and Scherrer *et al*., 1995) images in Figure 3.19 (color section) with GONG (Global Oscillation Network Group) white-light images taken from ground-based observatories. For further comparison, SoHO/EIT 195, 284, 304 Å images and a Catania H_α image have been added. Permanently small-scale changes take place in the photosphere where magnetic bipoles (e.g., Wang and Sheeley, 1989) of various spatial scales emerge, the smaller ones with low intensities replenishing themselves in time periods of about 40 hours are known to give rise to the black and white (salt and pepper) pattern in MDI magnetograms, the so-called magnetic carpet. Figure 3.20 shows how the small-scale magnetic field of the photospheric carpet connects the network on the spatial scale of supergranulation cells, while larger scale magnetic fields extend up into the corona (Aschwanden, 2004).

Figure 3.21 (color section), taken by the TRACE (Transition Region And Coronal Explorer) mission, shows the fine structure of the solar corona in unprece-

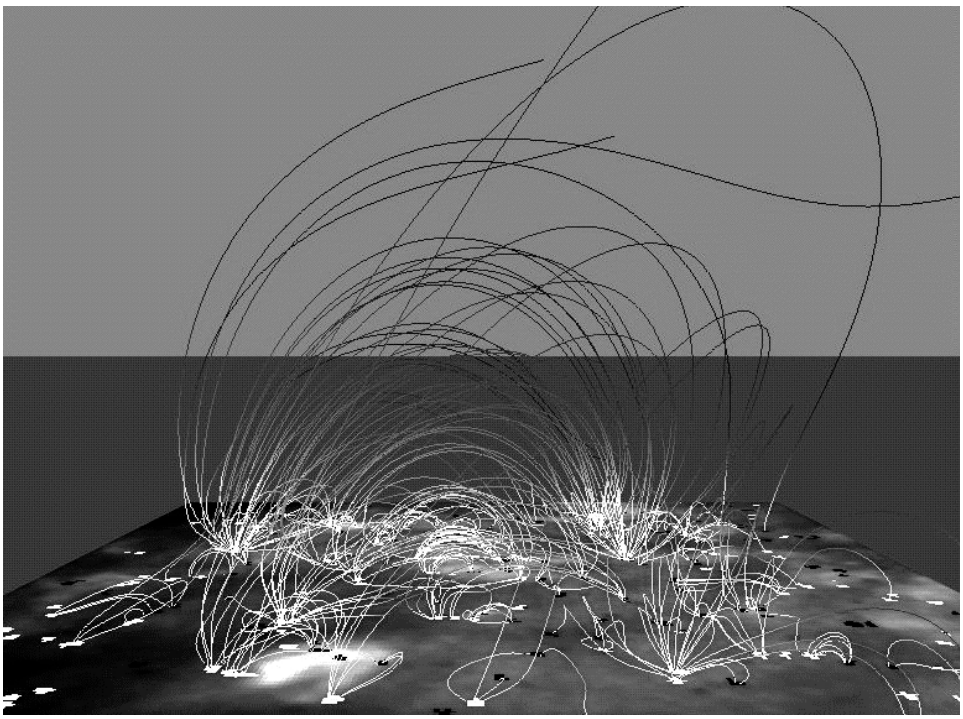

Figure 3.20. SoHO/MDI/EIT illustration of the magnetic carpet. Courtesy: SoHO/MDI/EIT Consortium.

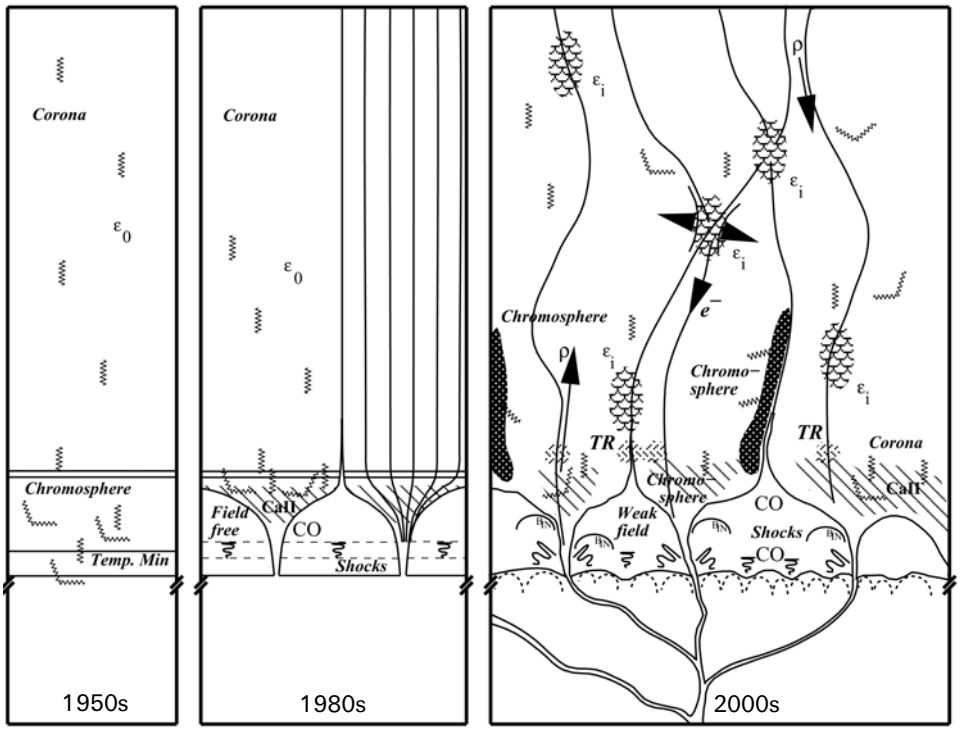

Figure 3.22. Left to right: changing physical concepts describing the structure of the solar corona from a gravitationally stratified atmosphere in the 1950s to an inhomogeneous turbulent profile today. From Aschwanden (2004).

dented spatial resolution. The image (with another color table on the right) of coronal loops over the eastern limb of the Sun was taken in the TRACE 171 Å pass band characteristic of a plasma at 1 MK temperature on November 6, 1999 at 02 : 30 UT. The image was rotated over 90 degrees in the clockwise direction. On the basis of new observations, Figure 3.22 shows how views of the physics of the solar corona have changed in time from a quasi-static, simple, gravitationally stratified solar atmosphere to a complex, highly time-variable system made up out of small-scale magnetic networks (Aschwanden, 2004). Although the Sun's atmospheric layers are ever changing on small scales, most of the time the interplanetary medium seems practically unaffected at the distance of Earth by the Sun's activity on small scales – associated, for example, with micro-flare activity – so that the main role for space weather effects is left to the solar wind from the open regions of the Sun's magnetic field (i.e., coronal hole flows).

With increasing solar activity, more and more magnetic bipoles, with the most intense areas in terms of magnetic flux seen as sunspots, occupy the solar photosphere, as can be seen in the SoHO/MDI images presented in Figure 3.5. Hence, the relatively simple structure of the solar corona described in terms of the ballerina model (Section 3.2.3) changes drastically, and the basic structure of the solar magnetic field and

corona comprised of open fields at polar latitudes and closed fields distributed at lower latitudes vanishes. Figure 3.23 (color section) shows the changing structure of the Sun's EUV corona at 195 Å in three different images, taken by SoHO/EIT in 1996 near solar activity minimum, in the increasing phase of the solar cycle in 1998 and in 1999 close to solar activity maximum. At these times, more and more magnetic flux emerges into the photosphere and violent solar eruptions and flares, likely caused through magnetic reconnection processes, start dominating the daily 'solar weather'.

3.3.2 The explosive corona – coronal mass ejections and flares

The observation of a large white-light solar flare on September 1, 1859 by Richard Carrington (1860) and his subsequent conclusion that the flare might have been indicative of solar processes, triggering the major magnetic storm on Earth which occurred about 17 hours later, motivated scientists to try and establish the physical relationships between these two phenomena, without obtaining unambiguous results, today known as the 'solar flare myth' (Gosling, 1993a). The main reason for the long-undiscovered true physical links in solar–terrestrial physics is primarily related to the faintness of the solar corona, being 10^6 times less bright in intensity than the visible solar disk (i.e., the photosphere). Observations of the corona remained elusive until Bernhard Lyot (1939) invented the coronagraph, the first telescope able to detect the faint corona from Earth apart from total solar eclipses. A coronagraph essentially detects photospheric light scattered from free electrons in the hot outer solar atmosphere. This polarized light is also referred to as the Thomson-scattered light of the K-corona, with K denoting the German word *kontinuierlich*. The continuum corona is the prime ingredient of the white-light features visible in coronagraph images. A scientifically highly important feature of the solar corona is that the plasma-β is typically less than 1 – that is, the thermal pressure of the plasma is much smaller than its magnetic pressure and, hence, the ionized atoms and electrons are structured by the Sun's magnetic field.

In the early 1970s, for the first time coronagraphs were developed for space missions and successfully flown on the OSO (Orbiting Solar Observatory) 7 mission and some years later onboard Skylab, subsequently with the P78-1 and Solar Maximum Missions (SMM) and currently on SoHO (e.g., St. Cyr *et al.*, 2000). The first observations of the solar corona, at time cadences of several tens of minutes, recorded by spaceborne coronagraphs yielded a big surprise: The frequent appearance of large coronal 'bubbles', exceeding greatly the Sun's size at some solar radii distance, were propagating outward into space at speeds of several hundreds of km/s in the telescope's fields of view which were about 2–6 solar radii (Hildner *et al.*, 1976; Howard *et al.*, 1982, 1997; Koomen *et al.*, 1974; Sheeley *et al.*, 1985; St. Cyr *et al.*, 1999; Yashiro *et al.*, 2004). These large-scale coronal transients are today commonly referred to as coronal mass ejections or CMEs.

Figure 3.24 (color section) shows a typical, fast CME observed by SoHO on August 5, 1999. The speed of the CME was initially about 700 km/s, but in this case it was accelerated to about 1000 km/s during its outward motion up to distances of at least 10 solar radii, as derived from the measured velocity increase in the field of view

($\sim$2–30 R_S) of the SoHO LASCO (Large Angle Spectrometric Coronagraph, see Brueckner *et al.*, 1995) instrument.

SoHO has so far recorded more than 10,000 CMEs (*http://cdaw.gsfc.nasa.gov/CME_list/*) with unprecedented resolution in space and time, allowing very detailed studies of their white-light structures, origins and kinematics (e.g., Chen *et al.*, 2000; Cremades and Bothmer, 2004). CMEs carry roughly 5×10^{12} to 5×10^{13} kg of solar matter into space (e.g., Howard *et al.*, 1997; Vourlidas *et al.*, 2002). Their speeds are often fairly constant over the first couple of solar radii, with the prime acceleration taking place commonly just within the first solar radii or less (e.g., St. Cyr *et al.*, 1999). However, some CMEs are accelerated sufficiently longer, as was the case in the sample event shown here.

The average speed of CMEs is on the order of 400 km/s, though some are substantially slower and others reach extremely high speeds, exceeding even 3000 km/s (e.g., Gopalswamy *et al.*, 2005). On average, the kinetic energy of a CME is around 10^{23} to 10^{24} J (e.g., Vourlidas *et al.*, 2002), which is comparable with the energy of large solar flares. Their angular widths are in the range of 24° to 72° (Yashiro *et al.*, 2004). During low solar activity, CMEs occur at low heliographic latitudes, but almost all around the Sun at times near solar maximum. Near solar minimum, the daily average CME rate is $\sim$1, while it is $\sim$4 near solar maximum (Yashiro *et al.*, 2004). Table 3.4 summarizes the basic characteristics of CMEs.

CMEs are best associated with eruptive prominences (disappearing filaments) – as shown by Webb and Hundhausen (1987) – and to a lesser extent with solar flares, though the individual phenomena may occur without each other (e.g., Subramanian and Dere, 2001). Gopalswamy *et al.* (2003) found more than 70% of the SoHO/LASCO CMEs during the years 1996–2002 to be associated with prominence eruptions. Flare-associated CMEs seem to be strongly connected to magnetic active regions, as evident from their brightness in low coronal EUV observations and from the enhanced underlying photospheric magnetic flux. This finding seems plausible, as one can easily imagine that stronger changing photospheric flux gives rise to coronal heating and flaring processes in active regions occurring at preferential lower heliographic latitudes in the course of the solar cycle, following the well-known butterfly pattern of sunspots (*http://science.msfc.nasa.gov/ssl/pad/solar/images/bfly.gif*).

In a recent study Zhang *et al.* (2001) analyzed in great detail – for a number of events – the temporal and physical relationship between coronal mass ejections and flares. In these cases the CMEs did slowly evolve through the fields of view of the

Table 3.4. Basic characteristics of CMEs.

Speed	$<$300–$>$3000 km/s
Mass	5×10^{12}–5×10^{13} kg
Kinetic energy	10^{23}–10^{24} J
Angular width	$\sim$24°–72°
Occurrence frequency	$\sim$1–$\sim$4 (sol. min.–sol. max.)

From Bothmer (2006).

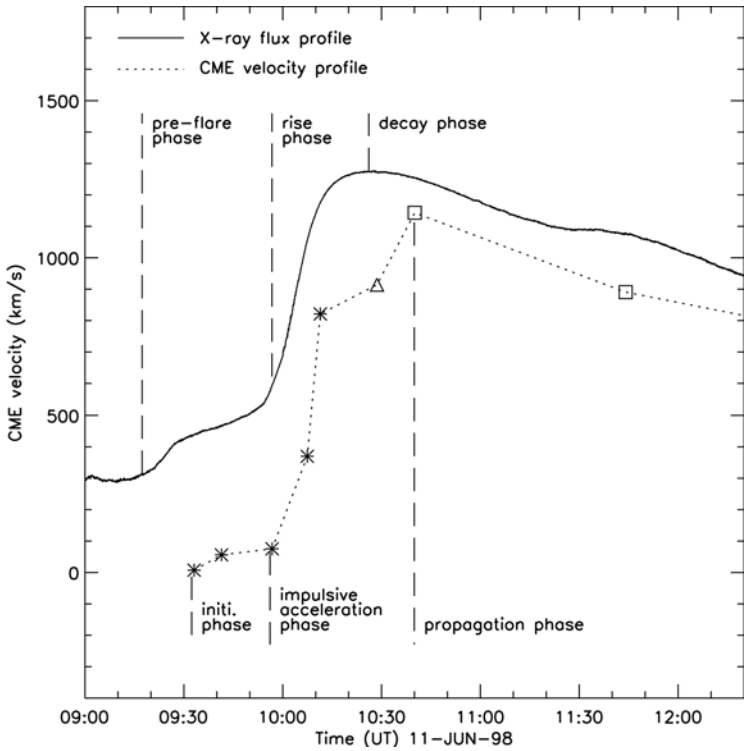

Figure 3.25. Speed–time profile for the CME on June 11, 1998 shown together with the flux profile of the associated X-ray flare. Note the three phases of CME acceleration and flare intensity evolution. From Zhang *et al.* (2001).

LASCO coronagraphs. According to their results, the kinematic evolution of flare-associated CMEs shows a three-phase development: an initiation, an impulsive acceleration and a propagation phase. In the initiation phase the CME slowly rises for a time period of several tens of minutes followed by the onset of the X-ray flare and the impulsive acceleration phase of the CME until, finally, the acceleration ceases and the CME starts propagating farther out at a constant speed, as shown in the velocity–time diagram in Figure 3.25 derived for the CME observed on June 11, 1998. Certainly, future high time-cadence solar observations will shed more light on the physical details of the onset of CMEs.

CMEs develop rapidly into large-scale objects with diameters bigger than the size of the Sun itself, as shown in Figure 3.26 (color section) from the study of structured CMEs performed by Cremades and Bothmer (2004). The typical three-part structure of the CME evident in Figure 3.26, consisting of a bright leading edge, a dark void and a bright trailing core, is evident already in the SoHO/EIT 195 Å images of the low corona (shown at the top). As Cremades and Bothmer (2004) pointed out, CMEs originate from magnetic loop/flux rope systems that likely already existed in the low corona at heights below about 1 solar radii and often expand in a self-similar manner into the field of view ($\sim$2–6 R_S) of the LASCO/C2 coronagraph. In the bottom right

image of Figure 3.26 the identified source region of the CME is located in a composite SoHO/EIT/MDI image. The purple and blue colors denote regions of opposite magnetic field polarity in the photosphere.

Cremades and Bothmer (2004) found that bipolar regions in the photosphere are generally the underlying source regions of CMEs, independent of whether these were active regions or ones in which magnetic flux was already decaying and had persisted considerably longer in time. At higher latitudes the source regions of CMEs were typically more spatially extended and associated with prominences.

In a systematic study of the CMEs' source region properties, Cremades and Bothmer (2004) found that the 3-D topology of structured CMEs observed in the field of view of LASCO/C2 can be classified according to a basic scheme in which the fundamental parameters are the heliographic position and orientation of the source region's neutral line separating the opposite magnetic polarities. If one assumes that the average orientation of the neutral lines separating bipolar regions as CME sources follows Joy's law, the characteristic white-light shape of a CME seen in the FOV of a coronagraph can be explained naturally through the basic scheme presented in Figure 3.27. CMEs originating from the visible solar disk are seen at the east limb in cross-section and sideways at the west limb. The scheme reverses for CMEs originating at the back-side of the Sun, as viewed from the position of the observer assumed in Figure 3.27. Howard *et al.* (in press) have successfully reproduced the white-light

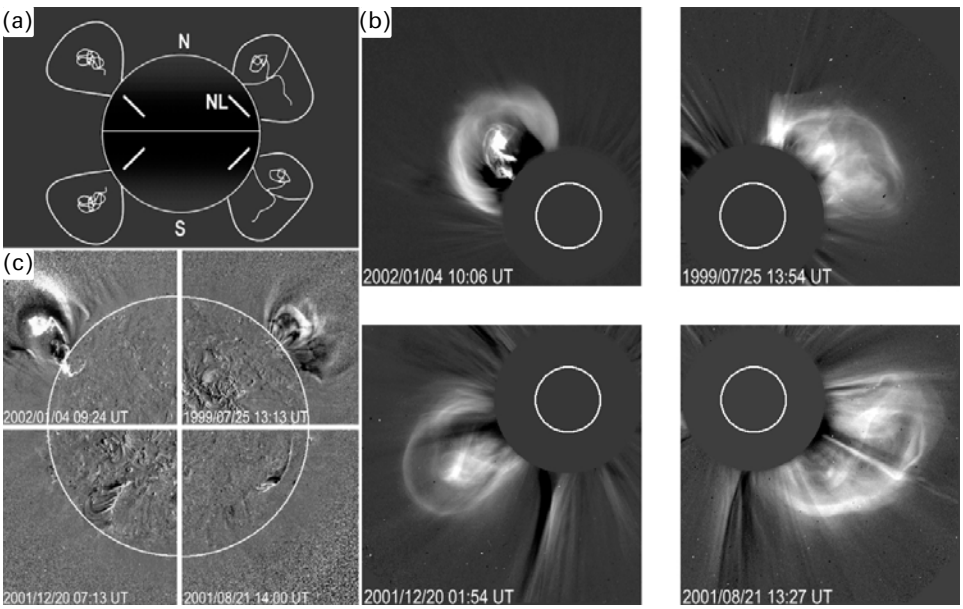

Figure 3.27. (a) Basic scheme showing the extreme cases of CME projection for front-side events. NL stands for neutral line (i.e., polarity inversion line separating the two opposite photospheric polarities). (b) Four projected CMEs seen by SoHO/LASCO C2 representing the scheme. (c) 195-Å signatures identifying the source regions of CMEs. For the northern events eruptive signatures were selected while for the southern ones post-eruptive features are shown. From Cremades and Bothmer (2004).

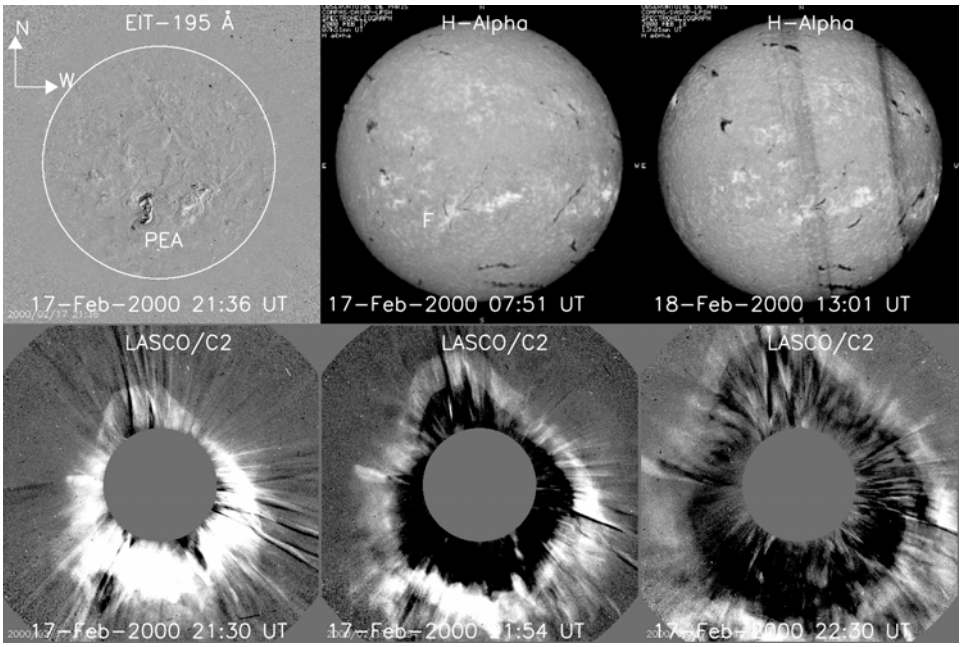

Figure 3.28. Top left: SoHO/EIT 195-Å image showing the post-eruptive arcade which formed after the front-side halo CME observed by LASCO/C2 on February 17, 2000. Middle and right images: Hα images from the Paris/Meudon Observatory showing the disappearance of the associated filament. Bottom images: SoHO/LASCO/C2 images showing the near-Sun development of the halo CME. The speed of the CME was about 600 km/s. Note the asymmetry of the halo in the NE to SW direction. From Tripathi *et al.* (2004).

pattern for the CMEs shown in Figure 3.27 through a graduated cylindrical shell (GCS) model, hence supporting the findings by Cremades and Bothmer (2004) on the 3-D structure of CMEs.

The apparent profile of an individual CME may differ more or less from the basic scheme presented in Figure 3.27 because of the solar variability of the fundamental underlying parameters – for example, many neutral lines are not straight but have rather complicated topologies, especially in active regions. The degree of correspondence with the scheme also depends on the absolute values of source region lengths, which will impose difficulties for small values typically found in compact active regions.

Contrary to the white-light structure of the CMEs shown in the scheme in Figure 3.27, events originating from near the center of the solar disk appear as unstructured halos (Howard *et al.*, 1982), as shown in the bottom sequence of images in Figure 3.28. The middle and right images at the top show the disappearance of a filament in H_α, the left image shows a post-eruptive EUV arcade that developed after the CME's onset in its low coronal source region (Tripathi, Bothmer and Cremades, 2004). Multi-wavelength observations of the CME's source region are shown in Figure 3.29 (color section) based on EUV 195 Å images from SoHO/EIT, soft X-ray observations

from Yohkoh and H_α-images from the French Observatory at Paris/Meudon (*http://bass2000.obspm.fr/home.php*). The view is complemented by SoHO/MDI magnetograms.

From the SoHO observations it seems obvious that CMEs originate from localized spatial source regions in the two solar hemispheres. In the case presented here the front-side halo CME did several days later pass Earth's orbit, as identified from WIND and ACE (Advanced Composition Explorer) solar wind data (Bothmer, 2003; Yurchyshin, 2001). The calculated orientation of the CME's major axis, as inferred from white-light observations, was found to lie almost normal to the ecliptic plane, in agreement with the expected orientation of the filament in the CME's source region. In this case the magnetic field configuration was consistent with that expected from MDI observations (Bothmer, 2003).

The low-corona EUV signatures of CMEs on the solar disk can be used to discriminate whether they are front-sided or back-sided events (e.g., Tripathi, Bothmer and Cremades, 2004; Zhukov and Auchère, 2004). These features include 'EIT waves' and 'dimmings' (Figure 3.30). The coronal waves seen by EIT typically propagate at speeds of several hundreds of km/s, but are not seen for all CMEs (Klassen *et al.*, 2000; Thompson, 2000; Wang, 2000). According to Tripathi *et al.*, EUV post-eruptive arcades seen for a couple of hours after the onset of a CME are a definitive CME proxy, even without the availability of simultaneous coronagraph observations. Intensity brightening in soft X-rays near the onset time of CMEs (as seen in Yohkoh observations, often of sigmoidal structure), EUV dimmings and prominence eruptions are other good CME proxies (e.g., Canfield *et al.*, 1999).

It is important to summarize that solar flares emit short-term flashes of EM radiation over a wide spectral range which at the time of their observation cause effects on the Earth's ionosphere and atmosphere, as pointed out in Chapters 7 and 13, while CMEs are responsible for the convection of magnetized solar plasma into interplanetary space, with the fastest (>1000 km/s) CMEs typically causing the most intense interplanetary disturbances and, in case of the presence of a southward B_z at Earth's orbit, the strongest magnetic storms as well (e.g., Bothmer, 2004; Bothmer and Schwenn, 1995; Gosling, 1993; Tsurutani, 2001). Depending on the speed of the CME, the delay of the geomagnetic storm with respect to the solar event ranges from less than a day to several days (e.g., Brueckner *et al.*, 1998).

3.3.3 Interplanetary consequences of coronal mass ejections – shocks and ICMEs

The first *in situ* measurements of the solar wind already showed that, apart from slow and fast solar wind streams as described in Section 3.2.1, the interplanetary medium is frequently disrupted by transient flows, often associated with interplanetary shock waves discernible as strong discontinuities in which all plasma parameters (velocity, density, temperature) and the magnetic field intensity abruptly increase (e.g., Gosling *et al.*, 1968). Figure 3.31 shows an interplanetary shock wave detected by Helios 1 on May 13, 1981 (Sheeley *et al.*, 1985). The plasma speed abruptly increased from 600 km/s to over 1200 km/s.

Simultaneous operations of the Solwind coronagraph onboard the P78-1 satellite

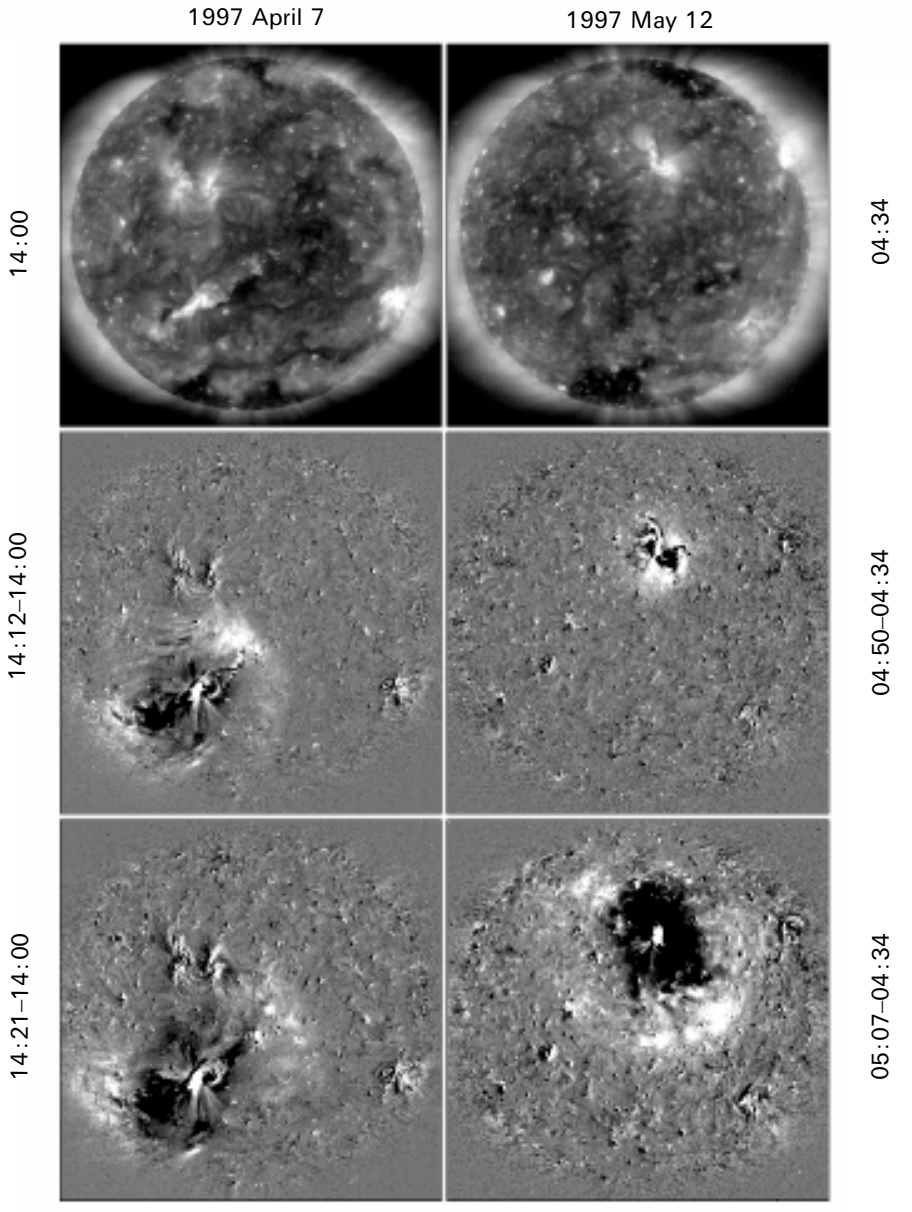

Figure 3.30. EIT waves imaged by SoHO/EIT at 195 Å in the solar corona associated with CMEs on April 7, 1997 and May 12, 1997. From Wang (2000).

and the German/US sun-orbiting spacecraft Helios 1, which explored the *in situ* characteristics of the inner heliosphere over the range 0.3–1 AU in the ecliptic plane, together with its sister spacecraft Helios 2, allowed for the first time during the years 1979–1982 to directly study the interplanetary effects of CMEs (Bothmer and

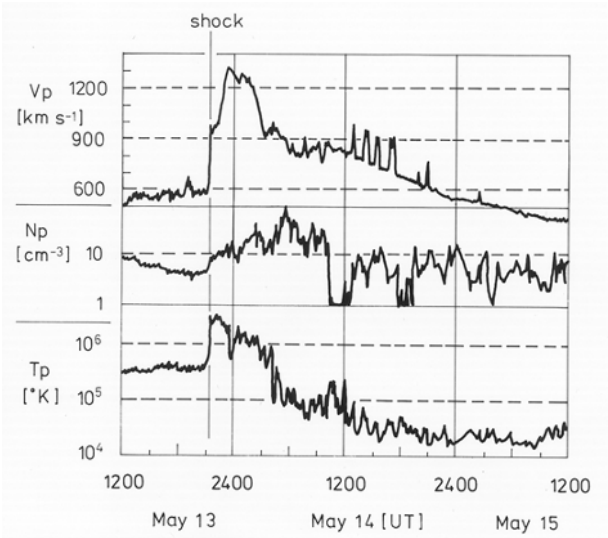

Figure 3.31. An interplanetary shock wave detected by Helios 1 on May 13, 1981. Solar wind parameters form top to bottom: proton bulk speed, density and temperature. From Sheeley *et al.* (1985).

Schwenn, 1996; Sheeley *et al.*, 1985). Sheeley *et al.* (1985) found that 72% of the interplanetary shock waves detected by Helios 1 were associated with large, low-latitude mass ejections on the nearby limb, with most of the associated CMEs having had speeds in excess of 500 km/s, some even having had speeds in excess of 1000 km/s. These observations clarified that CMEs are the sources of interplanetary shock waves and not solar flares, as was commonly believed until then (e.g., Chao and Lepping, 1974). Today it is well known that flares and CMEs can occur without each other, although the most intense events commonly occur jointly, and the concrete physical relationships between the two phenomena is a subject of ongoing research (e.g., Harrison, 1986; Zhang *et al.*, 2001).

Often an interplanetary shock wave was found to be followed several hours later by a transient solar wind stream with unusual plasma and magnetic field signatures, likely being the driver of the shock wave (Bothmer and Schwenn, 1996; Burlaga *et al.*, 1981). Systematic analyses of the wealth of satellite data obtained since the beginning of the space age has made it possible to establish reliable identification criteria of transient magnetized plasma flows as interplanetary consequences of CMEs (e.g., Gosling, 1990). To distinguish these CMEs in the solar wind from their solar counterparts, they are termed interplanetary coronal mass ejections or ICMEs (e.g. Cane and Richardson, 2003).

The classic plasma, magnetic field and suprathermal particle signatures of ICMEs at 1 AU are helium abundance enhancements, unusual ion and electron temperatures and ionization states (e.g., He^{+}, Fe^{16+}), higher than average magnetic field strengths (>10 nT), low variance of the magnetic field, smooth rotations of the magnetic field direction over time periods of several hours, bi-directional suprathermal (>40 eV)

Table 3.5. Basic characteristics of ICMEs at 1 AU.

Speed	300–>2000 km/s
Interplanetary shocks ahead of ICMEs	For CMEs with speeds >400 km/s
Magnetic field intensities	<10–>100 nT
Radial extension	0.25 AU ≈ 24 hours
Radial expansion with distance R from Sun	$\sim R^{+0.8}$ (R in AU)
Helical magnetic field structure	Magnetic cloud type ICMEs (1/3)
Plasma-β	<1 (especially in magnetic clouds)

From Bothmer (2006).

electron streaming, bi-directional suprathermal ion flows and plasma composition anomalies (e.g., Gosling, 1993 and references therein; Henke *et al.*, 1998, 2001). The detection of bi-directional electrons (BDEs) inside ICMEs suggests that the magnetic field lines may still be rooted in the Sun's photosphere at both ends (e.g., Bothmer *et al.*, 1996, 1997a; Gosling, 1993a). Table 3.5 summarizes the basic characteristics of ICMEs at 1 AU.

3.3.4 Examples of space storms driven by CMEs/ICMEs

Figure 3.32 shows measurements of the ICME that caused the major magnetic storm on July 15/16, 2000 (Bothmer, 2003; Lepping *et al.*, 2001). During this storm the Ap and Kp indices reached their maximum values. The plot in Figure 3.32 shows the time profile of the magnetic field magnitude B, the latitudinal angle θ ($+90^\circ$ corresponds to ecliptic north), the azimuthal angle φ (0° corresponds to the sunward direction, measured positive in the counterclockward direction), the plasma bulk velocity V, the proton density N_P and the thermal velocity of the protons V_{th}, as measured by the WIND spacecraft (courtesy D. Berdychevsky, from Lepping *et al.*, 2001). Data gaps were replaced by measurements from the GEOTAIL satellite (*http://www-spof.gsfc nasa.gov/istp/geotail/geotail.html*).

On July 15, 2000, the plasma parameters abruptly rose and the plasma speed increased to about 1100 km/s. This corresponds to the arrival of the interplanetary shock wave at 14:35 UT, labeled with a solid thick line in the figure. Several hours later on the same day at around 19:00 UT, it was followed by the ICME, as identified from the unusually high magnetic field strength and smooth southward to northward rotation of the magnetic field direction with respect to the ecliptic plane. The rotation started on July 15 at about 19:00 UT and lasted until July 16, 09:00 UT. The time period of the strongest magnetic disturbances measured at Earth corresponds with the time interval of the occurrences of strong southward magnetic field components caused by the ICME, even without taking details of the WIND orbit (i.e., the propagation time of the ICME from WIND to the magnetopause) into account. The magnetic storm starts with the arrival of the shock wave that triggers turbulent IMF fluctuations, followed by its main phase when the southward-directed magnetic field is encountered at the leading edge of the ICME. The magnetic field strength at the

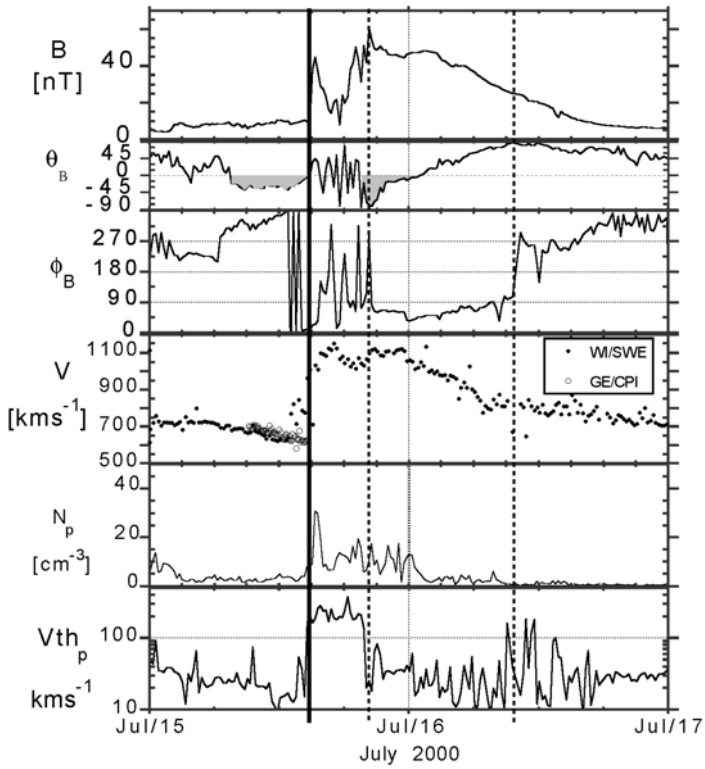

Figure 3.32. The ICME observed on July 15/16, 2000 by the WIND spacecraft. Data gaps are substituted with data from the Geotail satellite. The interplanetary shock ahead of the ICME is labeled by a solid line, dashed lines mark the boundaries of the ICME itself. Within the magnetic cloud type ICME, the magnetic field direction rotated from south to north, being directed eastward at its center. The ICME is of type SEN (i.e., it has left-handed magnetic helicity). Displayed solar wind parameters from top to bottom: magnetic field magnitude B, polar and azimuthal angles θ_B and φ_B, solar wind speed V, proton density N_P and thermal speed $V_{\rm th}$. Courtesy: Berdychevsky, from Lepping *et al.* (2001).

nose of an ICME is typically considerably enhanced (e.g., Bothmer and Schwenn, 1998) if the ICME is fast and the speed gradient, with respect to the ambient solar wind, is large so that the interplanetary shock can be driven by the ICME far out into the heliosphere, even to distances of many tens of AU or its outer boundaries (Richardson *et al.*, 2006). The ICME's leading edge undergoes strong compression effects due to its interaction with the ambient slower moving plasma ahead. From the solar wind speed and duration of the ICME derived from the WIND measurements, the radial size of the ICME is estimated as $\sim$0.3 AU. Although the spatial extent of the ICME is not known in the direction out of the ecliptic plane, it can be assumed from the large radial size that it is very large-scale in this direction too. Figure 3.33 sketches the propagation and deflections of the IMF by a fast ICME in the inner heliosphere, as viewed from a meridional perspective (Gosling, 1990). The deflections of the IMF in

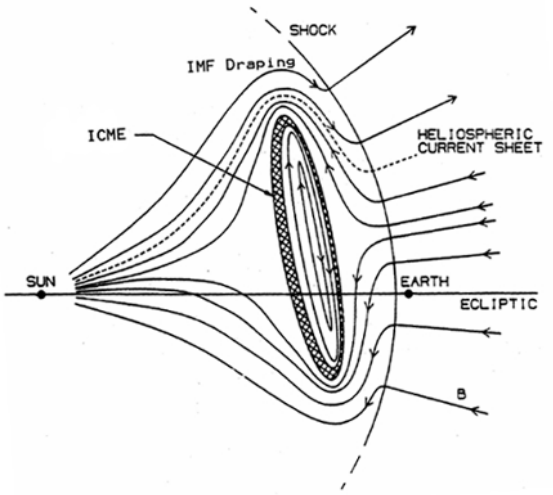

Figure 3.33. Idealized sketch of a fast ICME in the inner heliosphere viewed normal to the ecliptic plane. Note that – depending on the observer's position with respect to the center of the ICME and the Heliospheric Current Sheet (HCS) – different characteristic out-of-ecliptic variations of the IMF will be observed and that the shock and IMF deflections could also be observed even without hitting the ICME. The different signatures would lead to different signatures of geomagnetic storms or even not cause one. From Gosling (1990).

the region between the shock wave and the leading edge of the ICME, in which a high turbulent plasma regions forms, is termed 'draping of the IMF in the ICME sheath' (McComas *et al.*, 1988).

ICMEs that exhibit large-scale helical internal magnetic field configurations – like the one shown in Figure 3.32 – are termed magnetic clouds (Klein and Burlaga, 1982). In magnetic cloud type ICMEs the plasma-β is typically much smaller than 1, independent of the distance to the Sun in the inner heliosphere (Bothmer and Schwenn, 1998). According to Bothmer and Rust (1997) and Bothmer and Schwenn (1994, 1998), magnetic cloud type ICMEs can possess four different orientations of the magnetic field, as characterized by systematic rotations with respect to the ecliptic plane: SEN, SWN, NES, NWS, with N, S, E, W denoting the subsequent direction in which the magnetic field is directed at the leading edge of the ICME, its center and its trailing edge. These orientations characterize the helicity or chirality of a large-scale cylindrical magnetic flux tube in agreement with the self-consistent MHD model of a cylindrical magnetic flux tube shown in Figure 3.34 (Bothmer and Rust, 1997; Bothmer and Schwenn, 1998; Goldstein, 1983). If one points the fingers of the observer's hand towards the direction of the magnetic field in the leading edge of the ICME and the thumb along the magnetic field direction at the center of the ICME (the axis) and one further takes into account that the direction at the trailing edge is opposite to the direction at its leading edge, one can classify SEN- and NWS-type ICMEs as left-handed helical structures and SWN- and NES-type ICMEs as right-handed helical structures (Bothmer and Rust, 1997). According to this classification,

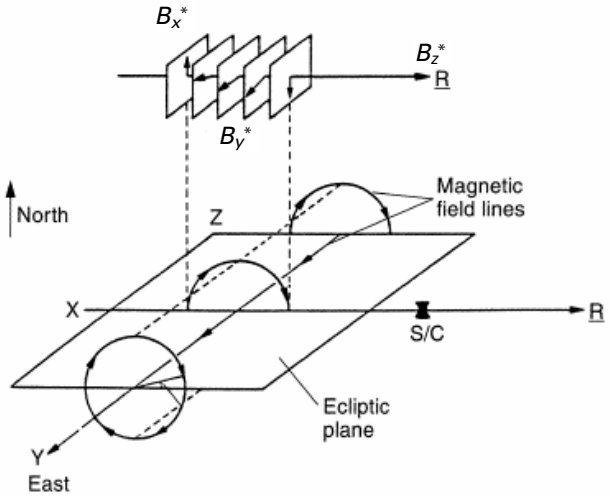

Figure 3.34. Idealized MHD model – a large-scale cylindrical flux tube – explaining the magnetic signatures observed during the passage of an ICME. From Bothmer and Schwenn (1998), after Goldstein (1983).

the ICME on July 15/16, 2000, is of type SEN – that is, it possesses left-handed magnetic chirality.

Magnetic cloud type ICMEs are of specific importance in the context of geomagnetic storms because their internal magnetic field structure can lead to large southward components of the IMF at 1 AU (e.g., Zhang and Burlaga, 1988). From a study of magnetic clouds in solar cycle 23, observed by the WIND and ACE satellites, Bothmer (2003) concluded that magnetic clouds trigger geomagnetic storms basically in two different ways or in combinations of these two ways: (1) through their specific internal magnetic field configuration, not only by SN or NS rotations, but also through the cloud's axis orientation when it is highly inclined and possessing a southward field direction (see also Mulligan *et al.*, 1998); and (2) through draping of the ambient IMF, especially in case of fast ICMEs driving shock waves ahead. The energy transfer from the solar wind to the magnetosphere is most efficient if ICMEs are associated with long-lasting (several hours) strong (<-10 nT) components of the magnetic field at 1 AU (e.g., Bothmer and Schwenn, 1995; Gonzalez and Tsurutani, 1987; Tsurutani, 2001) and activity is further amplified by ICMEs with high speeds (especially those >1000 km/s). It should be noted that in contrast – in case of northward IMF (i.e., $+B_z$-values associated with passage of an ICME) – a decrease in geomagnetic activity occurs (e.g., Veselovsky *et al.*, 2005).

ICMEs cause the highest V and lowest $-B_z$-values at Earth's orbit – the reason they are the drivers of all major geomagnetic storms with Kp $> 7+$ (Bothmer and Schwenn, 1995). Bothmer (2004) analyzed – in the framework of a European Union project (INTAS 99-727) – the causes of all geomagnetic storms with disturbed days with Ap values >20 nT during the years 1997–2001, based on an unprecedented coverage of solar wind measurements provided by near-Earth satellites. The results

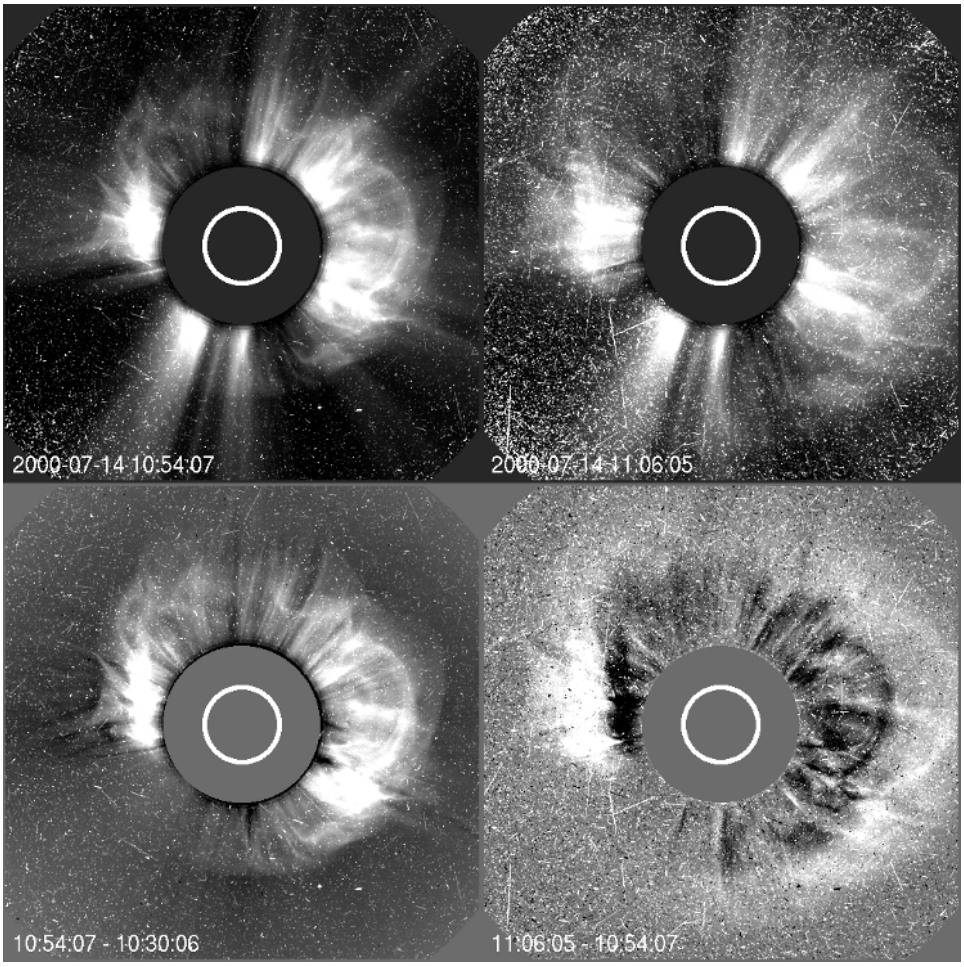

Figure 3.35. SoHO/LASCO C2 observations of the halo CME on July 14, 2000.

confirm that ICMEs are the prime drivers of major storms, as proposed by Bothmer and Schwenn (1996) in an earlier study of all storms with Kp values greater than 8−, and also that super-intense storms are often triggered by multiple interacting ICMEs.

Fast ICMEs driving shock waves from close to the Sun out into the heliosphere are also capable of accelerating charged particles to energies up to MeV or even GeV (e.g., Reames, 1999). Figures 3.35, 3.36 and 3.37 (color section) show the CME originating at the Sun on July 14, 2000, that caused the major geomagnetic storm on July 15/16, the EUV post-eruptive arcade that formed in this source region and a mosaic of solar observations including MeV electron and proton measurements from SoHO/COSTEP. COSTEP is the COmprehensive SupraThermal and Energetic Particle analyzer (e.g., Bothmer *et al.*, 1997b). The time delay at 1 AU to the CME onset time at the Sun is typically less than 15 minutes for the electrons and less than about 30

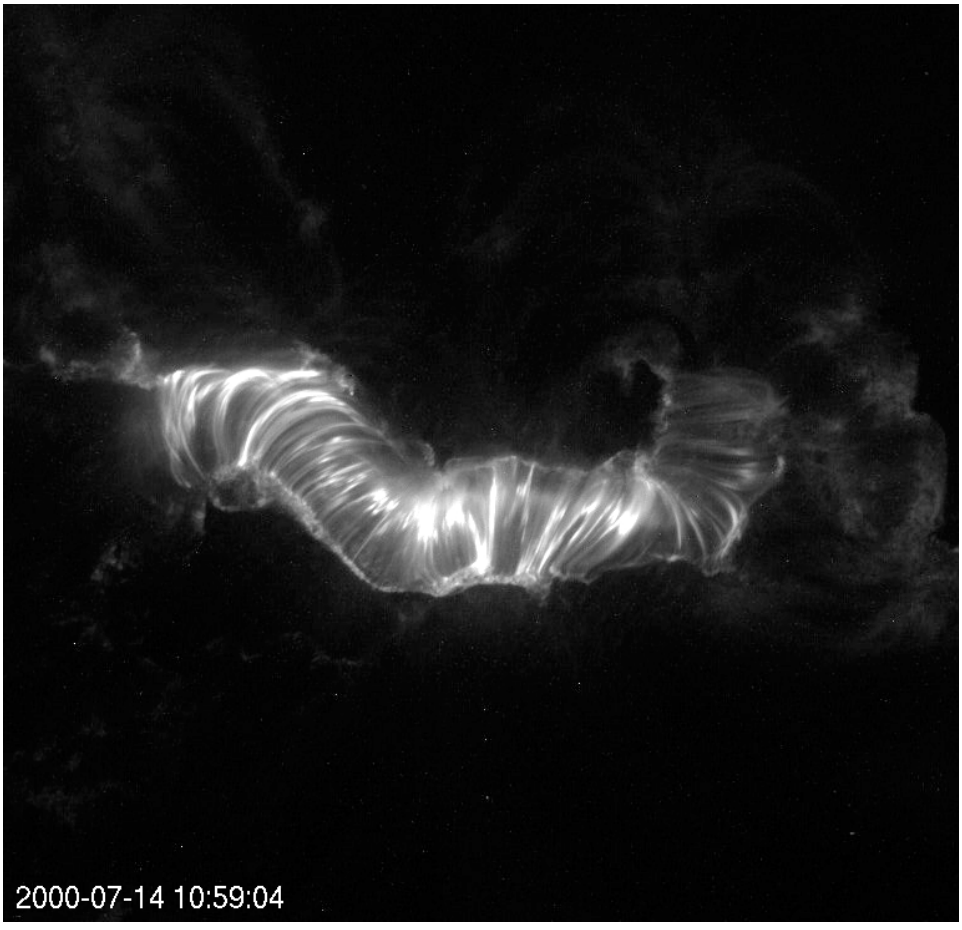

Figure 3.36. TRACE observations at 195 Å of the post-eruptive arcade in the CME's solar source region on July 14, 2000.

minutes for the protons at MeV energies for a prompt event. Protons of energies from 50–100 MeV from such solar energetic particle (SEP) events cause 'particle snowstorms' in the images from the SoHO optical telescopes when they pass through the CCDs, as can be seen in the LASCO/C2 and C3 images in Figure 3.37 (color section). They can degrade spacecraft hardware components, as can be seen in the plot of the efficiency of the SoHO solar panels in Figure 3.38 from their power decrease after the July 2000 event and after other major particle events (Brekke *et al.*, 2006). How high-energy protons affect electronic chips in the form of single-event upsets (SEUs) is schematically shown in Figure 3.39.

The largest geomagnetic storms in solar cycle 23, as measured by the peak Kp values (see also Table 3.8 in Section 3.5), were caused by two superfast (>2000 km/s, see *http://cdaw.gsfc.nasa.gov/CME_list/*) CMEs observed by SoHO/LASCO on

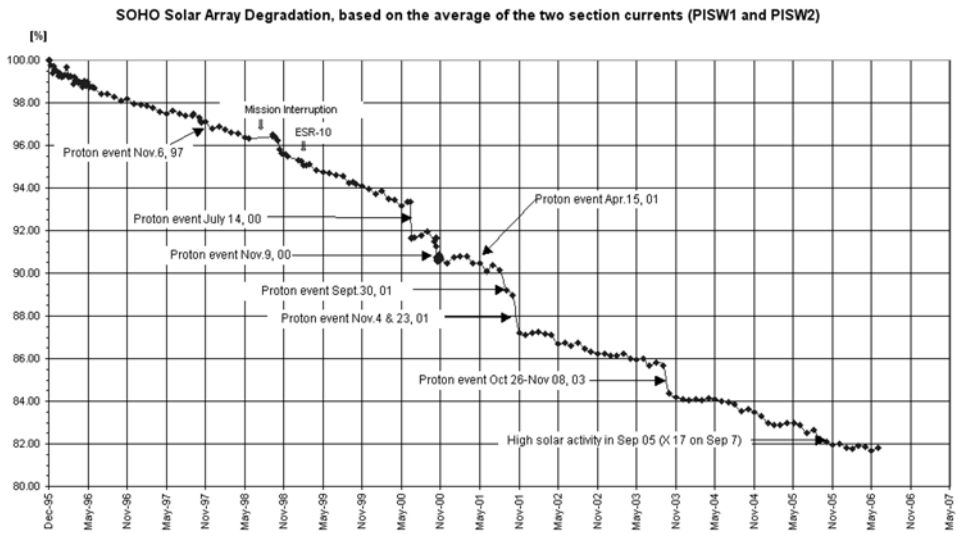

Figure 3.38. Effects of the July 14, 2000 solar energetic particle event and other major particle events on the solar panels of the SoHO spacecraft. Courtesy: Brekke *et al*. (2006).

October 28 and 29, 2003 (Figure 3.40, color section). It is worth pointing out that such high-speed CMEs are rare. Out of the more than 10,000 events listed in the SoHO/LASCO CME catalog for the years 1996–2006, only 36 had speeds in excess of 2000 km/s and just 25 of them reached speeds greater than 2500 km/s. Such superfast CMEs play a major role in terms of intense solar energetic particle events, as will be described in Section 3.3.5.

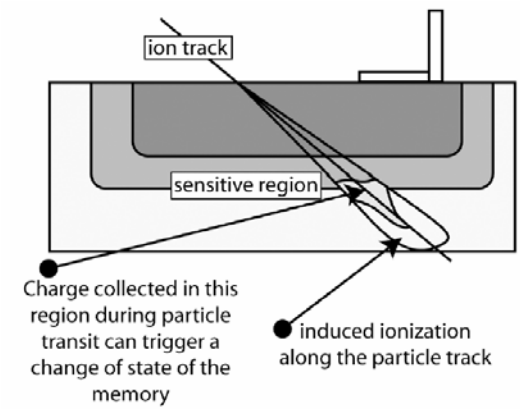

Figure 3.39. Example for ion interactions causing single-event upsets (SEUs). From Baker (2004), adapted from Robinson (1989).

3.3.5 Major SEP events, CME-driven shocks and radio-wave signatures

Intense solar energetic particle (SEP) events represent a serious threat to manned spaceflights to the Moon and Mars, during extravehicular activities on the International Space Station, and to air crews and passengers (see Chapters 5 and 11). Fortunately, commonly only a couple of times during a solar cycle do very intense SEP events with proton fluxes exceeding 10^{10} protons/cm^2 occur (ANSER, 1996), but unfortunately at the present time their origin is poorly understood and their forecast constitutes a big challenge to modern research.

We describe here two SEP events that occurred on October 28 and 29, 2003 and on January 20, 2005 (Figures 3.41a and 3.41b, color section), which were among the strongest in solar cycle 23. The close association between fluxes of energetic (at MeV energies) electrons and protons at 1 AU following CMEs at the Sun is well known (e.g., Bothmer *et al.*, 1997). It is now commonly assumed that MeV particles are primarily caused by shock acceleration mechanisms (e.g., Reames, 1999; Tylka, 2006) whereas particle acceleration in magnetic reconnection processes at the Sun seems to generate beams of particles at lower energies – as observed, for example, during the impulsive phase of a flare (see, e.g., Aschwanden *et al.*, 2006; Klassen *et al.*, 2000 and references therein). It is obvious that the key trigger exciting a strong shock wave in the coronal plasma and in the solar wind is the speed of the CME, as has been shown by Gopalswamy *et al.* (2005). High-speed CMEs ($> \sim$1500 km/s) play a crucial role in the acceleration of particles up to GeV energies, which can be registered as short-time cosmic ray intensity increases by neutron monitors on Earth (e.g., Gopalswamy *et al.*, 2005). Such ground level enhancements (GLEs) are caused by interaction of incoming ions with particles in the Earth's atmosphere.

Figure 3.41a shows the rapid increase in intensity of energetic protons on October 29, 2003 as measured by the GOES satellite in different energy channels. The enhanced particle flux lasted through the end of the day when a second particle event occurred. The time period of a decrease in particle intensity after 12:00 UT on October 29 was caused by the geospace transit of the ICME because its internal magnetic field structure is less transparent to energetic particles (see also Bothmer *et al.*, 1997). The two sudden proton flux increases can be associated with two superfast front-side halo (FH) CMEs labeled FH CME 1 and FH CME 2 in the second panel of Figure 3.41a, which represent height–time diagrams for the CME's leading edges tracked in the field of view of the LASCO C2 coronagraph during the displayed time period. Both CMEs were associated with strong X-ray flares measured by GOES (Figure 3.41a, third panel from top). Interplanetary magnetic field data from the ACE (Advanced Composition Explorer) satellite used to identify the subsequent ICME are shown in the bottom panel of Figure 3.41a.

Figure 3.41b provides the same measurements as described in Figure 3.41a, but for the SEP event on January 20, 2005. The intensity–time profile is more impulsive and shorter-lasting compared with the October 2003 events and the spectrum was much harder (Tylka, 2006). Particle energies reached GeV levels and the event was detected as GLE. In fact, in terms of GeV protons it was the largest GLE since 1956 (Tylka, 2006). According to a detailed analysis of the SoHO, ACE, SAMPEX, GOES

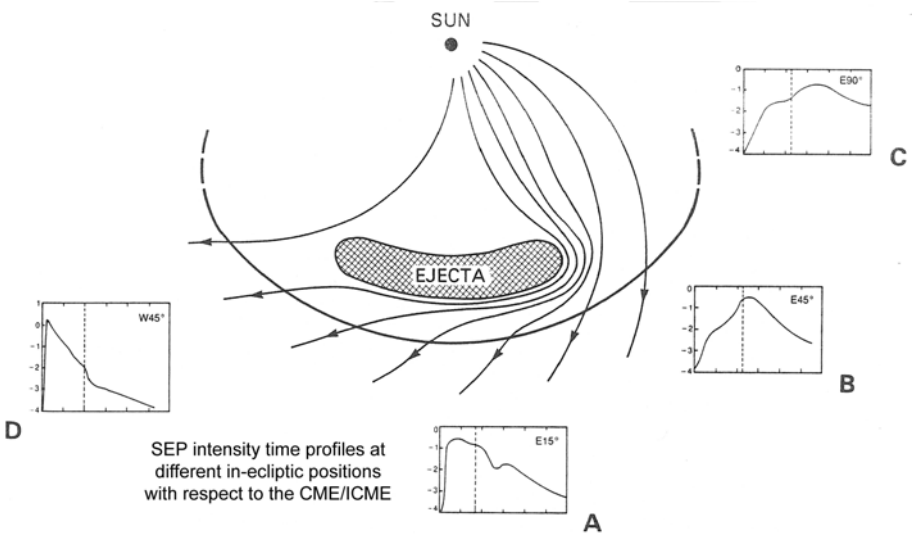

Figure 3.42. Intensity-time profiles measured in different solar energetic particle events with a different relative location with respect to the CME source region at the Sun. Adapted from Cane *et al.* (1988).

and RHESSI data and ground-based neutron monitor and radio-wave data, the superfast front-side halo CME had a speed exceeding 3000 km/s, such that it caused a strong shock wave with an Alfvénic Mach number of ~3, capable of accelerating the particles to GeV energies (Gopalswamy *et al.*, 2005; Tylka, 2006). The estimated distance from the Sun at which the protons were accelerated was estimated as 2.6 solar radii from the Sun's center, which interestingly corresponds to the coronal regime where the transition from open to closed magnetic field lines is expected. The composition of the energetic particles measured by ACE, SAMPEX and WIND supports the conclusion that the particles were accelerated out of the low corona and solar wind.

According to the results of Cane *et al.* (1988) the magnetic connection to the onset site of a CME and during its further interplanetary evolution can naturally explain the different intensity–time profiles observed by satellites in individual SEP events, as schematically shown in Figure 3.42. In agreement with the time–intensity profiles in October 2003 and January 2005, the sources of the October CMEs were situated near the solar disk center, whereas the January 2005 CME originated near the Sun's west limb (Figure 3.43). Due to the presence of higher energies of particles, the January 2005 SEP event was a far more serious threat to astronauts than the October 2003 SEP events (see also Chapter 11). It is well known that the SEP event in August 1972, which occurred between the Apollo 16 and 17 missions, would have been lethal to any astronauts on the Moon.

The largest solar proton events since the time they were systematically recorded are listed in Table 3.6. Note that the January 20, 2005 event is not included. The

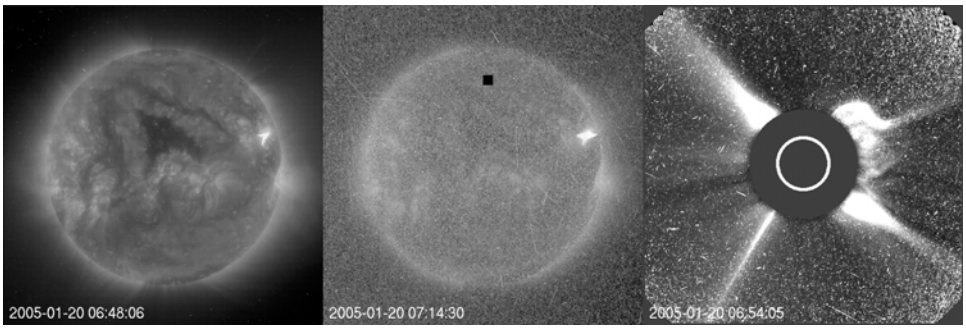

Figure 3.43. SoHO/EIT/LASCO observations of the CME, its source region and proton 'snowstorm' on January 20, 2005. The left image taken at 195 Å at 06:48 UT is a preflare image showing the bright active region to the northwest. The second EIT image shows the flaring region and image contamination by the proton snowstorm, followed by a LASCO/C2 image of the CME.

occurrence times of events listed in Table 3.6 show that, in principle, a SEP event can occur at any given time during a solar cycle – for example, the SEP events in 1994 and 2005 occurred not far from solar activity minimum. Another important aspect of Figure 3.42 is that the best magnetic connection is established with west-limb CMEs. This is the reason the solar source regions of CMEs that cause GLEs are predominately west-limb events (see Gopalswamy *et al.*, 2005). However, it must also be taken into account that, when considered more precisely, the magnetic connection at times of a solar event depends on the curvature of the Parker spiral at 1 AU at that time – that is, on the solar wind speed at 1 AU – so that the source region of the quasi steady-state solar wind is also important in terms of space weather forecasts. Since westward-directed CMEs do not necessarily expand to geospace, their occurrence does not necessarily imply the existence of a large southward B_z-component of the IMF near the Earth. Therefore, SEP events are often observed without the occurrence of geomagnetic storms. The speed at which energetic particles propagate to the Earth, often not much slower than the photons, can be seen in Figure 3.43 where the proton snowstorm is observed within minutes after the onset of the solar eruption. Tylka (2006) has shown that the particles were likely accelerated by the CME-driven shock at a distance of about 2.5 solar radii.

It is commonly assumed that it is in the upstream region of the shock wave driven by a fast CME in the low corona and interplanetary medium where the process of electron acceleration takes place. The accelerated electrons produce the radio emission near the electron plasma frequency as well as its second harmonic known as metric (at frequencies from some tens of MHz to several hundreds of MHz) and kilometric (at frequencies from several kHz up to about ten MHz) radio bursts (e.g., Klassen *et al.*, 2002). Though many questions remain to be answered about the origin and characteristics of, say, type II radio emissions – for example, the role of possible particle acceleration by blast waves initiated during the onset of flare/CME events – they can be considered as reliable indicators of shock-associated CMEs with speeds

Table 3.6. The 25 largest solar proton events measured in geospace between January 1976 and September 2005. Proton fluxes are integral 5-min averages for energies >10 MeV, given in particle flux units (p.f.u.), measured by GOES spacecraft at geosynchronous orbits (1 p.f.u. = 1 particle/(cm^2 s sr)). Different detectors, onboard various GOES spacecraft, have taken the data since 1976. More details are given at *http://umbra.nascom.nasa.gov/SEP/* The full list of proton events has been prepared by the U.S. Department of Commerce, NOAA, Space Environment Center, Boulder, CO.

Proton event			Associated flare and location of AR		
Start (day/UT)	Maximum	Proton flux (p.f.u. @ >10 MeV)	Flare max. (loc./day UT)	Importance (X-ray/opt.)	Location
1978					
Sep 23/10:35	Sep 24/04:00	2,200	Sep 23/10:23	X1/3B	N35W50
1982					
Jul 11/07:00	Jul 13/16:15	2,900	Jul 09/07:42	X9/3B	N17E73
1984					
Apr 25/13:30	Apr 26/14:20	2,500	Apr 25/00:05	X13/3B	S12E43
1989					
Mar 08/17:35	Mar 13/06:45	3,500	Mar 06/14:05	X15/3B	N35E69
Mar 17/18:55	Mar 18/09:20	2,000	Mar 17/17:44	X6/2B	N33W60
Aug 12/16:00	Aug 13/07:10	9,200	Aug 12/14:27	X2/2B	S16W37
Sep 29/12:05	Sep 30/02:10	4,500	Sep 29/11:33	X9/EPL	S26W90
Oct 19/13:05	Oct 20/16:00	40,000	Oct 19/12:58	X13/4B	S27E10
Nov 30/13:45	Dec 01/13:40	7,300	Nov 30/12:29	X2/3B	N26W59
1991					
Mar 23/08:20	Mar 24/03:50	43,000	Mar 22/22:47	X9/3B	S26E28
Jun 04/08:20	Jun 11/14:20	3,000	Jun 04/03:52	X12/3B	N30E70
Jul 07/04:55	Jul 08/16:45	2,300	Jul 07/02:23	X1/2B	N26E03
1992					
May 09/10:05	May 09/21:00	4,600	May 08/15:46	M7/4B	S26E08
Oct 30/19:20	Oct 31/07:10	2,700	Oct 39/18:16	X1/2B	S22W61
1994					
Feb 20/03:00	Feb 21/09:00	10,000	Feb 20/01:41	M4/3B	N09W02
2000					
Jul 14/10:45	Jul 15/12:30	24,000	Jul 14/10:24	X5/3B	N22W07
Nov 08/23:50	Nov 09/15:55	14,800	Nov 08/23:28	M7/mult.	N00-10W75-80
2001					
Sep 24/12:15	Sep 25/22:35	12,900	Sep 24/10:38	X2/2B	S16E23
Oct 01/11:45	Oct 02/08:10	2,360	Oct 01/05:15	M9	S22W91
Nov 04/17:05	Nov 06/02:15	31,700	Nov 04/16:20	X1/3B	N06W18
Nov 22/23:20	Nov 24/05:55	18,900	Nov 22/23:30	M9/2N	S15W34
2002					
Apr 21/02:25	Apr 21/23:20	2,520	Apr 21/01:51	X1/1F	S14W84
2003					
Oct 28/12:15	Oct 29/06:15	29,500	Oct 28/11:10	X17/4B	S16E08
2005					
Jan 16/02:10	Jan 17/17:50	5,040	Jan 15/23:02	X2	N15W05
May 14/05:25	May 15/02:40	3,140	May 13/16:57	M8/2B	N12E11

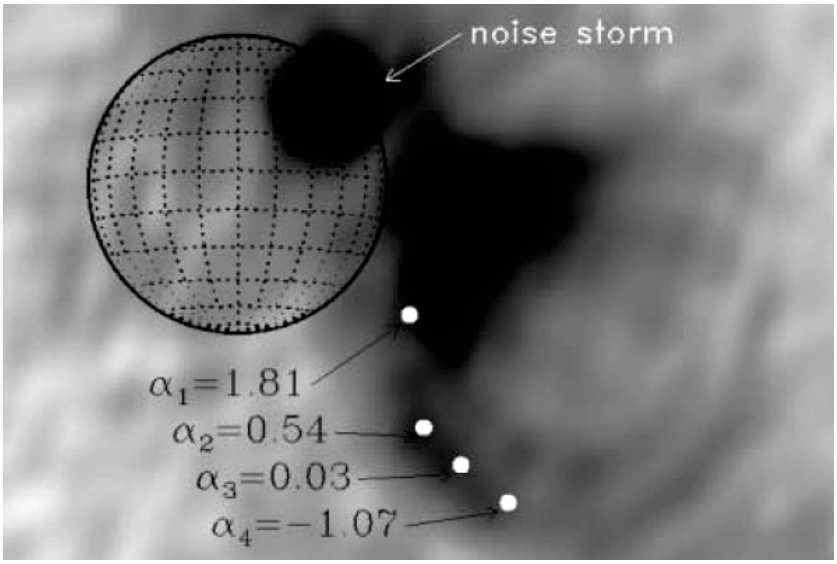

Figure 3.44. Snapshot map of the radio CME at a frequency of 164 MHz at the time of maximum flux (April 20, 1998 at 1013:23 UT, Nançay Radioheliograph). Background emission from the Sun has been subtracted. The radio CME is visible as a complex ensemble of loops extended out to the southwest. From Bastian *et al.* (2001).

$> \sim$500 km/s (Cane *et al.*, 1987). Bastian *et al.* (2001) have used radioheliograph measurements at a frequency of 164 MHz to image a CME at radio waves for the first time. The radio-emitting CME loops visible in Figure 3.44 are the result of nonthermal synchrotron emission from electrons with energies of $\sim$0.5–5 MeV interacting with magnetic fields of $\sim$0.1 to a few gauss. They appeared nearly simultaneously with the onset of a shock-associated type II radio burst, type III radio bursts and the initiation of a solar energetic particle event.

Figures 3.45 (color section) and 3.46 from Klassen *et al.* (2002) show the typical time history of optical, radio-wave and energetic particle measurements for a shock-associated west-limb CME. The MeV electrons measured at Earth's orbit by SoHO/COSTEP were released during or after, but never simultaneously with the onset of type II bursts and CMEs. The time delay between type II burst onset and electron event release ranged from 11.5 to 45 minutes. Thus, the electrons were released either at the end of shock-associated (SA) type II bursts or somewhat later. Most likely they were released when the associated type II burst and the CME reached a certain height, h, above the photosphere ($h \sim$ 1–4 R_S), such that the expanding CME and its shock wave reached magnetic field lines connected to the observer at Earth's orbit. During the subsequent evolution of the CME in the heliosphere, it drove a shock wave ahead of it as long as the speed gradient of the CME with respect to the ambient solar wind flow was sufficiently large. However, particle acceleration is most efficient close to the Sun since plasma density rapidly decreases with distance from the Sun and because the speed of the CME decreases due to its interaction with slower plasma ahead of it.

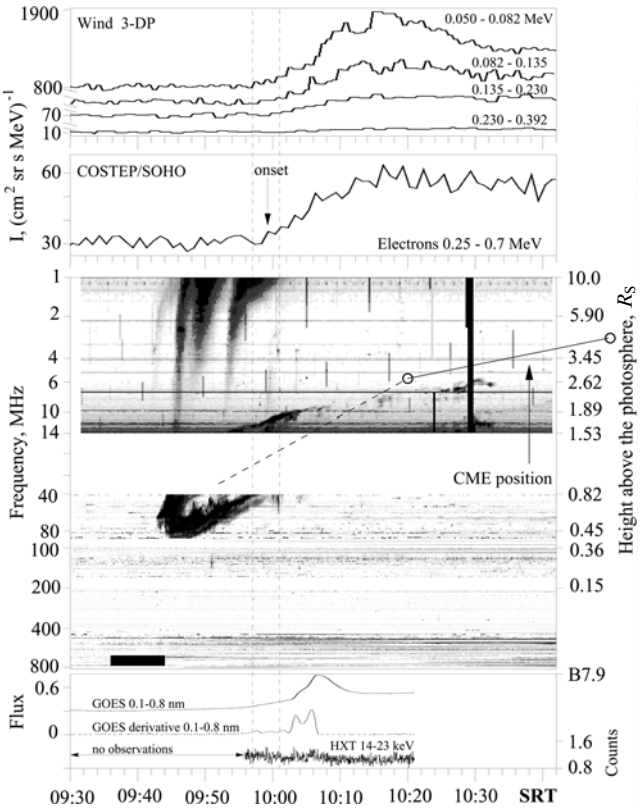

Figure 3.46. Relation between electron intensities in the range 0.050–0.7 MeV and electromagnetic emission at/close to the Sun for the event on May 18, 1998. The coronal type II burst, the CME and the electron event start after the filament eruption (see Figure 3.45). The energetic electrons in all channels were released simultaneously, 16.5 min after the type II and the SA (shock-accelerated) type III bursts onset. Top two panels: electron intensities observed by WIND 3-DP and SoHO/COSTEP instruments. The vertical dashed lines show the onset time interval of electrons detected in the range 0.050–0.392 MeV. The arrow indicates the onset time of electrons in the range 0.25–0.7 MeV. Middle panel: dynamic radio spectrum (800–1 MHz) overlaid with CME trajectory. A type II burst occurs between 86–6 MHz at 09:43–10:42 SRT. From the type II onset, the intense SA type III bursts escape from its lanes. At frequencies above those of type II no other type III, IV were observed. Open circles represent the CME heights (right scale), dashed line is backward extrapolation of the CME trajectory. Black bar denotes the time interval of the filament eruption. Bottom panel: soft X-ray flux (GOES: 1–8 Å, W m^{-2} 10^6), its time derivative (dotted, flux × 50) and hard X-rays measured by Yohkoh. The soft X-ray flare starts after the type II onset. The hard X-rays show – in agreement with the temporal behavior of the soft X-ray derivative – a weak enhancement at 10:03–10:07 SRT after the onset of the electron event. From Klassen *et al.* (2002).

Figure 3.47 (color section) shows the intensity–time profile for electrons and protons observed for the front-side halo CME on April 7, 1997. As expected, the particles measured at the highest energies by SoHO/COSTEP are detected first, with the ~5 MeV protons following the ~0.5 MeV electrons. In contrast to the sudden inten-

sity drop of the MeV particles, the peak intensities of the ~100 keV protons are observed in the upstream region of the interplanetary shock driven by the CME a couple of days later during its passage at 1 AU (Bothmer *et al.*, 1997, 1999). The 'leakage' of upstream shock-accelerated keV protons could be used to track the arrival of the halo CME/ICME similarly to the use of kilometric radio waves shown in Section 3.5. For further details on the different radio-wave signatures associated with solar eruptions the reader is referred to the summaries presented by Aschwanden (2004) and Schwenn (2006).

3.4 SPACE STORMS OVER THE SOLAR CYCLE – TIMES OF OCCURRENCE AND IMPORTANCE OF SOLAR, HELIOSPHERIC AND MAGNETOSPHERIC MODULATIONS

Although space weather forecasts are required on a daily basis, the dependence of the origin and characteristics of geomagnetic storms on the solar cycle phase yields important clues that can be added together to help establish realistic forecasts of space weather in the near future.

The variability of the solar photospheric magnetic field on various temporal and spatial scales shapes the global structure of the overlying corona and drives solar activity during the Sun's 11-year cycle. Input conditions that produce magnetic fluctuations measured at the Earth's surface can only be determined on the basis of satellite observations of the solar wind ahead of the Earth's magnetosphere. Since the beginning of the space age (end of the 1950s to the early 1960s), large databases were compiled which provided scientists with an invaluable resource to investigate the interplanetary causes of space storms and to study a unique set of correlated observations of the Sun, interplanetary space and geospace. Amongst the first systematic studies of the interplanetary causes of geomagnetic storms based on satellite data are those by Gosling (1993b). They analyzed the associations between Earth passage of interplanetary disturbances associated with CMEs and geomagnetic storms for major (Kp 8− to 9), large (Kp 7− to 7+), medium (Kp 6− to 6+) and small (Kp 5− to 5+) storms between August 1978 and October 1982. This was the period around solar activity maximum when the ISEE 3 satellite was operating directly upstream from the Earth. Gosling (1993b) found that all 14 of the major storms during the interval studied were associated with the passage of shock disturbances, and in 13 cases the ICME driving the shock was encountered as well. This reflects the fact that the shock itself does not commonly produce a long-lasting southward IMF component, rather this is primarily associated with the sheath region between the shock and ICME and with the internal magnetic field of the ICME itself. The level of geomagnetic activity stimulated by the shock/ICME in different storms was found to be directly related to the magnitude of the flow speed, magnetic field strength and southward field component associated with the event. These relationships reflect the fact that energy is transferred from the solar wind to the Earth's magnetosphere primarily by means of magnetic reconnection between the IMF and the terrestrial magnetic field at the dayside magnetopause (see Chapter 4). The rate of reconnection, and presumably also the rate at which energy is transferred to the magnetosphere, depends both on solar wind flow speed and the magnetic field strength and orientation. The association

of geomagnetic activity with shocks and ICMEs becomes less and less pronounced at lower levels of geomagnetic activity – that is, for medium and small storms.

The solar and interplanetary causes of the five largest geomagnetic storms between 1971 and 1986 were analyzed by Tsurutani *et al.* (1992). Analyzing the satellite data of the solar wind, they found that these five storms were caused by transient fast solar wind flows that were driving shock waves ahead of them. The solar sources could not be investigated in depth, but intense solar flares indicative of strong solar eruptions (fast CMEs) were associated with all events. The key ingredient that was found in the solar wind data was the long-lasting (several hours) extreme magnitude of the southward-directed IMF (which is usually of the order of 5 nT at 1 AU in regular solar wind flows). The enhanced IMF variability was more pronounced than solar wind variability. The southward IMF component at 1 AU that triggered the geomagnetic storms was caused either by draping of the IMF in the sheath region between the shock and subsequent ICME (see Section 3.3.4) and/or by the strong southward internal magnetic field of the ICME itself. The intensity of the geomagnetic storms was amplified in cases when the ICME-driven shocks ram solar wind flows with small pre-existing southward fields and compress those fields.

These two studies – which yielded results for a few major storms around solar activity maximum – were followed by an extended study by Bothmer and Schwenn (1995) who analyzed the interplanetary causes of all major (Kp $\geq 8-$) geomagnetic storms during the years 1966–1990 (when satellite solar wind data without major gaps were taken). The results of this study showed that 41 of the 43 analyzed storms during that time interval were found to be caused by shock-associated ICMEs, one storm was caused by a slow-moving ICME of the magnetic cloud type followed by a CIR and only one by a CIR itself. Thus, independently of the solar cycle phase, major geomagnetic storms are driven by fast (shock-associated) ICMEs. A similar result was obtained using the Dst index as an indicator of geomagnetic storm occurrence. The maximum values of Kp in the individual events were directly related to the peak southward components of the IMF. Draping of the IMF near the front part of ICMEs and/or the magnetic field configuration of the magnetic cloud type (in the ICME itself) were the sources of the extreme negative B_z values. The intensity of the IMF southward component was often substantially amplified at the front and rear parts of magnetic clouds due to their interaction with the ambient solar wind. This was found to be of particular importance for cases when a magnetic cloud type ICME was followed by a CIR or by an interplanetary shock, especially during those very disturbed interplanetary conditions produced by a sequence of ICMEs (through multiple ICMEs or MICMEs). The prime reason CIRs commonly do not trigger major geomagnetic storms is that they are associated with minor magnetic field strengths of shorter duration at 1 AU.

Different contributions of ICMEs and CIRs have been investigated in detail for the years 1972–2000 by Richardson *et al.* (2002). Their results support the previous findings: the most intense storms are nearly solely caused by ICMEs, as shown in Figure 3.48. The authors used almost the same classification as Gosling *et al.* (1993b). The different occurrence rates (storms/year) of small, medium, large and major geomagnetic storms in 1972–2000 caused by ICMEs and co-rotating streams are

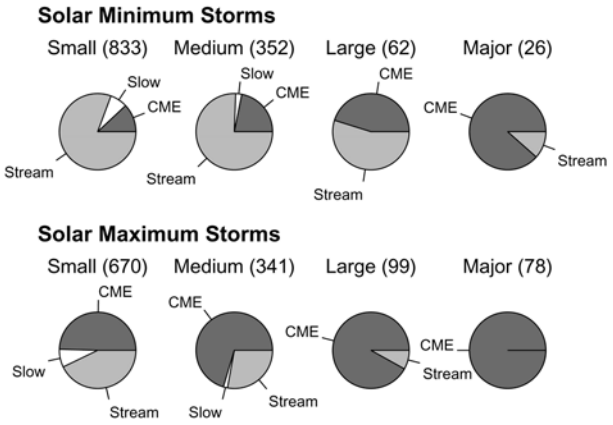

Figure 3.48. Frequency distribution for small, medium, large and major geomagnetic storms as classified by the Kp index, during the years 1972–2000 at different phases of the solar cycle as inferred from analysis of solar wind data. From Richardson *et al.* (2001).

shown in Figure 3.49. ICME-associated storms clearly dominate around times of solar activity maximum and most large and major storms are caused by them. Storms related to co-rotating streams and CIRs are dominant at medium to small storm intensity levels, especially in the declining phase of the solar cycle. Interestingly, the frequency distribution of intense storms over the solar cycle shows a two-peak frequency distribution (as also reported by Gonzalez and Tsurutani, 1990), with peaks before and after the sunspot number maximum, as can be seen in Figure 3.49. The short decrease at times of solar activity maximum might be related to the latitudinal variation in CME source region position (Figure 3.50, Gopalswamy *et al.*, 2003) and to its free expansion to higher latitudes in the absence of polar coronal holes that can systematically deflect CMEs to lower latitudes (see Figure 3.51, Cremades and Bothmer, 2004; Cremades, Bothmer and Tripathi, 2006).

If one ignores the strength of intensity and only takes into account the number of geomagnetically disturbed days (e.g., with Ap $\geq$40), then the picture of enhanced geomagnetic activity in the declining phase of the solar cycle becomes very pronounced, as can be seen in Figure 3.52. These weaker storms are caused by CIRs followed by high-speed streams from coronal holes, as described in Section 3.2.3.

Arguably, the most detailed study of geomagnetic storms based on the unprecedented set of interplanetary measurements from the IMP, WIND and ACE satellites was that undertaken within the EU–ESA/INTAS projects 99-727 and 03-51-6206: the solar and interplanetary sources of all geomagnetic storms in solar cycle 23 with intensity levels of Ap >20 were analyzed. The project website (*http://dbserv.sinp.msu.ru/apev*) includes a catalog of all identified space storms including solar and interplanetary data, which serves as an invaluable tool for space weather researchers. The results of these projects are shown in Table 3.7 and Figure 3.53, which summarize the sources identified from analysis of the interplanetary data for all storms with intensity levels of Ap >20 in 1996–2001 (Bothmer, 2004). Note that there were no such storms observed in 1996, so Table 3.7 and Figure 3.53 start to list events recorded since

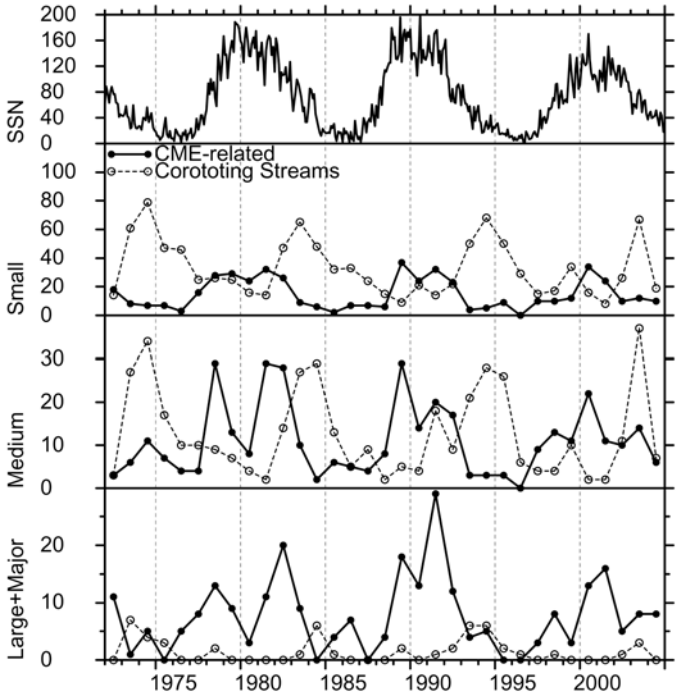

Figure 3.49. Occurrence rates (storms/year) of small, medium, large and major geomagnetic storms in 1972–2005 associated with ICMEs and co-rotating streams displayed together with the sunspot number. From Richardson (2006).

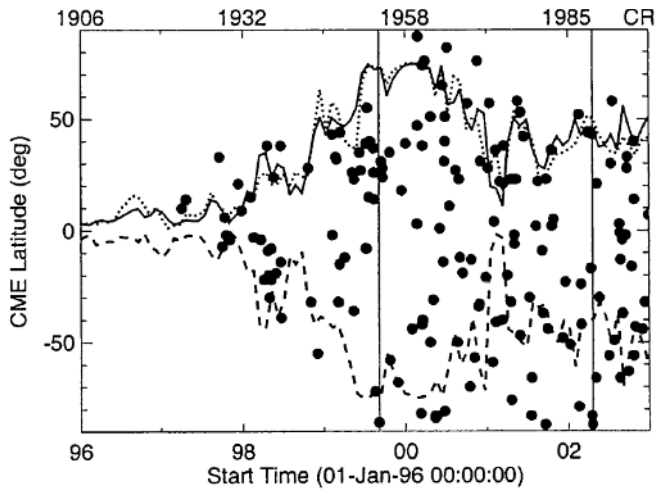

Figure 3.50. Latitudes of prominence eruption-associated CMEs (filled circles) in the northern (dotted line) and southern (dashed line) hemisphere. The solid lines represents an average value. The vertical lines denote the time interval of the observations of high-latitude CMEs. From Gopalswamy *et al*. (2003).

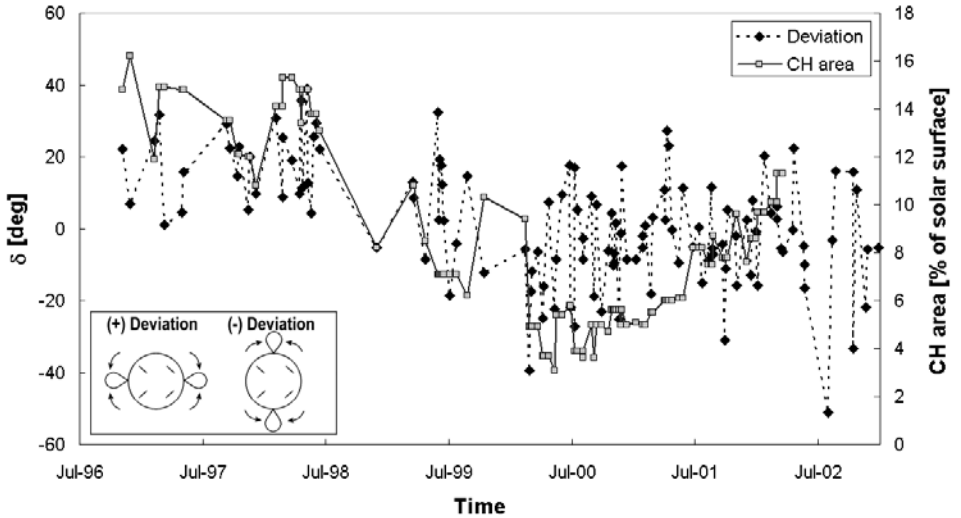

Figure 3.51. Comparison of the deflection angles δ measured for the CMEs' centers with respect to their low coronal source regions with the spatial area of the polar coronal holes at the Sun in 1996–2002. A positive angle corresponds to a deflection towards the ecliptic plane. Note that around times of the Sun's magnetic polarity reversal in 2000, the polar coronal holes have vanished, and that during that time the CME deflection reflects an unsystematic pattern. From Cremades and Bothmer (2004).

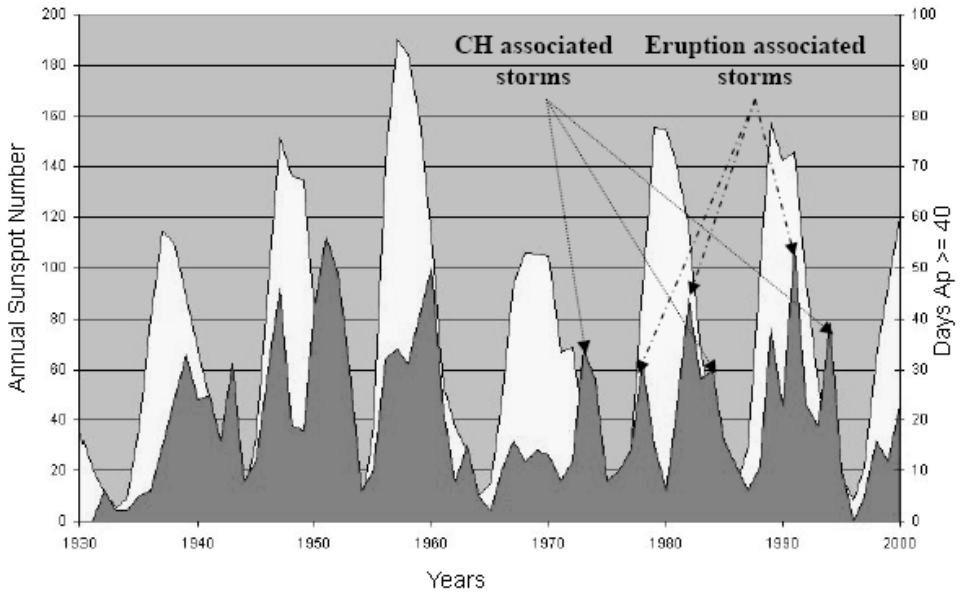

Figure 3.52. Solar cycle variation of the number of geomagnetically disturbed days with Ap $\geq$40. The sunspot number curve is shown in white. The few time intervals that were dominated by different solar drivers of the storms are indicated. Ap diagram adapted from J. Allen, *http://www.ngdc.noaa.gov/stp/GEOMAG/image/APStar_2000sm.gif*

Table 3.7. Causes of geomagnetic storms with Ap >20 during 1996–2001.

Cause of storm	Number of days with Ap >20 during 1997–2001	Number of individual storms	Typical Ap range
Slow solar wind	8	8	<30
CIR/CH	90	55	<60
Combined ICME/CIR	18	11	<150
ICME	101	81	<170
MICMEs	38	30	<200
Total number	*255*	*185*	

Acronyms: co-rotating interaction region (CIR); coronal hole (CH); interplanetary coronal mass ejection (ICME); multiple ICMEs (MICMEs). From Bothmer (2004).

1997. According to this study, the solar wind drivers of geomagnetic storms with intensity levels of Ap >20 can be classified in five different categories as follows:

1. Slow solar wind near the heliospheric current sheet associated with low levels of geomagnetic activity (storm intensity commonly Ap <30).
2. Co-rotating interaction regions (CIRs) followed by coronal hole (CH) high-speed (500–750 km/s) plasma flows (storm intensity commonly Ap <60).
3. Interplanetary counterparts of CMEs (ICMEs) interacting with CIRs (storm intensity commonly Ap <150).
4. Southward IMF components caused by the IMF draping ahead of ICMEs or through their internal magnetic field configuration, or both (storm intensity commonly Ap <170).
5. Multiple ICMEs (storm intensity commonly Ap <200).

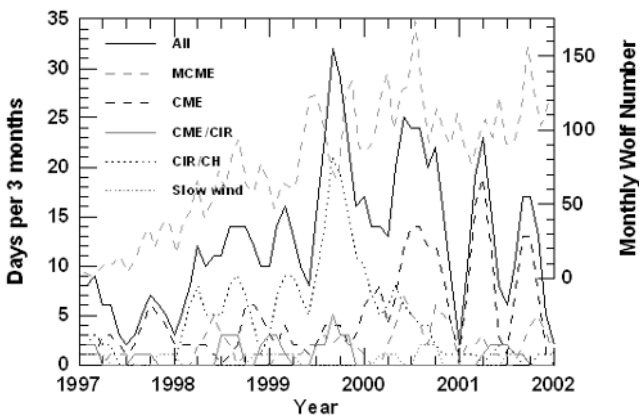

Figure 3.53. Frequency distribution of the different solar/interplanetary drivers of geomagnetic storms with Ap >20 in 1997–2001 compared with the sunspot number as an indicator for the phase of the solar activity cycle. From Bothmer (2004).

Most disturbed days during the investigated period occurred in 1999, 2000 and 2001. Whereas in mid-1999 many storms (although of lower intensity) were still caused by CHs, this picture dramatically changed in 2000 when geomagnetic activity drivers started to become completely ICME-dominated. It is well known that CHs and associated CIRs play major roles as triggers of geomagnetic storms in the decreasing phase of solar activity, but their role in the rising phase of the cycle seems so far to have been underestimated.

Besides the characteristics of photospheric and coronal source regions of quasi steady-state solar wind flows and transient streams due to solar eruptions (CMEs), stream interactions taking place in the heliosphere during the evolution of individual flows up to 1 AU can lead to amplification or weakening of geo-effectiveness in individual events – as described for the formation of CIRs in Section 3.2.3. CIRs can also amplify the geo-effectiveness of ICMEs, as is shown in the example in Figure 3.54 in which an ICME of the magnetic cloud type has been compressed in its trailing

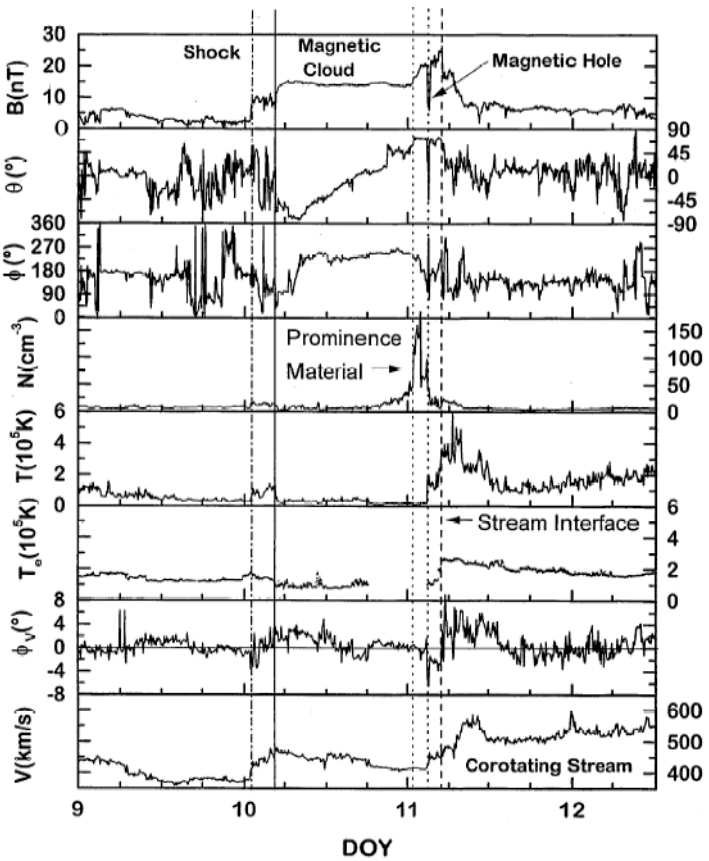

Figure 3.54. Solar wind and magnetic field parameters from January 9 to 12, 1997 showing a magnetic cloud type ICME that was overtaken by a co-rotating stream from a coronal hole. From Burlaga *et al.* (1997).

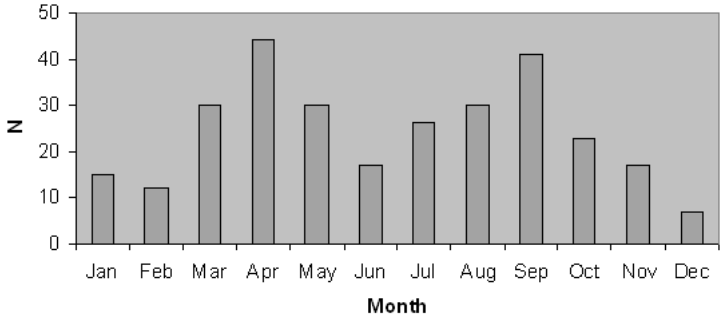

Figure 3.55. Monthly occurrence rates of geomagnetic storms with intensity levels of Kp $\geq 8-$ in 1932–2006.

part by a co-rotating high-speed solar wind stream from a coronal hole overtaking the ICME, as observed by the WIND satellite (Burlaga *et al.*, 1998). It is interesting to note that the January 1997 ICME event produced only a moderate geomagnetic storm, but it has become a very famous space weather event in the media because of its association with the malfunction of an AT&T telecommunication satellite (*http://www-istp.gsfc.nasa.gov/istp/cloud_jan97/*). The stream interaction led to compression of the ICME's trailing part, so in the case of a longer interval of the southward field, substantial amplification of the geo-effectiveness of the ICME would have been caused. In this way, multiple transient solar wind streams can cause quite complicated flow structures in the heliosphere (Burlaga *et al.*, 1987).

Beyond the solar and heliospheric modification of solar wind input conditions, the structure of the Earth's magnetosphere also plays a key role in modulating geo-effectiveness. The occurrence rate of intense geomagnetic storms shows a pronounced semiannual variation, as shown in Figure 3.55 where the monthly frequencies of geomagnetic storms with levels of Kp $\geq 8-$ are plotted for the years 1932–2006. Most intense storms occur at times near the equinoctial months of March and September, with a clear depression in the number of storms during the solstitial months in June and December. The seasonal variation of geomagnetic activity has been known for a long time (e.g., Bartels, 1963; Gonzalez *et al.*, 1993) and various mechanisms have been proposed in controversy. Historically, the first was the so-called axial mechanism (e.g., Cortie, 1913, 1916; Priester and Cattani, 1962) which was based on the fact that the Earth reaches its maximum heliographic latitude of $+7.2^\circ$ and -7.2° on approximately September 6 and March 5, respectively. The idea was that low-latitude active regions cause solar eruptions that are more likely to reach the Earth. However, today we know that CMEs originating from latitudes around 40° in both solar hemispheres do pass geospace (e.g., Bothmer and Rust, 1997; Bothmer and Schwenn, 1998), so that latitudinal variation does not seem to play the key role in the origin of semiannual variation.

Another early proposed concept to explain the seasonal variation of intense geomagnetic storms was based on variation in the effectiveness of the interaction between the solar wind and the Earth's magnetosphere that depends on the orienta-

tion of the Earth's magnetic dipole relative to the Sun–Earth line. In this theory, known as the equinoctial mechanism, storms would be expected to be favorably observed to occur near March 21 and September 23. Another theory, the Russell–McPherron model, takes into account the inclination of the solar magnetic equator with respect to the ecliptic plane, leading to the largest southward components of the IMF (assuming a nominal Parker spiral configuration) in the GSM coordinate system around April 5 and October 5 (Russell and McPherron, 1973b). In this model geomagnetic activity is higher for solar wind streams possessing a negative IMF polarity (i.e., the field is directed towards the Sun) in spring and a positive IMF polarity (i.e., the field is directed away from the Sun) in fall (e.g., Crooker and Siscoe, 1986). It should be noted that, ideally, this holds for streams having the same solar wind speed and that in the case of different speeds the Russell–McPherron effect can be wiped out.

Due to the proximity predicted by the different models for the dates of expected maximum geomagnetic activity and also to the intrinsic variation in the seasonal pattern from year to year, it has been a challenging task to determine the individual contributions of different mechanisms to semiannual variation. As has been shown by Gonzalez *et al.* (1993), the seasonal phase of maximum activity varies with the level of geomagnetic activity. This fact supports the assumption that different solar wind conditions have different intrinsic properties (CIRs, fast solar wind streams, ICMEs) and stimulate geomagnetic activity differently (e.g., Huttunen *et al.*, 2002). Of course, Alfvénic fluctuations causing southward IMF components within high-speed streams, amplified or weakened through the Russell–McPherron effect, do not impose large pressure pulses on the Earth's magnetosphere as in the case of CIRs or fast ICMEs. Extremely fast ICMEs can even compress the day-side magnetopause to a distance as close as about 6 R_E such that geostationary satellites unexpectedly stay for some period of time in the solar wind upstream of the Earth's magnetosphere, as was the case in the March 1989 geomagnetic storm.

It is worth noting that the Kp and Dst indices react differently to solar wind dynamic pressure (e.g., Huttunen *et al.*, 2005, see Section 3.2.2). A scenario that can possibly explain the pronounced semiannual variation of intense geomagnetic storms has been proposed by Crooker *et al.* (1992). The authors provide convincing evidence that intense southward IMFs responsible for great storms can reside in the post-shock plasma preceding fast ICMEs and maybe as well in the internal fields of ICMEs themselves. According to this model, post-shock southward field geo-efficiency results from a major increase in the Russell–McPherron effect through a systematic pattern of compression and draping within the ecliptic plane (see Figure 3.42). Differential compression from the shock increases the Parker spiral angle and, consequently, the azimuthal IMF component that projects as the southward IMF component onto Earth's dipole axis. Southward fields in post-shock flows ahead of ICMEs become strongest at the spring (fall) equinox in ICMEs emerging from toward (away) sectors. We note here that, more precisely, the prime role belongs to the IMF polarity the ICME-driven shock runs into, rather than to the IMF polarity the ICME originated from. ICME source region polarities determine the internal magnetic field configuration of magnetic clouds (Bothmer and Rust, 1997; Bothmer and Schwenn, 1998). The efficiency of the Russell–McPherron effect for post-shock flows is supported by the

results of Phillips *et al.* (1992). They have shown that geo-effectiveness associated with shocks and ICMEs is ordered by plasma bulk speed, southward field and pre-existing conditions. When such events are ordered by pre-event GSEQ (geocentric solar equatorial) components, the seasonal effect is clear, with the Dst index being largest near the equinox. Contrarily, no such trend was found for slower ICMEs that are not associated with shocks. Besides the semiannual variation obvious from Figure 3.55, it appears that seasonal variation with slightly enhanced geomagnetic activity in July to September is statistically present. A possible explanation for this seasonal variation could be the uneven hemispheric distribution of the stations from which Kp is derived – 11 of the current total number of 13 Kp stations are located in the northern hemisphere.

Although solar wind input conditions are modulated and intense storms favor the equinox months, an intense storm (Kp $\geq 8-$) can in principle occur at any given time of the year and at any phase of the solar cycle (see also Tsurutani *et al.*, 2003). This can be seen from the storm occurrence times of the 25 largest geomagnetic storms (in terms of their peak Kp index) in 1932–2006 listed in Table 3.8. Intense storms occurred in January 1960 and 1949 or in July 1959 and 1946 – that is, not during the equinoctial months favored by seasonal variation. Moreover, sometimes intense storms even occur not far from solar activity minima, as in February 1986 or November 2004. The intensity of an individual geomagnetic storm is in principle independent of the phase and strength of a solar cycle. These findings yield the natural conclusion that space weather forecasting has to be performed on a daily basis, with fundamental solar and heliospheric observations and modeling required, as will be described in the final section of this chapter.

3.5 SOLAR OBSERVATIONS AND MODELING FOR SPACE WEATHER FORECASTS

Since the advent of the space age new scientific observations other than from the Earth's surface have provided us with a new view on the physics of the Sun, its dynamic atmosphere and effects on interplanetary space, including geospace. Besides solar EM radiation, the Sun permanently emits magnetized plasma, either in a quasi steady-state form of slow and fast solar wind streams, or, occasionally, in an explosive manner in the form of coronal mass ejections (CMEs) that evolve in the interplanetary medium as ICMEs (interplanetary coronal mass ejections). Solar wind streams of any type may interact with each other, and compression effects may significantly amplify preexisting southward components of the IMF which are favorable for triggering geomagnetic storms.

To know at any given moment of time the energy state of the interplanetary medium, especially that of the Earth's magnetosphere, which is permanently impacted by the solar wind, it is of crucial importance to provide reliable forecasts of solar wind conditions for a few day in advance. This task requires continuous monitoring of the evolution of solar photospheric magnetic flux as the ultimate driver of the variety of known solar activity phenomena and continuous – if possible in high time resolution –

Table 3.8. The largest 25 geomagnetic storms between January 1932 and July 2006. The last column provides the total sum of all ap-values greater than or equal to 179 (equivalent to Kp $\geq$8−).

Year	Days	Month	Total sum of 3-hour intervals with ap $\geq$179
1989	13, 14	3	2824
1941	18, 19	9	2736
1960	12, 13	11	2529
1940	29, 30, 31	3	2459
1960	6, 7	10	2451
1960	31, 1	1	2444
1940	24, 25	3	2429
1946	22, 23	9	1944
1986	7, 8, 9	2	1923
1991	24, 25, 26	3	1879
1959	15	7	1807
2003	29, 30	10	1765
1957	4, 5	9	1615
1946	28	3	1579
1946	26, 27	7	1507
1967	25, 26	5	1515
1982	13, 14	7	1515
1941	5	7	1479
2004	9, 10	11	1451
1949	25, 26	1	1422
1958	8	7	1415
1941	1	3	1414
2000	15, 16	7	1386
1958	11	2	1379
1959	17, 18	7	1365

imaging of the corona, preferentially at white-light and EUV wavelengths. These observations can than be used to model the solar wind outflow to predict the expected flow structures and solar wind conditions at Earth's orbit. These conditions are also of prime importance to discover into which global stream structure a suddenly released CME evolves and to provide information into which magnetic background the energetic charged particles that may have been accelerated in association with solar flares and CMEs will propagate.

3.5.1 Modeling the quasi steady-state corona and solar wind

Modeling of the quasi steady-state corona and solar wind may in its easiest way be established based on the so-called potential field source surface (PFSS) model in which the coronal magnetic field is assumed to be current-free ($\mathbf{V} \times \mathbf{B} = 0$) (e.g., Hoeksema,

1984; Schrijver and de Rosa, 2003; Wang and Sheeley, 1992). The data input for these models are ground- and space-based magnetograms. New magnetohydrodynamic (MHD) codes are able to take – to some extent – contributions from solar active regions into account (Aschwanden *et al.*, 2006). The structure of the global solar corona has been calculated – for example, based on the Magnetohydrodynamics Around a Sphere (MAS) model developed by the SAIC (Science International Corporation) group – for the range 1–30 R_S based on the strength of the radial magnetic field $B_r(\theta, \varphi)$ as a function of solar latitude (θ) and longitude (φ) provided through full disk synoptic (the data cover the time period of a full solar rotation) magnetograms and coronal temperature $T_e(\theta, \varphi)$ and density $n_e(\theta, \varphi)$ values. Modeling of the solar corona and its changing structure is shown in Figures 3.56 and 3.57 (both in color section) (from Balogh and Bothmer *et al.*, 1999; modeling by Linker *et al.*, 1999, and Mikic *et al.*, 1999). This model has been used successfully to estimate solar wind speeds at the orbit of the Ulysses spacecraft during the Whole Sun Month Campaign in 1996, as shown in Figure 3.56.

Wang *et al.* (1997) modeled the solar wind expansion in the heliosphere by taking into account the locations, areal sizes, rotation and solar cycle evolution of coronal holes. Solar wind flows from the coronal holes can then be reproduced by applying extrapolation techniques to measurements of the photospheric magnetic field and its expansion to estimate the bulk speed, mass and energy densities of solar wind plasma in the heliosphere. Odstrcil *et al.* (2002, 2003) developed a time-dependent solar wind model, the so-called ENLIL code, for the range 21.5 R_S to 1.6 AU for a heliographic latitude range of $\sim 60^\circ$ in the inner heliosphere. The model is also based on solar magnetograms and, in addition, uses the MAS or WSA (Wang–Sheeley–Arge) code to locate inner radial boundary conditions. A detailed summary on the current modeling efforts was given by Aschwanden *et al.* (2006). It should be noted that, unfortunately, the magnetograms currently obtained are not providing precise values of the photospheric magnetic field at heliographic latitudes beyond about 60° and commonly just provide measurements of the longitudinal component of the magnetic field along the line of sight. Figure 3.58 (color section) shows how the method by Wang *et al.* was applied by the U.S. NOAA National Space Environment Laboratory, Boulder, CO, to forecast solar wind speed and IMF polarity at Earth's orbit and to compare the predictions with *in situ* data from the ACE satellite (*http://www.sec.noaa.gov/ws/*). Predicted quasi-stationary solar wind input conditions can then be used to forecast expected geomagnetic activity – similar to the methods used in Figure 3.59 (color section) where solar wind parameters were used to model the expected impact of an ICME on November 20–21, 2003 – in terms of the Dst index according to the models by O'Brien and McPherron (2000) and Wang *et al.* (2003). This event was one of the strongest storms in solar cycle 23, as identified in the Dst index (Huttunen *et al.*, 2005). The O'Brien and McPherron model assumes that the ring current injection and ring current decay parameter are controlled by the solar wind electric field. The Wang *et al.* (2003) model includes the influence of solar wind dynamic pressure in the injection function and the decay parameter. Recently, Mikic and Linker (*http://shadow.adnc.net/corona/mar06eclipse/mar06eclipse.html*) successfully modeled the global structure of the solar corona a week ahead of the solar eclipse on March 29, 2006.

3.5.2 Forecasting coronal mass ejections and solar energetic particle events

Since fast coronal mass ejections (CMEs) cause the most intense space storms and solar energetic particle (SEP) events (see Sections 3.3.4 and 3.5), it is currently the most challenging task to predict the onset and interplanetary consequences of these CMEs. In terms of space storms one is especially interested in the prediction of superfast (2000–3000 km/s) front-side halo CMEs (SFHCMEs). As was shown by Cremades and Bothmer (2004) and Tripathi, Bothmer and Cremades (2004), commonly CMEs originate from localized bipolar regions in the photosphere separating opposite polarity magnetic fields (see Section 3.3.2). Photospheric bipolar regions appear in various spatial sizes and in a variety of intensities and lifetimes, sometimes they occur within a few hours, and to date the physical characteristics of the magnetic regions that produce CMEs are still poorly understood. Figure 3.60 (color section) from Cremades, Bothmer and Tripathi (2006) shows the source regions of CMEs during 1996–2002 together with the evolution of the longitudinal component of the photospheric magnetic field. CMEs originating from active regions (marked red) follow the typical butterfly pattern seen for the sunspots, whereas CMEs originating from quiescent regions (marked green) typically occur at the higher latitudes. Magnetograms thus provide an important base to identify possible source regions of CMEs, however the reasons for their onsets are not yet understood and need much further investigation in the future. So far the onset of CMEs can only be guessed in advance, based on solar magnetograms or solar white-light observations showing the appearance of new active regions at the east limb and the distribution of active and quiescent regions on the visible solar disk. In contrast to observations from Earth, SoHO/MDI provides continuous observations of the photospheric magnetic field. The MDI observations in Figure 3.61 show how, occasionally, photospheric magnetic flux of strong intensity can emerge even at times near solar activity minimum within a relatively short time, as was the case in January 2005. The emerging flux consequently led to major solar eruptions and SEP events as described in Section 3.3.5. Figure 3.62 (color section) shows an example of how the small-scale emergence of magnetic flux in the source region of a prominence-associated CME observed by SoHO on September 12, 2000 may have caused its eruption (Bothmer and Tripathi, 2006). The threshold for magnetic field data was taken as ± 200 G in the analysis of the MDI data at a time resolution of 96 minutes, to allow identification of significant changes in magnetic field uniquely. From the observations shown in Figures 3.60 and 3.62 it appears obvious that emerging photospheric flux at various spatial scales is a key trigger of solar activity. Newly emerging flux may already be detected by means of helioseismology methods at the far side of the Sun invisible to direct observations from Earth, as shown in Figure 3.63. Here, a new active region with increased magnetic flux appers as a large-scale local inhomogeneity to the propagation of solar seismic waves. However, in contrast to filament eruptions and CMEs associated with emerging flux, cases have also occurred where annihilation of magnetic flux of opposite polarity was observed along a filament channel (separating regions of opposite magnetic polarity) shortly before the eruption of a filament and CME (Bothmer and Tripathi, 2006). This scenario is referred to as a flux cancellation process (e.g., Linker *et al.*, 2003). Studies

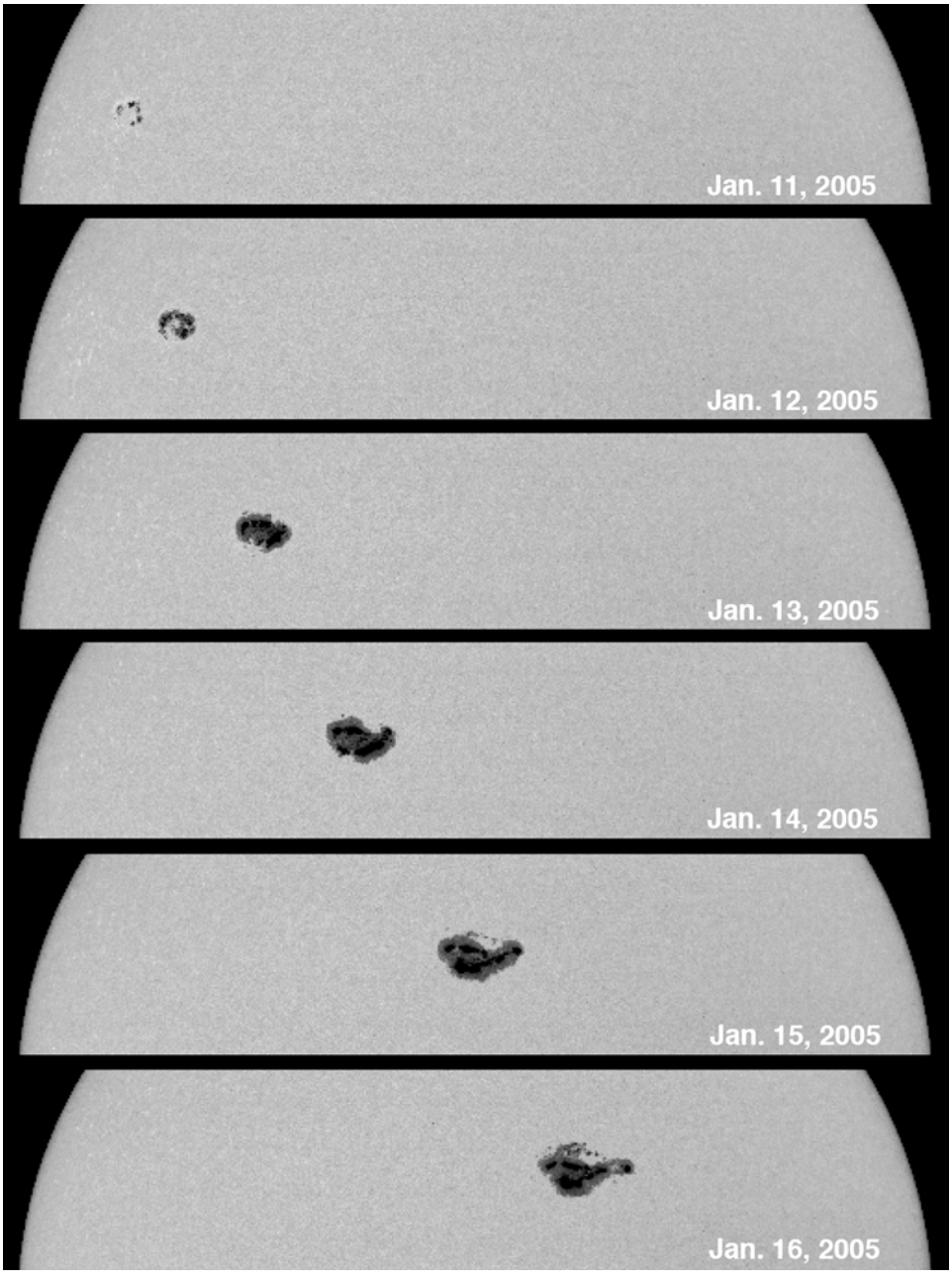

Figure 3.61. SoHO/MDI white-light observations of the development of a sunspot region between January 11 and 16, 2005 when the Sun was approaching solar activity minimum. The active region associated with the emerging magnetic flux caused several fast CMEs, one was associated with a GLE. Courtesy: SoHO/MDI Consortium.

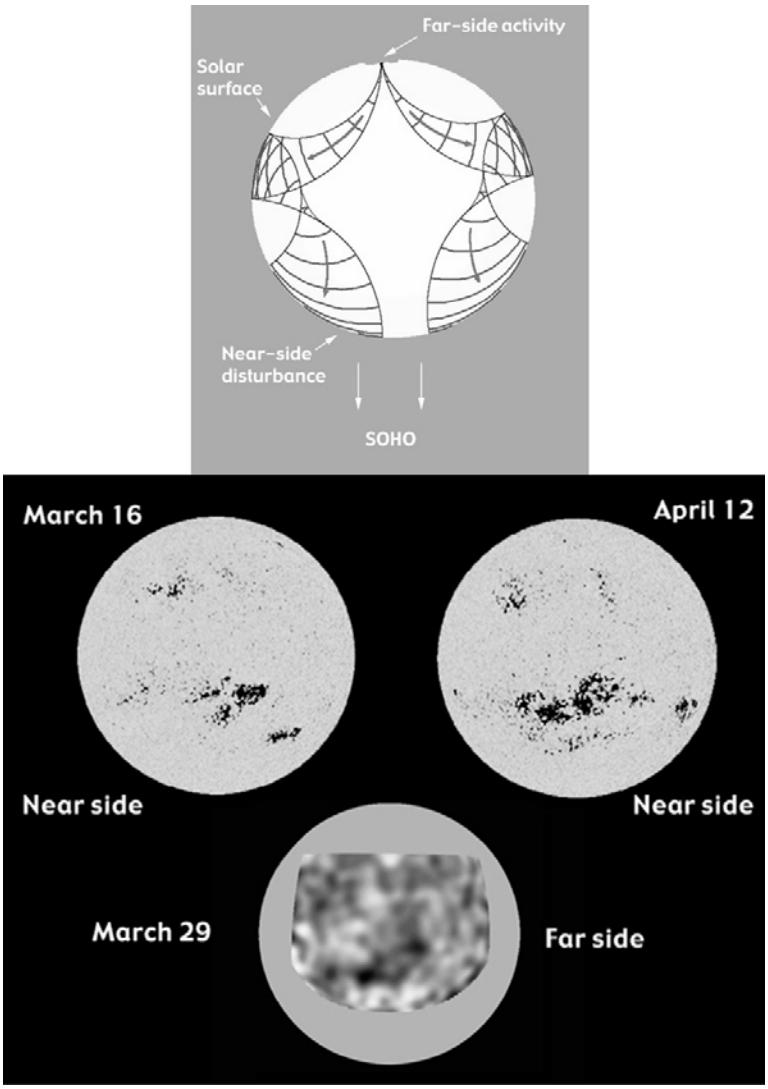

Figure 3.63. Top: an active region on the side of the Sun facing away from the Earth causes sound waves, represented by arcs, that travel through the interior, bounce once off the surface, and reach the side facing the Earth (the near side). The waves generate ripples on the near side surface and are reflected back toward the active region. An active region reveals itself because it possesses very strong magnetic fields that speed up the sound waves. Waves that pass through an active region have a round trip travel time about 12 seconds shorter than the average of 6 hours. The difference becomes evident when sound waves shuttling back and forth get out of step with one another. Bottom: three-panel image, showing absolute magnetic field strength of the same feature (upper left) one-half solar rotation before, and (upper right) one-half solar rotation after the (below, center) holographically imaged far-side region. Courtesy: NASA and ESA (*http://science.nasa.gov/headlines/y2000/ast09mar_1.htm*).

of the relationship of photospheric and coronal observations at a higher time resolution have only been facilitated recently through SoHO. It can be expected that new missions – like STEREO (Solar TErrestrial RElations Observatory) and Solar-B – operating simultaneously and providing disk and limb observations, will yield unprecedented observations of the connection of physical processes of the overlying corona with the evolution of the underlying photospheric magnetic field. Possible thresholds in terms of the magnetic flux in the photosphere that are required to cause CMEs are not known yet but likely exist, since without the presence of bipolar regions covering a substantial area in the photosphere no CMEs seem to occur.

Besides the unresolved question about what causes the onset of a CME is the question about its tentative speed and propagation time to Earth (e.g., dal Lago *et al.*, 2004; Gopalswamy *et al.*, 2001; Huttunen *et al.*, 2005; Schwenn, 2006; Zhang *et al.*, 2003). To determine the arrival times of ICMEs at 1 AU based on coronagraph observations is a difficult task because of the projection effects inherent in white-light observations (e.g., Cremades and Bothmer, 2004). Front-side disk-centered (i.e., likely Earth-directed) CMEs watched from Earth (or the L1 orbit of SoHO) unfortunately appear as unstructured halos (see Figure 3.28). In such cases a reliable radial propagation speed is hard to derive. Dal Lago *et al.* (2004) and Schwenn *et al.* (2005) have developed the model shown in Figure 3.64, which allows forecasting the arrival time of CMEs at Earth's orbit by discriminating between the expansion and propagation speeds of CMEs originating from different source locations at the Sun (limb, near-limb, halo events). A thorough analysis based on CMEs observed by SoHO/LASCO (Figure 3.64) yielded the following estimate for the travel time (T_{tr}) of halo CMEs to 1 AU (for magnetic cloud type ICMEs and shocks see Huttunen *et al.*, 2005):

$$T_{tr} = 203 - 20.77 * \ln(V_{exp}) \qquad (T_{tr} \text{ in hours, } V_{exp} \text{ in km/s})$$

It seems plausible to assume that those CMEs which propagate into slower ambient solar wind within the inner heliosphere are those which are decelerated most on their way to Earth's orbit. Systematic studies of the properties of CMEs/ICMEs in the inner heliosphere are required to further help understand better their heliospheric evolution (e.g., Forsyth and Bothmer *et al.*, 2006). The proton density, N_P, decrease inside magnetic cloud type ICMEs was studied by Bothmer and Schwenn (1998) using data from the Helios 1 and 2 spacecraft for the inner heliosphere between 0.3 and 1.0 AU, with the result that the density inside these ICMEs decreased in proportion to the distance from the Sun as $R^{-2.4}$. The radial size, s, of these magnetic cloud type ICMEs was found to increase proportionally with distance, R, from the Sun as $s(R) = 0.24 \times R^{0.78}$ (R in AU). A quantitative determination of the evolution of the magnetic field strength of ICMEs up to 1 AU and realistic simulations of compression effects due to interactions with the ambient solar wind still remain to be modeled. Figure 3.65 shows a rare case in which kilometric type II radio-wave observations from the WIND spacecraft have been used to track the CME/ICME in January 1997 from the Sun to beyond Earth.

The internal magnetic field configuration and spatial orientation of CMEs/ICMEs may be predicted according to the scenario proposed by Bothmer and Rust (1997) and Bothmer and Schwenn (1994, 1998), in which the helical magnetic flux

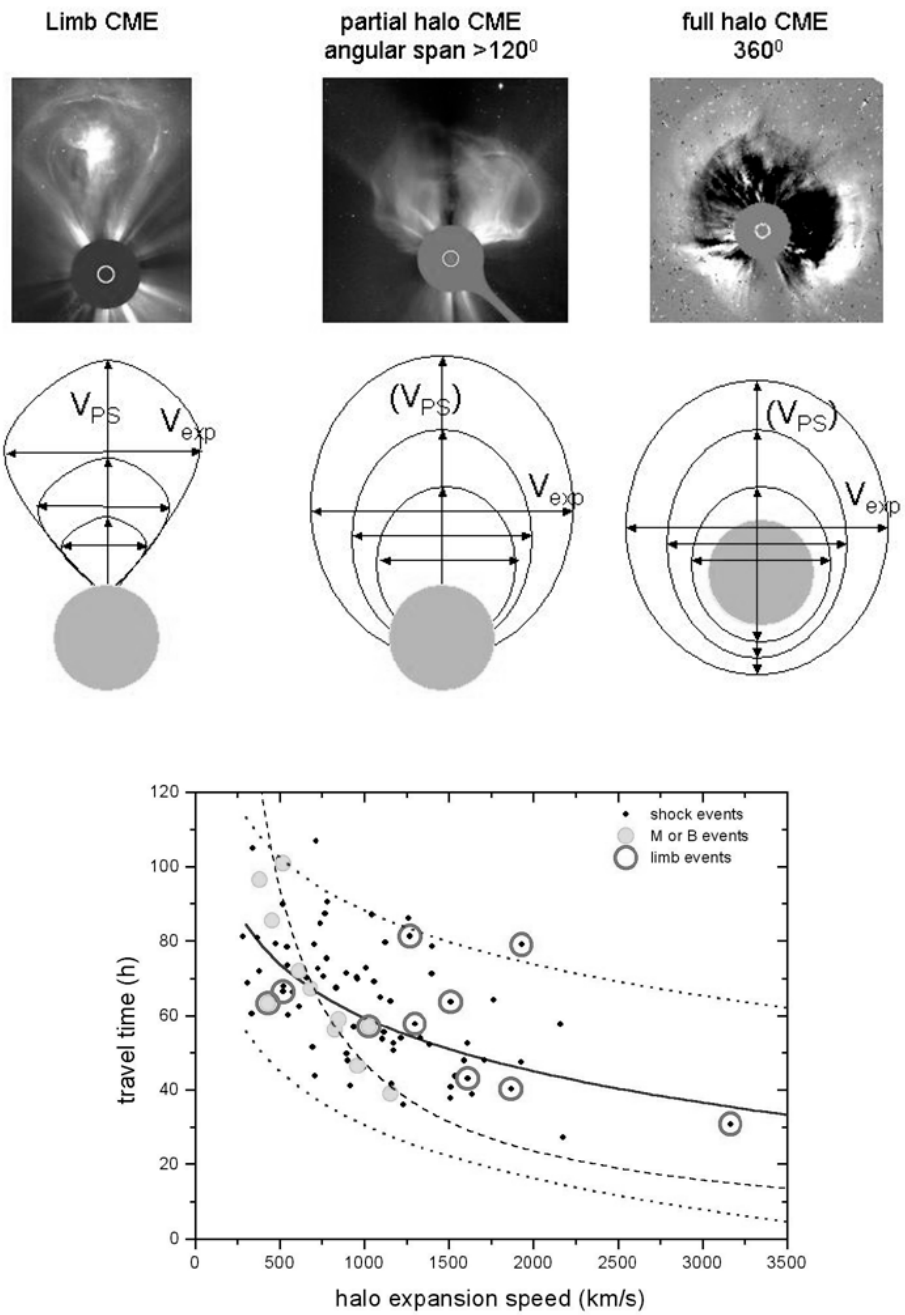

Figure 3.64. Top images: sketch showing the direction of the propagation speed (V_{PS}) and that of the expansion speed (V_{exp}) for CMEs at the limb, near the limb and for halo events. Bottom: comparison of the travel time of CMEs to 1 AU with the calculated halo expansion speeds. From Dal Lago *et al.* (2004).

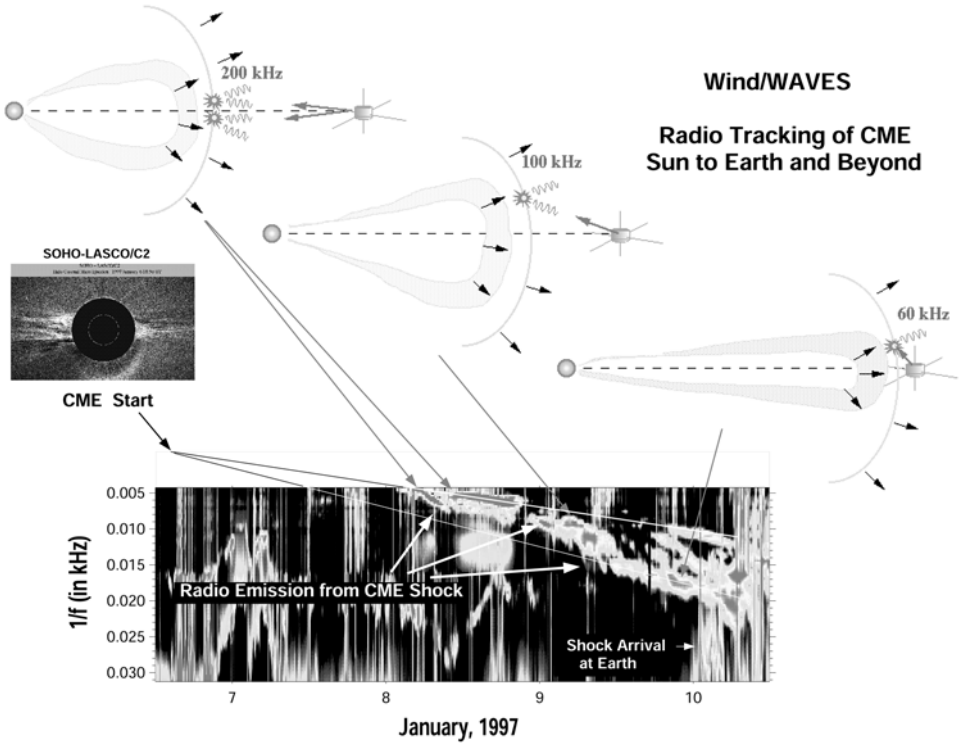

Figure 3.65. Radio tracking of a CME-driven shock from the Sun to beyond Earth by the WIND/WAVES instrument for the January 6, 1997 CME. Propagation of the shock is observed as an interplanetary type II emission. Since the radial distance of the type II emission (proportional to $1/f$) and thus the speed of the shock front depends on the density model and geometry chosen, the sketches at the top could only be constructed after the shock passage by the Earth. Courtesy: M. Kaiser, NASA/GSFC, Science Definition Team Report for the NASA STEREO Mission, 1997.

rope structure of CMEs/ICMEs can be inferred from the underlying magnetic polarity in the CME's photospheric source regions, orientation of the associated filaments and post-eruptive arcades and the handedness preference in the two different solar hemispheres (Figure 3.66). A recent study under development indicates that magnetic cloud type ICMEs with opposite orientations and magnetic configurations to those expected from Figure 3.66 result from those events which originate at the Sun from bipolar regions which do not show the Joy and Hale typical patterns expected for the given solar cycle, such as bipolar regions of opposite magnetic polarity and with orientations reversed from systematic hemispheric inclinations or from quadrupolar magnetic field regions at times when bipolar regions are located close to each other. In these cases hemispheric-handedness is opposite to that expected according to the simple scheme shown in Figure 3.66. This is an encouraging result in that it seems likely in the near future to reliably predict the internal magnetic structure and spatial orientation of ICMEs from the Sun to 1 AU. Future studies should help establish

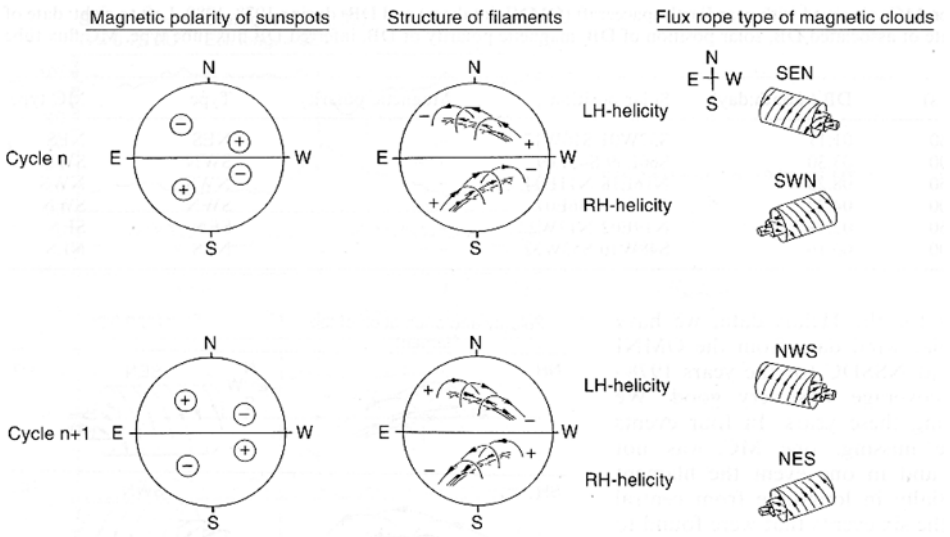

Figure 3.66. Solar cycle dependence of the magnetic field structure of filaments at the Sun and that of the corresponding MCs in the interplanetary medium. Note that for simplicity the MCs are oriented horizontally with respect to the ecliptic plane and that the cycles do not indicate any overlaps nor do they take into account the situation in magnetic regions in the photosphere that reveal a more complex field configuration (e.g., in quadrupolar regions). From Bothmer and Rust (1997), Bothmer and Schwenn (1998).

quantitative forecasts for the field strength, diameter and arrival time of ICMEs. It should be noted that the effects of the global structure of the corona should also be taken into account, since CMEs are deflected in their direction of propagation with respect to their low coronal source regions in the presence of polar coronal holes, as shown in Figure 3.51 (Cremades and Bothmer, 2004). What has been learned in the past years from SoHO and Yohkoh observations is that there exist reliable signatures in the solar corona, such as coronal dimmings, EIT waves, post-eruptive arcades, filament eruptions, observable especially at EUV and X-ray wavelengths, from which the onset of a CME can be deduced relatively certainly (Tripathi, Bothmer and Cremades, 2004; Zhukov, 2005; Zhukov and Auchère, 2004), whereas flares can occur without CMEs and sigmoids are signatures of CMEs if a sigmoid to arcade restructuring occurs.

Future research is certainly needed to better understand the onset of CMEs, their 3-D structure and interplanetary evolution as ICMEs. A new mission dedicated to help unravel these questions and help clarify the space weather effects of CMEs/ICMEs is currently under preparation for launch in 2006: NASA's STEREO consists of two suitable, nearly identical spacecraft, equipped with optical telescopes (coronagraphs, EUV imagers and interplanetary cameras) that will allow for the first time study of the 3-D structure of CMEs and their evolution from the Sun to Earth's orbit and beyond, simultaneously from new vantage points from the Sun–Earth line (*http://stp.gsfc.nasa.gov/missions/stereo/stereo.htm*).

Figure 3.67 shows schematically the orbit of the two STEREO spacecraft and the set of near-Sun imagers called SCIP (Sun-Centered Imaging Package), including the entrance aperture mechanism SESAMe (SECCHI Experiment Sun Aperture Mechanism (Howard *et al*., 2000), the command sent for opening the telescope doors is 'open sesame'). The twin spacecraft will drift by 22° per year in opposite directions in near 1-AU orbits with respect to the Sun–Earth line. Scientists hope that STEREO will approximately operate until 5 years from launch – that is, until 2011 which is the next solar maximum. STEREO will allow for the first time real-time space weather predictions with forecast times from ~1 to 5 days, depending on the speed of the earthward-propagating CMEs/ICMEs. The two STEREO satellites will also sample the *in situ* plasma and magnetic field characteristics of ICMEs and the flows of solar energetic particles (e.g., Luhmann *et al*., 2005). The physical mechanisms of particle acceleration are at the moment poorly understood, but they are of high importance in order to forecast radiation hazards to astronauts on the ISS and for manned missions to Mars and the Moon (see Chapters 5 and 11) – it is worth pointing out here that Moon and Mars have no shielding atmosphere like the Earth – and also to airline crews and passengers. Though the travel time of high-energy particles to Earth's orbit is only several tens of minutes, and short-time exposure might not be predictable, long-time (several hours to days) exposure for humans can be avoided through real-time CME/flare alerts based on routine observations of the evolution of the photospheric magnetic field and imaging of the corona. Finally, Table 3.9 provides a brief payload concept for a future space mission operating in low Earth orbit (LEO) that could provide the most important observations needed to help establish reliable space weather forecasts.

3.6 ACKNOWLEDGEMENTS

V. B. acknowledges the support of the project Stereo/Corona by the German Bundesministerium für Bildung und Forschung through the Deutsche Zentrum für Luft- und Raumfahrt e.V. (DLR, German Space Agency). Stereo/Corona is a science and hardware contribution to the optical imaging package SECCHI, developed for the NASA STEREO mission to be launched in 2006. Further information can be found at *http://stp.gsfc.nasa.gov/missions/stereo/stereo.htm*. A. Z. acknowledges support from the Belgian Federal Science Policy Office through the ESA-PRODEX programme. Both authors acknowledge the support of the EU–ESA/INTAS projects 99-727 and 03-51-6206. We thank all the members of the SoHO/LASCO/EIT/MDI consortium who built the instruments and provided the data used in this chapter. LASCO, EIT and MDI images are courtesy of the SoHO consortium. SoHO is a project of international cooperation between ESA and NASA. The *CME Catalog* is generated and maintained by NASA and the Catholic University of America in cooperation with the Naval Research Laboratory. We acknowledge the use of H_α data from the Observatory of Meudon. The NSO/Kitt Peak data shown are produced cooperatively by NSF/NO AO, NASA/GSFC and NOAA/SEL. We also would like to thank the Yohkoh, TRACE, WIND and ACE consortia in the same way as the SoHO consortium.

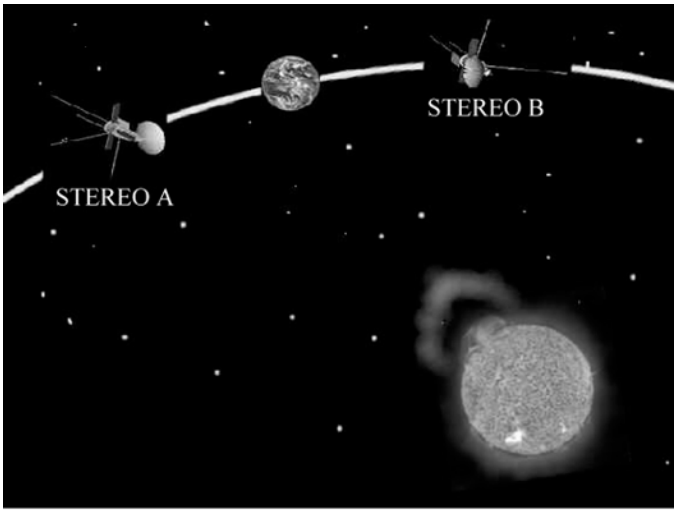

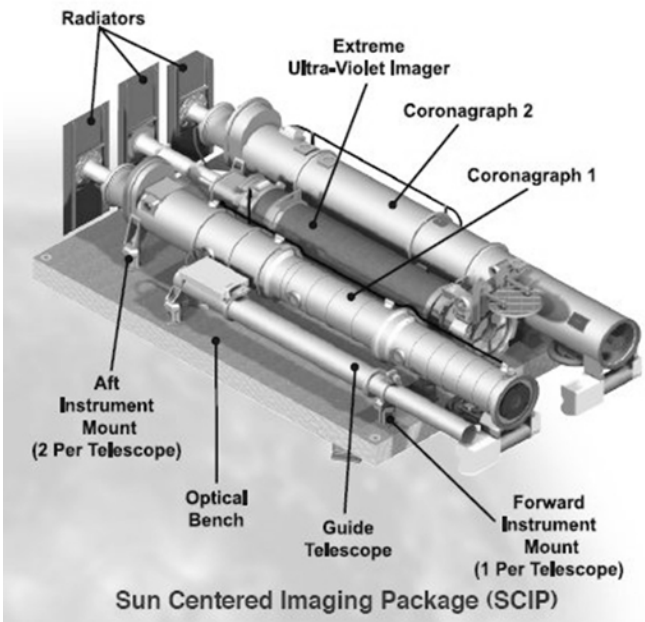

Figure 3.67. Top: schematic of the orbit of the STEREO spacecraft A (ahead) and B (behind). Courtesy: NASA STEREO Consortium. Bottom: the SCIP (Sun-Centered Imaging Package) of the SECCHI (Sun–Earth Connection Coronal and Heliospheric Investigation) imaging package for the NASA STEREO Mission. SESAMe are the SECCHI experiment Sun apperture mechanisms (reclosable doors). Courtesy: SECCHI Consortium.

Table 3.9. Prime payload for solar observations enabling reliable space weather forecasts.

Instrument	Wavelength for observations, field of view and time cadence	Space weather target
EUV imager	195 Å, 171 Å full disk, $\lesssim$5 min.	Detection of coronal transients, active regions, CME onsets and post-eruptive signatures, heliographic location of CME source region
Coronagraph	White-light, 1.5–10 R_S, $\lesssim$10 min.	Detection of halo and partial halo CMEs and provision of speed estimates
Magnetograph (if not supplied through ground-based observations)	Ni I 6768, full disk scans, <3 hours	Detection of newly emerging flux, active regions, sunspots, flux evolution, magnetic structure of CME source regions

Thanks go further to Dr. Hebe Cremades, Dr. Durgesh Kumar Tripathi and Ralf Kotulla who helped solve technical issues and/or provided results from their work. I would finally like to thank Daniel Berdychevsky and Ronald Lepping for providing the solar wind data plot for the Bastille event.

3.7 REFERENCES

Alfvén, H., Electric currents in cosmic plasmas, *Rev. Geophys. Space Phys.*, **15**, 271, 1977.

Allen, J.H. and D.C. Wilkinson, Solar–terrestrial activity affecting systems in space and on Earth, *Solar–Terrestrial Predictions – IV: Proceedings of a Workshop at Ottawa, Canada May 18–22, 1992*, J. Hruska, M.A. Shea, D.F. Smart, and G. Heckman (eds.), p. 75, 1992.

Allen, J.H., H. Sauer, L. Frank and P. Reiff, Effects of the March 1989 solar activity, *EOS*, **70-46**, 1486–1488, 1989.

ANSER, *Foundations of Solar Particle Event Risk Management Strategies*, prepared under NASA Grant NAGW-4166 for the NASA Mission from Planet Earth Study Office and Life and Microgravity Science and Applications Office, ANSER Suite 800, 1215 Jefferson Davis Highway, Arlington, VA 22202, 1996.

Aschwanden, M., *Physics of the Solar Corona: An Introduction*, Springer-Praxis, 2004.

Aschwanden, M., S.K. Antiochos, J.W. Cook, R.A. Howard, J.T. Karpen, J.A. Klimchuk, N.R. Sheeley, L.A. Fisk, T.I. Gombosi, N. Lugaz *et al.*, Theoretical modeling for the STEREO Mission, *Space Sci. Rev.*, in press, 2006.

Badalyan, O.G., V. Obridko and N.J. Sykora, *Solar Physics*, **199**, 421, 2001.

Baker, D.N., Specifying and forecasting space weather threats to human technology, in *Effects of Space Weather on Technology Infrastructure*, I.A. Daglis (ed.), Kluwer Academic, pp. 1–25, 2004.

Balogh, A., V. Bothmer (Co-Chairs), N. Cooker, R.J. Forsyth, G. Gloeckler, A. Hewish, M. Hilchenbach, R. Kallenbach, B. Klecker, J.A. Linker *et al.*, The solar origin of corotating interaction regions and their formation in the inner heliosphere (Report of Working Group 1), *Space Sci. Rev.*, **89**, 141–178, 1999.

Balogh, A., R.G. Marsden and E.J. Smith, *The Heliosphere near Solar Minimum: The Ulysses Perspective*, Springer-Praxis, 2001.

Bartels, J., Terrestrial–magnetic activity and its relations to solar phenomena, *Terr. Magn. Atmosph. Electr.*, **37**, 1–52, 1932.

Bartels, J., Discussion of time-variations of geomagnetic activity indices Kp and Ap, 1932–1961, *Ann. Geophys.*, **19**, 1–20, 1963.

Bartels, J. and J. Veldkamp, Geomagnetic and solar data: International data on magnetic disturbances, *J. Geophys. Res.*, **54**, 295–299, 1949.

Bastian, T.S., M. Pick, A. Kerdraon, D. Maia and A. Vourlidas, The coronal mass ejection of 1998 April 20: Direct imaging at radio wavelengths, *Astrophys. J.*, **558**, L65–L69, 2001.

Benevolenskaya, E.E., A.G. Kosovichev, J.R. Lemen, P.H. Scherrer and G.L. Slater, Large-scale solar coronal structure in soft X-rays and their relationship to the magnetic flux, *Astrophys. J.*, **571**, L181–L185, 2002.

Biermann, L., Kometschweife und solare Korpuskularstrahlung, *Z. Astrophys.*, **29**, 274, 1951.

Bohlin, J.D. and N.R. Sheeley Jr., Extreme ultraviolet observations of coronal holes: II. Association of holes with solar magnetic fields and a model for their formation during the solar cycle, *Solar Physics*, **56**, 125–151, 1978.

Borello Filisetti, O., G. Lovera, V. Mussino, M. Parisi and M. Storini, On the geomagnetic response to high-speed solar wind streams, *Ann. Geophys.*, **6**, 627–634, 1988.

Bothmer, V., Solar corona, solar wind structure and solar particle events, *Proc. of ESA Workshop on Space Weather, November 1998*, ESA WPP-155, ISSN 1022-6656, pp. 117–126, 1999.

Bothmer, V., Sources of magnetic helicity over the solar cycle, *Proc. ISCS 2003 Symposium, 'Solar Variability as an Input to the Earth's Environment'*, ESA SP-535, p. 419, 2003.

Bothmer, V., The solar and interplanetary causes of space storms in solar cycle 23, *IEEE Transactions on Plasma Science*, **32**, 4, 2004.

Bothmer, V., The solar atmosphere and space weather, in *Solar System Update*, P. Blondel and J.W. Mason (eds.), Springer-Praxis, pp. 1–53, 2006.

Bothmer, V. and Rust, D.M., *The Field Configuration of Magnetic Clouds and the Solar Cycle*, AGU Geophys. Monogr. 99, pp. 139–146, 1997.

Bothmer, V. and Schwenn, R., Eruptive prominences as sources of magnetic clouds in the solar wind, *Space Sci. Rev.*, **70**, 215–220, 1994.

Bothmer, V. and R. Schwenn, The interplanetary and solar causes of major geomagnetic storms. *J. Geomagn. Geoelectr.*, **47**, 1127–1132, 1995.

Bothmer, V. and Schwenn, R., Signatures of fast CMEs in interplanetary space, *Adv. Space Res.*, **17**, 319–322, 1996.

Bothmer, V., and Schwenn, R., The structure and origin of magnetic clouds in the solar wind, *Annales Geophysicae*, 1–24, 1998.

Bothmer, V. and D. Tripathi, Photospheric field evolution in the source regions of coronal mass ejections, *SOHO 17 Conference Proceedings*, in press, 2006.

Bothmer, V., M.I. Desai, R.G. Marsden, T.R. Sanderson, K.J. Trattner, K.-P. Wenzel, J.T. Gosling, A. Balogh, R.J. Forsyth, B.E. Goldstein, Ulysses observations of open and closed magnetic field lines within a coronal mass ejection, *Astron. Astrophys.*, *316*, 493–498, 1996.

Bothmer, V., B. Heber, H. Kunow, R. Müller-Mellin, G. Wibberenz, J.T. Gosling, A. Balogh, A. Raviart and C. Paizis, The effects of coronal mass ejections on galactic cosmic rays in the

high latitude heliosphere: Observations from Ulysses' first orbit, *Proc. 25th Int. Cosmic Ray Conference*, Space Research Unit, **1**, 333–336, 1997a.

Bothmer, V., A. Posner, H. Kunow, R. Müller-Mellin, B. Heber, M. Pick, B.J. Thompson, J.-P. Delaboudinière, G.E. Brueckner, R.A. Howard *et al.*, Solar energetic particle events and coronal mass ejections: New insights from SOHO, *Proc. 31st ESLAB Symposium*, ESA SP-415, p. 207, 1997b.

Brekke, P., B. Fleck, S.V. Haugan, T. van Overbeek, H. Schweitzer and M. Chaloupy, Space weather effects on SOHO and its role as a space weather watchdog, *Proc. 8th Spacecraft Charging Technology Conf., October 20–24, 2003, Huntsville, AL*, in press, 2006.

Brueckner, G.E., R.A. Howard, M.J. Koomen, C.M. Korendyke, D.J. Michels, J.D. Moses, D.G. Socker, K.P. Dere, P.L. Lamy, A. Llebaria *et al.*, The Large Angle Spectroscopic Coronagraph (LASCO), *Solar Phys.*, **162**, 357–402, 1995.

Brueckner, G.E., J.-P. Delaboudiniere, R.A. Howard, S.E. Paswaters, O.C. St. Cyr, R. Schwenn, P. Lamy, G.M. Simnett, B. Thompson, D. Wang, Geomagnetic storms caused by coronal mass ejections (CMEs): March 1996 through June 1997, *Geophys. Res. Lett.*, **25**, 3019, 1998.

Burlaga, L.F., Interaction with the earth, *Space Sci. Rev.*, **17**, 327, 1975.

Burlaga, L.F. and J.H. King, Intense interplanetary magnetic fields observed by geocentric spacecraft during 1963–1975, *J. Geophys. Res.*, **84**, 6633, 1979.

Burlaga, L.F. and R.P. Lepping, The causes of recurrent geomagnetic storms, *Planet. Space Sci.*, **25**, 1151–1160, 1977.

Burlaga, L., Sittler, E., Mariani, F. and Schwenn, R., Magnetic loop behind an interplanetary shock: Voyager, Helios and IMP 8 observations, *J. Geophys. Res.*, **86**, 6673–6684, 1981.

Burlaga, L.F., L. Klein, N.R. Sheeley Jr., D.J. Michels, R.A. Howard, M.J. Koomen, R. Schwenn and H. Rosenbauer, A magnetic cloud and a coronal mass ejection, *J. Geophys. Res.*, **9**, 1317–1320, 1982.

Burlaga, L.F., K.W. Behannon and L.W. Klein, Compound streams, magnetic clouds, and major geomagnetic storms, *J. Geophys. Res.*, **92**, 5725–5734, 1987.

Burlaga, L., R. Fitzenreiter, R. Lepping, K. Ogilvie, A. Szabo, A. Lazarus, J. Steinberg, G. Gloeckler, R. Howard, D. Michels *et al.*, A magnetic cloud containing prominence material: January 1997, *J. Geophys. Res.*, **103**, 277–285, 1998.

Burton, R.K., R.L. McPherron and C.T. Russell, An empirical relationship between interplanetary conditions and Dst, *J. Geophys. Res.*, **80**, 4204, 1975.

Cane, H.V. and I.G. Richardson, Interplanetary coronal mass ejections in the near-Earth solar wind during 1996–2002, *J. Geophys. Res.*, **108**, 1156, doi:10.1029/2002JA009817, 2003.

Cane, H.V., N.R. Sheeley Jr. and R.A. Howard, Energetic interplanetary shocks, radio emission, and coronal mass ejections, *J. Geophys. Res.*, **92**, 9869–9874, 1987.

Cane, H.V., D.V. Reames and T.T. von Rosenvinge, The role of interplanetary shocks in the longitude distribution of solar energetic particles, *J. Geophys. Res.*, **93**, 9555–9567, 1988.

Canfield, R.C., H.S. Hudson and D.E. McKenzie, Sigmoidal morphology and eruptive solar activity, *Geophys. Res. Lett.*, **26**(6), 627, 1999.

Carrington R.C., Description of a singular appearance in the Sun on September 1, 1859, *Monthly Not. Royal Astron. Soc.*, **20**, 13, 1860.

Chao, J.K. and R.P. Lepping, A correlative study of ssc's, interplanetary shocks, and solar activity, *J. Geophys. Res.*, **79**(13), 1799, 1974.

Chen, J., R.A. Santoro, J. Krall, R.A. Howard, R. Duffin, J.D. Moses, G.E. Brueckner, J.A. Darnell and J.T. Burkepile, Magnetic geometry and dynamics of the fast coronal mass ejection of 1997 September 9, *Astrophys. J.*, **533**, 481, 2000.

Cortie, A.L., Sunspots and terrestrial magnetic phenomena, 1898–1911, *Monthly Not. Roy. Astron. Soc.*, **73**, 52–60, 1913.

Cortie, A.L., Sunspots and terrestrial magnetic phenomena, 1898–1911, *Monthly Not. Roy. Astron. Soc.*, **76**, 15–18, 1916.

Cremades, H. and Bothmer, V., On the three-dimensional configuration of coronal mass ejections, *Astron. and Astrophys.*, **422**, 307, 2004.

Cremades, H., V. Bothmer and D. Tripathi, Properties of structured coronal mass ejections in solar cycle 23, *Adv. Space Res.*, in press, 2006.

Crooker, N.U. and G.L. Siscoe, The effects of the solar wind on the terrestrial environment, in *Physics of the Sun*, Vol. III, D. Reidel, p. 193, 1986.

Crooker, N.U., E.W. Cliver and B.T. Tsurutani, The semiannual variation of great geomagnetic storms and the postshock Russell–McPherron effect preceding coronal mass ejecta, *Geophys. Res. Lett.*, **19**, 429–432, 1992.

Crooker, N.U. and J.T. Gosling (Co-Chairs), V. Bothmer, R.J. Forsyth, P.R. Gazis, A. Hewish, T.S. Horbury, D.S. Intriligator, J.R. Jokipii, J. Kóta *et al.*, CIR morphology, turbulence, discontinuities, and energetic particles (Report of Working Group 2), *Space Sci. Rev.*, **89**, 179, 1999.

Daglis, I.A. (ed.), *Effects of Space Weather on Technology Infrastructure*, NATO Science Series, II. Mathematics, Physics and Chemistry, p. 176, 2004.

Dal Lago, A., L.E.A. Vieira, E. Echer, W.D. Gonzalez, A.L.C. de Gonzalez, F.L. Guarnieri, N.J. Schuchand R. Schwenn, Comparison between halo cme expansion speeds observed on the Sun, the related shock transit speeds to Earth and corresponding ejecta speeds at 1 AU, *Solar Physics*, **222**(2), 323, 2004.

Delaboudinière, J.-P., G.E. Artzner, J. Brunaud, A.H. Gabriel, J.F. Hochedez, F. Millier, X.Y. Song, B. Au, K.P. Dere, R.A. Howard *et al.*, EIT: Extreme-Ultraviolet Imaging Telescope for the SOHO Mission, *Solar Physics*, **162**, 291–312, 1995.

Dere, K., J. Wang and Y. Yan (eds.), Coronal and stellar mass ejections, *Proc. IAU Symposium 226, Beijing*, 2004.

Dikpati, M., G. de Toma and P.A. Gilman, Predicting the strength of solar cycle 24 using a flux-transport dynamo-based tool, *Geophys. Res. Lett.*, **33**, L05102, doi:10.1029/2005GL025221, 2006.

Eddy, J.A., Historical evidence for the existence of the solar cycle, in *TheSolar Output and Its Variation*, O.R. White (ed.), Associated University Press, Boulder, CO, 1977.

Feynman, J. and S.F. Martin, The initiation of coronal mass ejections by newly emerging magnetic flux, *J. Geophys. Res.*, **100**, 3355, 1995.

Fleck, B. and Svetska, Z. (eds.), The first results from SOHO, *Solar Physics*, **170**, 1; **172**, 2, Kluwer Academic, 1997.

Fleck, B., Domino, V. and Poland, A., The SOHO mission, *Solar Physics*, **162**, 1, Kluwer Academic, 1995.

Forbes, T.G., A review on the genesis of coronal mass ejections, *J. Geophys. Res.*, **105**, 23153, 2000.

Forsyth, R.J. and V. Bothmer (Co-Chairs), C. Cid, N.U. Crooker, T.S. Horbury, K. Kecskemety, B. Klecker, J.A. Linker, D. Odstrcil, M.J. Reiner *et al.*, ICMEs in the inner heliosphere: Origin, evolution and propagation effects, *Space Sci. Rev.*, in press, 2006.

Froehlich, C., Solar irradiance variability, in *Solar Variability and Its Effects on the Earth's Atmosphere and Climate System*, AGU Monograph Series, J.M. Pap and P. Fox (eds.), AGU, Washington, D.C., 2003.

Gibson, S.E. and B.C. Low, Three-dimensional and twisted: An MHD interpretation of on-disk observational characteristics of coronal mass ejections, *J. Geophys. Res.*, **105**, A8, 18187, 2000.

Goldstein, H., On the Field configuration in magnetic clouds, in *Solar Wind Five*, NASA Conf. Publ. CP-2280, pp. 731–733, 1983.

Gonzalez, W.D., A unified view of solar wind–magnetosphere coupling functions, *Planetary and Space Science*, **38**(5), 627, 1990.

Gonzalez, W.D. and A.L.C. Gonzalez, Dual-peak solar cycle distribution of intense geomagnetic storms, *Planet. Space Sci.*, **38**, 181, 1990.

Gonzalez, W.D. and B.T. Tsurutani, Criteria of interplanetary parameters causing intense magnetic storms (Dst < -100 nT), *Planet. Space Sci.*, **35**, 1101, 1987.

Gonzalez, de A.L.C., W.D. Gonzalez, S.L.G. Dutra and B.T. Tsurutani, Periodic variation in geomagnetic activity: A study based on the Ap index, *J. Geophys. Res.*, **98**, 9215–9231, 1993.

Goodrich, C.C., J.G. Lyon, M. Wiltberger, R.E. Lopez and K. Papadopoulos, An overview of the impact of the January 10–11, 1997 magnetic cloud on the magnetosphere via global MHD simulation, *Geophys. Res. Lett.*, **25**(14), 2537, 1998.

Gopalswamy, N., A. Lara, S. Yashiro, M. L. Kaiser and R. A. Howard, Predicting the 1-AU arrival times of coronal mass ejections, *J. Geophys. Res.*, **106**, 29207, 2001.

Gopalswamy, N., Lara, A., Yashiro, S., Nunes, S. and Howard, R.A., Coronal mass ejection activity during solar cycle 23, in *Solar Variability as an Input to the Earth's Environment*, ESA SP-535, pp. 403–414, 2003.

Gopalswamy, N., H. Xie, S. Yashiro and I.Usoskin, I. Coronal mass ejections and ground level enhancements, *Proc. 29th International Cosmic Ray Conference*, Vol. 1, pp. 169–173, 2005.

Gosling, J.T., Coronal mass ejections and magnetic flux ropes in interplanetary space, in *Physics of Magnetic Flux Ropes*, E.R. Priest, L.C. Lee and C.T. Russell (eds.), AGU Geophys. Monogr. 58, p. 343, 1990.

Gosling, J.T., The solar flare myth, *J. Geophys. Res.*, **98**, A11, 18937, 1993a.

Gosling, J.T., Coronal mass ejections: The link between solar and geomagnetic activity, *Phys. Fluids*, **B5**, 2638, 1993b.

Gosling, J.T. and D.J. McComas, Field line draping about fast coronal mass ejecta: A source of strong out-of-the-ecliptic interplanetary magnetic fields, *Geophys. Res. Lett.*, **14**, 355–358, 1987.

Gosling, J.T. and V. Pizzo, Formation and evolution of corotating interaction regions and their three-dimensional structure, *Space Sci. Rev.*, **89**(1–2), 21, 1999.

Gosling, J.T., J.R. Asbridge, S.J. Bame, A.J. Hundhausen and I.B. Strong, Satellite observations of interplanetary shock waves, *J. Geophys. Res.*, **73**, 43, 1968.

Gosling, J.T., S.J. Bame, D.J. McComas and J.L. Phillips, Coronal mass ejections and large geomagnetic storms, *Geophys. Res. Lett.*, **17**, 901–904, 1990.

Gosling, J.T., J. Birn and M. Hesse, Three-dimensional reconnection and the magnetic topology of coronal mass ejection events, *Geophys. Res. Lett.*, **22**, 869–872, 1995.

Gringauz, K.I., V.V. Bezrukikh and V.D. Ozerov, Results of measurements of the concentration of positive ions in the atmosphere, using ion traps mounted on the Third Soviet Earth Satellite, in *Artificial Earth Satellites*, L.V. Kurnosova (ed.), New York, Plenum Press, Vol. 6, p. 77, 1961.

Harrison, R.A., Solar coronal mass ejections and flares, *Astron. and Astrophys.*, **162**, 283, 1986.

Henke, T., J. Woch, U. Mall, S. Livi, B. Wilken, R. Schwenn, G. Gloeckler, R. von Steiger, R.J. Forsyth and A. Balogh, Differences in the $O+7/O+6$ ratio of magnetic cloud and noncloud coronal mass ejections, *Geophys. Res. Lett.*, **25**, 3465, 1998.

Henke, T., J. Woch, R. Schwenn, U. Mall, G. Gloeckler, R. von Steiger, R.J. Forsyth and A. Balogh, Ionization state and magnetic topology of coronal mass ejections, *J. Geophys. Res.*, **106**, 597, 2001.

Hildner, E., J.T. Gosling, R.M. MacQueen, R.H. Munro, A.I. Poland and C.L. Ross, Frequency of coronal transients and solar activity, *Solar Physics*, **48**, 127–135, 1976.

Hoeksema, J.T., Structure and evolution of the large scale solar and heliospheric magnetic fields, PhD thesis, Stanford University, CA, 1984.

Howard, R.A., D.J. Michels, N.R. Sheeley and M.J. Koomen, The observation of a coronal transient directed at earth, *Astrophys. J.*, **263**, L101–L104, 1982.

Howard, R.A., G.E. Brueckner, O.C. St. Cyr, D.A. Biesecker, K.P. Dere, M.J. Koomen, C.M. Korendyke, P.L. Lamy, A. Llebaria, M.V. Bout *et al.*, Observations of CMEs from SOHO/LASCO, *Coronal Mass Ejections*, AGU Geophysical Monograph 99, p. 17, 1997.

Howard, R.A., A.F. Thernisien, A. Vourlidas, C. Marque and N. Patel, Modeling of CMEs for the STEREO Mission, *Proc. Solar Wind*, **11**, in press.

Hundhausen, A.J., C.B. Sawyer, L. House, R.M.E. Illing and W.J. Wagner, Coronal mass ejections observed during the Solar Maximum Mission: Latitude distribution and rate of occurrence, *J. Geophys. Res.*, **89**, 2639, 1984.

Huttunen, E.K., H.E. Koskinen and R. Schwenn, Variability of magnetospheric storms driven by different solar wind perturbations, *J. Geophys. Res.*, **107**, 10.1029/2001JA900171, 2002.

Huttunen, E.K., J. Slavin, M. Collier, H.E.J. Koskinen, A. Szabo, E. Tanskanen, A. Balogh, E. Lucek and H. Rème, Cluster observations of sudden impulses in the magnetotail caused by interplanetary shocks and pressure increases, *Ann. Geophys.*, **23**, 1–16, 2005.

Kivelson, M.G. and C.T. Russell (eds.), *Introduction to Space Physics*, Cambridge Univ. Press, ISBN 0521457149, 1995.

Klassen, A., H. Aurass, G. Mann *et al.*, *AASS*, **141**, 357, 2000.

Klassen, A., V. Bothmer, G. Mann, M. J. Reiner, S. Krucker, A. Vourlidas and H. Kunow, Solar energetic electron events and coronal shocks, *Astron. and Astrophys.*, **385**, 1078–1088, 2002.

Klein, L.W. and Burlaga, L.F., Interplanetary magnetic clouds at 1 AU, *J. Geophys. Res.*, **87**, 613–624, 1982.

Koomen, M., R. Howard, R. Hansen and S. Hansen, The coronal transient of 16 June 1972, *Solar Physics*, **34**, 447, 1974.

Koskinen, H., E. Tanskanen, R. Pirjola, A. Pulkinnen, C. Dyer, D. Rodgers, P. Cannon, J.-C. Mandeville and D. Boscher, *Space Weather Effects Catalogue*, Finish Meteorological Institute, ISSN 0782-6079, 2000.

Lang, K., *The Sun from Space*, Astronomy and Astrophysics Library, Springer-Verlag, 2000.

Lanzerotti, L.J. and T.R. Sanderson, Energetic particles in the heliosphere, in *The Heliosphere Near Solar Minimum: The Ulysses Perspective*, A. Balogh, R.G. Marsden and E.J. Smith (eds.), Springer-Praxis, pp. 259–286, 2001.

Lanzerotti, L.J., D.J. Thomson and C.G. Maclennan, Wireless at high altitudes: Environmental effects on space-based assets, *Bell Labs Technical Journal*, **5**, Summer 1997.

Lanzerotti, L.J., C. Breglia, D.W. Maurer, G.K. Johnson and C.G. Maclennan, Studies of spacecraft charging on a geosynchronous telecommunication satellite, *Adv. Space Res.*, **22**(1), 79, 1998.

Lepping, R.P., J.A. Jones, and L.F. Burlaga, Magnetic field structure of interplanetary magnetic clouds at 1 au, *J. Geophys. Res.*, **95**, 11957–11965, 1991.

Lepping, R.P., D.B. Berdichevsky, L.F. Burlaga, A.J. Lazarus, J. Kasper, M.D. Desch, C.-C. Wu, D.V. Reames, H.J. Singer, C.W. Smith *et al.*, The Bastille Day magnetic cloud and

upstrem shocks: Near-earth interplanetary observations, *Solar Physics*, **204**, 287–305, 2001.

Lepping, R.P., D.B. Berdichevsky and C.C. Wu, Sun–Earth electrodynamics: The solar wind connection, *Recent Res. Devel. Astrophys.*, **1**, 139, 2003.

Linker, J.A., Z. Mikic, D.A. Biesecker, R.J. Forsyth, S.E. Gibson, A.J. Lazarus, A. Lecinski, P. Riley, A. Szabo and B.J. Thompson, Magnetohydrodynamic modeling of the solar corona during whole Sun month, *J. Geophys. Res.*, **104**, 9809–9830, 1999.

Linker, J.A., Z. Mikic, R. Lionello and P. Riley, Flux cancellation and coronal mass ejections, *Phys. of Plasmas*, **10**(5), 1971–1978, 2003.

Lites, B.W. and B.C. Low, Flux emergence and prominences: A new scenario for 3-dimensional field geometry based on observations with the advanced stokes polarimeter, *Solar Phys.*, **174**, 91, 1997.

Low, B.C., Coronal mass ejections, magnetic flux ropes, and solar magnetism, *J. Geophys. Res.*, **106**(A11), 25141, 2001.

Low, B.C. and M. Zhang, *Global Magnetic-Field Reversal in the Corona*, AGU Geophys. Monogr. 141, p. 51, 2004.

Luhmann, J.G., D.W. Curtis, R.P. Lin, D. Larson, P. Schroeder, A. Cummings, R.A. Mewaldt, E.C. Stone, A. Davis, T. von Rosenvinge *et al.*, IMPACT: Science goals and firsts with STEREO, *Adv. Space Res.*, **36**, 1534–1543, 2005.

Lyot, B., The study of the solar corona and prominences without eclipses, George Darwin Lecture, *Mon. Not. Roy. Astron. Soc.*, **99**, 580, 1939.

Marsden, R.G., The 3-D heliosphere at solar maximum, *Space Sci. Rev.*, **97**, 1–4, Kluwer Academic, reprint, 2001.

Marubashi, K., Structure of the interplanetary magnetic clouds and their solar origins, *Adv. Space Res.*, **6**, 335–338, 1986.

Marubashi, K., *Interplanetary Magnetic Flux Ropes and Solar Filaments*, AGU Geophys. Monogr. 99, pp. 147–156, 1997.

Marubashi, K., Interplanetary magnetic flux ropes, *J. of the Communications Research Laboratory*, **49**, 3, 2002.

Mayaud, P.N., *Derivation, Meaning, and Use of Geomagnetic Indices*, AGU Geophysical Monogr. 22, 1980.

McComas, D.J., J.T. Gosling, D. Winterhalter and E.J. Smith, Interplanetary magnetic field draping about fast coronal mass ejecta in the outer heliosphere, *J. Geophys. Res.*, **93**, 2519, 1988.

McComas, D.J., S.J. Bame, P. Barker, W.C. Feldman, J.L. Phillips, P. Riley and J.W. Griffee, Solar Wind Electron Proton Alpha Monitor (SWEPAM) for the Advanced Composition Explorer, *Space Sci. Rev.*, **86**, 563–612, 1998.

McPherron, R.L., Magnetospheric substorms, *Rev. Geophys. Space Phys.*, **17**, 657, 1979.

Mikic, Z., J.A. Linker, D.D. Schnack, R. Lionello and A. Tarditi, Magnetohydrodynamic modeling of the global solar corona, *Phys. Plasmas*, **6**, 2217–2224, 1999.

Mulligan, T., C.T. Russell and J.G. Luhmann, Solar cycle evolution of the structure of magnetic clouds in the inner heliosphere, *Geophys. Res. Lett.*, **25**, 2959, 1998.

Mulligan, T. and C.T. Russell, Multispaceraft modeling of the flux rope structure of interplanetary coronal mass ejections: Cylindrically symmetric versus nonsymmetric topologies, *J. Geophys. Res.*, **106**, 10581, 2001.

Ness, N.F., Interplanetary magnetic field dynamics, in *Space Storms and Space Weather Hazards*, I.A. Daglis (ed.), Kluwer Academic, Vol. 131, 2001.

Neugebauer, M. and C.W. Snyder, Mariner 2 observations of the solar wind, 1: Average properties, *J. Geophys. Res.*, **71**, 1966.

Nicolson, I., *Die Sonne*, Herder-Verlag, Freiburg, Germany, 1982.
O'Brien, T.P. and R.L. McPherron, An empirical pase space analysis of ring current dynamics: Solar wind control of injection and decay, *J. Geophys. Res.*, **105**, 7707–7719, 2000.
Odstrcil, D., Modeling 3D solar wind structure, *Adv. Space Res.*, **32**(4), 497, 2003.
Odstrcil, D., J.A. Linker, R. Lionello, Z. Mikic, P. Riley, V.J. Pizzo and J.G. Luhmann, Merging of coronal and heliospheric numerical two-dimensional MHD models, *J. Geophys. Res.*, **107**, doi:10.1029/2002JA009334, 2002.
Panasenco, O., I.S. Veselovsky, A.V. Dmitriev, A.N. Zhukov, O.S. Yakovchouk, I.A. Zhitnik, A.P. Ignat'ev, S.V. Kuzin, A.A. Pertsov, V.A. Slemzin *et al.*, Solar origins of intense geomagnetic storms in 2002 as seen by the CORONAS-F satellite, *Adv. Space Res.*, **36**(8), 1595–1603, 2005.
Parker, E.N., Extension of the solar corona into interplanetary space, *J. Geophys. Res.*, **64**, 1675, 1959.
Parks, G.K., *Physics of Space Plasmas: An Introduction*, ISBN 0813341299, Westview Press, 2003.
Phillips, J.L., J.T. Gosling and D.J. McComas, Coronal mass ejections and geomagnetic storms: Seasonal variations, *Proc. Solar–Terrestrial Predictions Workshop, Ottawa*, 1992.
Priester, W. and O. Cattani, On semiannual variation of geomagnetic activity and its relation to solar corpuscular radiation, *J. Atm. Sci.*, **19**, 121–126, 1962.
Prölss, G., *Physik des erdnahen Weltraums: Eine Einführung*, Springer-Verlag, Berlin, 2004.
Reames, D.V., Particle acceleration by CME-driven shock waves, Highlight Paper, *26th Int. Cosmic Ray Conf.*, 1999.
Richardson, I.G., The formation of CIRs at stream–stream interfaces and resultant geomagnetic activity, in *Recurrent Magnetic Storms: Corotating Solar Wind Streams*, B. Tsurutani, R. McPherron, W. Gonzalez, G. Lu, J.H.A. Sobral and N. Gopalswamy (eds.), AGU Geophys. Monogr. 167, in press, 2006.
Richardson, I.G., E.W. Cliver and H.V. Cane, Sources of geomagnetic storms for solar minimum and maximum conditions during 1972–2000, *Geophys. Res. Lett.*, **28**, 2569–2572, 2001.
Richardson, I.G., D.F. Webb, J. Zhang, D.B. Berdichevsky, D.A. Biesecker, J.C. Kasper, R. Kataoka, J.T. Steinberg, B.J. Thompson, C.-C. Wu *et al.*, Major geomagnetic storms (Dst ≤ -100 nT) generated by corotating interaction regions, *J. Geophys. Res.*, **111**, A07S09, doi:10.1029/2005JA011476, 2006.
Richardson, J.D., Y. Liu, C. Wang and L.F. Burlaga, ICMEs at very large distances, *Adv. Space Res.*, in press, 2006.
Rosenberg, R.L. and P.J. Coleman, Solar cycle-dependent north–south field configurations observed in solar wind interaction regions, *J. Geophys. Res.*, **85**, 3021–3032, 1980.
Rostoker, G., Geomagnetic indices, *Reviews of Geophysics and Space Physics*, **10**, 935, 1972.
Russell, C.T., Geophysical coordinate transformations, *Cosmic Electrodynamics*, **2**, 184, 1971.
Russell, C.T. and R.L. McPherron, The magnetotail and substorms, *Space Sci. Rev.*, **15**, 205, 1973a.
Russell, C.T. and R.L. McPherron, Semiannual variation of geomagnetic activity, *J. Geophys. Res.*, **78**, 92, 1973b.
Russell, C.T., T. Mulligan and B.J. Anderson, Radial variation of magnetic flux ropes: Case studies with ACE and NEAR, *Solar Wind Ten: Proc. of the 10th Int. Solar Wind Conf.*, M. Velli, R. Bruno and F. Malara (eds.), American Institute of Physics, p. 121, 2003.
Scherrer, P.H., R.S. Bogart, R.I. Bush, J.T. Hoeksema, A.G. Kosovichev, J. Schou, W. Rosenberg, L. Springer, T.D. Tarbell, A. Title *et al.*, The solar oscillations investigation: Michelson Doppler Imager. *Solar Physics*, **162**, 129–188, 1995.

Schlegel, K., Wenn die Sonne verrückt spielt, *Physik in unserer Zeit*, **31**(5), 222, 2000.

Schreiber, H., On the periodic variations of geomagnetic activity indices Ap and ap, *Ann. Geophys.*, **16**, 510, 1998.

Schrijver, C.J., Catastrophic cooling and high-speed downflow in quiescent solar coronal loops observed with TRACE, *Solar Physics*, **198**, 325, 2001.

Schrijver, C.J. and M.L. DeRosa, Photospheric and heliospheric magnetic fields, *Solar Physics*, **212**, 165, 2003.

Schwenn, R., Transport of energy and mass to the outer boundary of the Earth system, in *Solar–Terrestrial Energy Program: Major Scientific Problems, Proceedings of a SCOSTEP symposium held during the XXVII COSPAR Plenary Meeting, Helsinki, University of Technology, Espoo, Finland*, pp. 13–30, 1988.

Schwenn, R., Large-scale structure of the interplanetary medium, *Physics of the Inner Heliosphere, 1: Large-Scale Phenomena*, Springer-Verlag, p. 99, 1990.

Schwenn, R., Variability of magnetospheric storms driven by different solar wind perturbations, *J. Geophys. Res.*, **107**, 10.1029/2001JA900171, 2002.

Schwenn, R., Space weather: The solar perspective, *Living Rev. Solar Physics*, **3**, 2, *http://www.livingreviews.org/lrsp-2006-2*, 2006.

Schwenn, R. and E. Marsch (eds.), *Physics of the Inner Heliosphere, 1: Large-Scale Phenomena*, Springer-Verlag, 1990.

Schwenn, R. and E. Marsch (eds.), *Physics of the Inner Heliosphere. 2: Particles, Waves and Turbulence*, Springer-Verlag, 1991.

Schwenn, R., A. dal Lago, E. Huttunen and W.D. Gonzalez, The association of coronal mass ejections with the effects of their counterparts near the Earth, *Ann. Geophys.*, **23**, 1033–1059, 2005.

Sheeley Jr., N.R., R.A. Howard, M.J. Koomen, D.J. Michels, R. Schwenn, K.-H. Mühlhäuser and H. Rosenbauer, Coronal mass ejections and interplanetary shocks, *J. Geophys. Res.*, **90**, 163–175, 1985.

Siebert, M., Maßzahlen der erdmagnetischen Aktivität, *Handbuch Physik*, Vol. 49/3 (Geophysik 3/3), pp. 206–275, Springer-Verlag, 1971.

Smith, C.W., J. L'Heureux, N.F. Ness, M.H. Acuna, L.F. Burlaga and J., Scheifele, The ACE magnetic field experiment, *Space Sci. Rev.*, **86**, 613, 1998.

Sonett, C.P. and I.J. Abrahms, The distant geomagnetic field, 3: Disorder and shocks in the magnetopause, *J. Geophys. Res.*, **68**, 1233, 1963.

St. Cyr, O.C., J.T. Burkepile, A.J. Hundhausen and A.R. Lecinski, A comparison of ground-based and spacecraft observations of coronal mass ejections from 1980–1989, *J. Geophys. Res.*, **104**, 12493, 1999.

St. Cyr, O., R.A. Howard, N.R. Sheeley Jr., S.P. Plunkett, D.J. Michels, S.E. Paswaters, M.J. Koomen, G.M. Simnett, B.J. Thompson, J.B. Gurman *et al.*, Properties of coronal mass ejections: SOHO, LASCO observations from January 1996 to June 1998, *J. Geophys. Res.*, **105**, 18169, 2000.

Stix, M., *The Sun: An Introduction*, 2nd edition, Astronomy and Astrophysics Library, Springer-Verlag, 2004.

Subramanian, P. and K.P. Dere, Source regions of coronal mass ejections, *Astrophys. J.*, **561**, 372, 2001.

Tang, F., B.T. Tsurutani, W.D. Gonzalez, S.I. Akasofu and E.J. Smith, Solar sources of interplanetary southward Bz events responsible for major geomagnetic storms (1978–1979), *J. Geophys. Res.*, **94**, 3535, 1989.

Thompson, B.J., Moreton waves, in *Encyclopedia of Astronomy and Astrophysics*, P. Murdin (ed.), article 2575, Institute of Physics, Bristol, UK, *http://eaa.iop.org/abstract/0333750888/2575*, 2000.

Tsurutani, B.T., Solar/interplanetary plasma phenomena causing geomagnetic activity at Earth, *Proceedings of the International School of Physics 'Enrico Fermi'*, B. Coppi, A. Ferrari and E. Sindoni (eds.), IOS Press, Amsterdam, pp. 273–286, 2000.

Tsurutani, B.T., The interplanetary causes of magnetic storms, substorms and geomagnetic quiet, in *Space Storms and Space Weather Hazards*, I.A. Daglis (ed.), Kluwer Academic, p. 103, 2001.

Tsurutani, B.T. and W.D. Gonzalez, The cause of high intensity long-duration continuous AE activity (HILDCAAs): Interplanetary Alfvén wave trains, *Planet. Space Sci.*, **35**, 405, 1987.

Tsurutani, B.T. and W.D. Gonzalez, The interplanetary causes of magnetic storms: A review, in *Magnetic Storms*, B.T. Tsurutani, W.D. Gonzalez, Y. Kamide and J.K. Arballo (eds.), AGU Geophys. Monogr. 98, pp. 77–89, 1997.

Tsurutani, B.T., W.D. Gonzalez, F. Tang and Y.T. Lee, Great magnetic storms, *Geophys. Res. Lett.*, **19**, 73, 1992.

Tsurutani, B.T., W.D. Gonzalez, G.S. Lakhina and S. Alex, *The Extreme Magnetic Storm of September 1–2, 1859*.

Tsurutani, B.T., W.D. Gonzalez, X.-Y. Zhou, R.P. Lepping and V. Bothmer, Properties of slow magnetic clouds, *J. of Atm. and Sol.–Terr. Phys.*, **66**, 147–151, 2004.

Tsurutani, B.T., W.D. Gonzalez, A.L.C. Gonzalez, F.L. Guarnieri, N. Gopalswamy, M. Grande, Y. Kamide, Y. Kasahara, G. Lu, I. Mann *et al.*, Corotating solar wind streams and recurrent geomagnetic activity: A review, *J. Geophys. Res.*, **111**, A07S01, doi:10.1029/2005JA011273, 2006.

Tylka, A.J., The historic solar event of January 20, 2005: A challenge for current theories on the origin of solar energetic particles?, *SHINE 2006 Workshop, 31 July–4 August, Zermatt, Utah*, *http://creme96.nrl.navy.mil/20Jan05/*, 2006.

Uchida, Y. *et al.* (eds.), *X-ray Solar Physics from Yohkoh*. University Academy Press, Tokyo, 1994.

Veselovsky, I.S., M.I. Panasyuk, S.I. Avdyushin, G.A. Bazilevskaya, A.V. Belov, S.A. Bogachev, V.M. Bogod, A.V. Bogomolov, V. Bothmer, K.A. Boyarchuk *et al.*, Solar and heliospheric phenomena in October/November 2003: Causes and effects, *Kosmicheskie Issledovaniya*, **42**(5), 453–508, 2004; translated in *Cosmic Research*, **42**(5), 435–488, 2004.

Veselovsky, I.S., V. Bothmer, P. Cargill, A.V. Dmitriev, K.G. Ivanov, E.R. Romashets, A.N. Zhukov and O.S. Yakovchouk, Magnetic storm cessation during northward IMF, *Adv. Space Res.*, **36**, 2460, 2005.

Vourlidas, A., D. Buzasi, R.A. Howard and E. Esfandiari, Mass and energy properties of LASCO CMEs, in *Solar Variability: From Core to Outer Frontiers*, ESA SP-506, p. 9194, 2002.

Wang, C.B., J.K. Chao and C.-H. Lin, Influence of the solar wind dynamic pressure on the decay and injection of the ring current, *J. Geophys. Res.*, **108**, doi:10.1029/2003JA009851, SMP 5-1/5-10, 2003.

Wang, Y.M., *Astrophys. J.*, **543**, L89, 2000.

Wang, Y.M. and N.R. Sheeley Jr., Average properties of bipolar magnetic regions during sunspot cycle 21, *Solar Phys.*, **124**, 81, 1989.

Wang, Y.M. and N.R. Sheeley Jr., On potential-field models of the solar corona, *Astrophys. J.*, **392**, 310, 1992.

Wang, Y.M. and N.R. Sheeley Jr., Filament eruptions near emerging bipoles, *Astrophys. J.*, **510**, L157, 1999.

Wang, Y.M., A.G. Nash and N.R. Sheeley Jr., Evolution of the sun's polar fields during sunspot cycle 21: Poleward surges and long-term behavior, *Astrophys. J.*, **347**, 529, 1989.

Wang, Y.M., S.H. Hawley and N.R. Sheeley Jr., The magnetic nature of coronal holes, *Science*, **271**, 464, 1996.

Wang, Y.M., N.R. Sheeley, J.H. Walters, G.E. Brueckner, R.A. Howard, D.J. Michels, P.L. Lamy, R. Schwenn and G.M. Simnett, Origin of streamer material in the outer corona, *Astrophys. J.*, **498**, L165, 1998.

Wang, Y.M., N.R. Sheeley Jr. and M.D. Andrews, Polarity reversal of the solar magnetic field during cycle 23, *J. Geophys. Res.*, **107**, A12, 1465, doi:10.1029/2002JA009463, 2002.

Webb, D.F. and A.J. Hundhausen, Activity associated with the solar origin of coronal mass ejections, *Sol. Phys.*, **108**, 383–401, 1987.

Webb., D., E.W. Cliver, N.U. Crooker, O.C. St. Cyr and B.J. Thompson, Relationship of halo coronal mass ejections, magnetic clouds, and magnetic storms, *J. Geophys. Res.*, **105**, 7491, 2000.

Wilson, R.M. and E. Hildner, On the association of magnetic clouds with disappearing filaments, *J. Geophys. Res.*, **91**, 5867–5872 , 1986.

Yashiro, S., N. Gopalswamy, G. Michalek, O.C. St. Cyr, S.P. Plunkett, N.B. Rich and R.A. Howard, A catalog of white light coronal mass ejections observed by the SOHO spacecraft, *J. Geophys. Res.*, **7105**, 2004.

Yurchyshyn, V.B., H. Wang, P.R. Goode and Y. Deng, Orientation of the magnetic fields in interplanetary flux ropes and solar filaments, *Astrophys. J.*, **563**, 381, 2001.

Zhang, G. and L.F. Burlaga, Magnetic clouds, geomagnetic disturbances and cosmic ray decreases, *J. Geophys. Res.*, **93**, 2511, 1988.

Zhang, J., K.P. Dere, R.A. Howard, M.R. Kundu and S.M. White, On the temporal relationship between coronal mass ejections and flares, *Astrophys. J.*, **559**, 452, 2001.

Zhang, J., K.P. Dere, R.A. Howard and V. Bothmer, Identification of solar sources of major geomagnetic storms between 1996 and 2000, *Astrophys. J.*, **582**, 520, 2003.

Zhao, X.P. and D.F. Webb, Source regions and storm effectiveness of frontside full halo coronal mass ejections, *J. Geophys. Res.*, **108**, 1234, doi:10.1029/2002JA009606, 2003.

Zhukov, A.N., Solar sources of geoeffective CMEs: A SOHO/EIT view, in *Coronal and Stellar Mass Ejections, Proceedings IAU Symposium No. 226*, K.P. Dere, J. Wang and Y. Yan (eds.), Cambridge University Press, pp. 437–447, 2005.

Zhukov, A.N. and F. Auchere, On the nature of EIT waves, EUV dimmings and their link to CMEs, *Astron. and Astrophys.*, **427**, 705, 2004.

Zhukov, A.N., I.S. Veselovsky, F. Clette, J.-F. Hochedez, A.V. Dmitriev, E.P. Romashets, V. Bothmer and P. Cargill, Solar wind disturbances and their sources in the EUV solar corona, in *Solar Wind Ten: Proceedings of the Tenth International Solar Wind Conference, Pisa, Italy, 17–21 June 2002*, M. Velli, R. Bruno and F. Malara, AIP Conference Proceedings 679, Issue 1, p. 711, 2003.